Modeling Biofibre (Hemp) Processing using the Discrete Element Method (DEM)

by

Mohammad Al-Amin Sadek

A Thesis submitted to the Faculty of Graduate Studies of

The University of Manitoba

in partial fulfilment of the requirements of the degree of

DOCTOR OF PHILOSOPHY

Department of Biosystems Engineering

University of Manitoba

Winnipeg

Abstract

The main objective of the research was to understand hemp processing at different stages through numerical simulations. Processing of hemp materials involves breaking the hemp into different sizes of particles and separating those particles into fractions of different sizes. Numerical models were developed using the discrete element method (DEM) to simulate hemp processing using a hammermill and separations of different hemp particles using a 3D vibratory screen-type separator. The models were implemented using a commercial DE code, the Particle Flow Code in Three Dimension (PFC^{3D}). In the models, virtual hemp, hemp fibre and core were defined using clusters of PFC^{3D} basic spherical particles which are connected by the PFC^{3D} parallel bonds. The microproperties (e.g. particle stiffness and friction coefficient, and bond stiffness and strength) of these particles were calibrated. For calibrations, virtual tests were performed using PFC^{3D} for hemp stem, fibre, and core. Those virtual tests included direct shear tests of fibre and core particles, tensile tests of fibre, and compression tests of hemp stems. The microproperties of these particles were calibrated through comparing results from the virtual tests with results from laboratory tests or literature data. Those calibrated particle microproperties were used in the PFC^{3D} models developed for simulating the hammermill for hemp processing and the 3D vibratory separator for particle separation. These two machines were constructed using various PFC^{3D} walls and lines, and had the main features and operational conditions as the real machines. The hammermill model was able to predict the power requirement of hammermill and particle dynamic behaviours (kinetic and strain energies) within the hammermill. The separator model was capable of predicting the separation efficiency of the 3D vibratory separator for separations of different hemp

particle mixtures. The behaviour of the models reflected the real behaviour observed experimentally. The model results were reasonably good as compared with literature data and the test results. The models developed have the potential to simulate many other dynamic attributes of hemp particles with the machines. This study has laid a solid foundation for future studies of biomaterial-machine interactions using the DEM.

Acknowledgements

The author wishes to express his whole hearted sense of gratitude and indebtedness to his research advisor Dr. Ying Chen for his invaluable advice, continuous guidance and monitoring, prompt help, keen interest and constant encouragement throughout the study. Acknowledgement is also extended to the members of my advisory committee, Drs. Claude Laguë, Qingjin Peng and Wen Zhong for their valuable inputs their encouragement in this research effort allowed me to benefit from their vast experience. Also would like to thank Dr. Chris K. Mechefske for his participation as the external examiner.

The author would like to express his sincere thanks to Dr. Hubert Landry for his advice and guidance in discrete element method applications. Also special thanks to Dr. Sacha Emam, Itasca Consulting Group, Inc., for his guidance at different stages of model development.

The author would like to express his special thanks to Fangliang Chen**,** Klayton Kaleta, Leno Guzman, for their technical collaboration in conducting the experimental work. Also contribution of Dr. M. R. Khan and Meaghan Baker for providing their experimental data is highly acknowledged. The author also wishes to thank all senior and junior colleagues, friends and staff of the Department of the Biosystems Engineering at the University of Manitoba for their assistance and the encouragements throughout the journey.

The author wishes to express his deep indebtedness to his wife as well as classmate Shahnaz Parvin, for her continuous encouragement and support and also who had been beside me during the course of this journey. The author also wishes to express his deep gratitude to his parents, parents-in-low, brothers, sisters and all relatives for their encouragement, blessings and dedication that contribute a lot to achieve his goal.

The author expresses his deep sense of gratitude and appreciation to NSERC, University of Manitoba, MITACS and Composite Innovation Centre (CIC) for providing financial throughout the program.

His cordial thanks are due to everyone not mentioned but most importantly not forgotten.

Table of Contents

List of Tables

List of Figures

Chapter 1

Introductory Material, Scope and Objectives of the Thesis

1.1. INTRODUCTION

Hemp (*Cannabis sativa*) fibre is an environment friendly and renewable material with numerous industrial uses, such as for textiles, bio-composites, insulators, automobile components, and building materials. To obtain good quality fibre for these uses, effective processing equipment is required. Processing of hemp includes two main processes: decortication and cleaning. Decortication is mechanically processing hemp for fibre. Therefore, the words, decorticated and processed, are interchanged in the thesis. Through decortication, hemp is broken into pieces, resulting in different sizes of fibre and cores. Thus, decorticated hemp is a mixture of fibre and cores as well as chaff. Some small cores and chaff may be removed during the decortication process. However, the decorticated hemp material may still contain a high percentage of cores and chaff. The cleaning process further removes the core and chaff from the decorticated material to obtain cleaner fibres.

Fibre processing technology is not well established yet due to a lack of the knowledge in mechanical and dynamic behaviour of hemp stalk, fibre, and core. Current machines used in hemp industries are adopted from other applications. Those machines are expensive to run due to high energy consumption and do not produce acceptable quality of fibre.

Understanding of the mechanical and dynamic behaviour of hemp material is the prerequisite for improving existing fibre processing equipment and developing new high-performance equipment.

Processed hemp material is non-homogenous and it contains different particles: fibre, core, and chaff, in various sizes. The interaction of these particles with a machine is a complicated dynamic regime. It is difficult to quantify such a regime using experiments. The discrete element method DEM has become a promising modeling tool to simulate the behaviour of particle flow. Several computer DE codes, for example, Particle Flow Code in Three Dimension (PFC^{3D}) are available commercially. Therefore, using the DEM to simulate hemp particles and hemp processing would be a wise approach to take. The major challenges of using the DEM include defining the hemp, fibre, and core particles of irregular shapes and calibrating their microproperties in the DE model.

The thesis is structured in paper format where the main research work has been described in four individual chapters. Chapters 3, 4, 5, and 6 are the four individual manuscripts which were written in a format suitable for publication in scientific journals. At the beginning of each manuscript, a brief section indicates its relationship to the thesis in its entirety. General introduction, general literature review, and general conclusions and recommendations are presented in Chapter 1, 2, and 7 respectively. Some information included in the general literature review chapter is also included in the manuscripts for completeness of the manuscript. Chapter 3 has already been published (***M. A. Sadek,*** *Y. Chen, C. Laguë, H. Landry, Q. Peng, and W. Zhong. 2011****.*** *Characterization of the Shear*

Properties of Hemp using Discrete Element Method. Trans. Of the ASABE, 54(6): 2279-2285). Chapters 4, 5, and 6 are ready to submit to scientific journals.

1.2. OBJECTIVES OF THE THESIS

The overall objective of this study was to understand the mechanical behavior of biofibre during fibre processing by developing DEM models. Results from this research will contribute to a better understanding of hemp mechanical properties and hemp processing, leading to the development of high-performance hemp processing equipment, in terms of high fibre quality, minimum fibre losses, and low energy cost, to meet the increasing industrial demand for natural fibres. The specific objectives of the study were

1. to develop a PFC^{3D} model for calibrating the particle microproperties of processed hemp fibre and core through measuring the shear properties of these marerial using direct shear tests;
2. to develop a PFC^{3D} model for calibrating the particle bond microproperties through measuring the tensile properties of hemp fibre using tensile tests;
3. to simulate energy requirement and the dynamic behaviour of hemp material subjected to different hammermill operating conditions using PFC^{3D};
4. to simulate the dynamic behaviour of decorticated hemp material in fibre separation process through measuring the separation efficiency of a 3D vibratory separator using PFC^{3D}.

Chapter 2

Literature Review

2.1. BIOFIBRE AND ITS APPLICATIONS

Biofibre is referred as the fibre obtained from the plant, animal or mineral. Biofibre is abundantly available from renewable resources. Thus biofibres are less expensive and more environment friendly. The source of plant fibres is the plant bark (bast fibre), leaf, fruit, wood, straw, and grasses whereas the source of animal fibre is hair, cocoon, and wool. The main component is cellulose for plant fibre and proteins for animal fibre. Animal biofibres are mostly for textile uses and plant biofibres are mostly used in textiles and composite materials. The best known biofibre plants are flax, hemp, linseed, jute, cotton, coir, sisal, kenaf, yucca, abaca, and ramie.

Biofibre has many advantages over other artificial fibres. Biofibres are biodegradable and have high tensile and flexural strength per weight of material. Because of these advantages biofibres are becoming popular for different industrial uses. Biofibres have been successfully used for making biodegradable composite materials. Composites made by combining (natural/bio) fibres with biodegradable resins are referred as “green” composites (Netravali and Chabba 2003). Beside composite material biofibre has been used for making light weight material, concrete reinforcement, textile, carpets, and ropes.

2.2. HEMP

Hemp (*Cannabis sativa*) is one of the biofibre plants and is a good source of bast fibre. Hemp mostly grows in temperate climate like in Canada, Russia, and Eastern Europe. Hemp seed and leaf are also a good source of oil, food and have low concentration of delta-9- tetrahydrocannabinol (THC), the major drug component in Marijuana (Gratton 2002; de Meijer 1995). Industrial hemp plants naturally attain a THC content of 0.6%. It is generally accepted that a content of 2% is required to have a noticeable effect on the human body when the plan is ingested or the smoke from the burning plant is inhaled.

2.2.1. Hemp Morphology

Hemp varieties including USO 14 and USO 31 are commonly cultivated in Canada. Hemp plants are usually 1.5 to 2.5 m tall and the average diameter of hemp stem is 7 to 16 mm (Gratton and Chen 2003). Plant height and diameter vary depending on the variety, sunlight, soil, nutrient, water, and plant density (Bocsa and Karus 1997). Male plants are usually taller than female plants (Beckermann 2007). Figure 2.1a shows a typical male and female industrial hemp plant. The hemp stem consists of woody core also called hurd with hollow pith (Fig. 2.1b). The outer bark surrounding the woody core contains the long bast fibre (Gratton and Chen 2003). The woody core is responsible for providing stiffness to the hemp stem, and the bast fibre in the bark provides tensile and flexural strength. The proportion of bast fibre and hurds varies depending on the cultivars. The bast fibre mass proportions are usually from 16 to 35% and hurd mass proportions vary from 52 to 68% (Gratton 2002; de Meijer 1995; Furl and Hempel 2000).

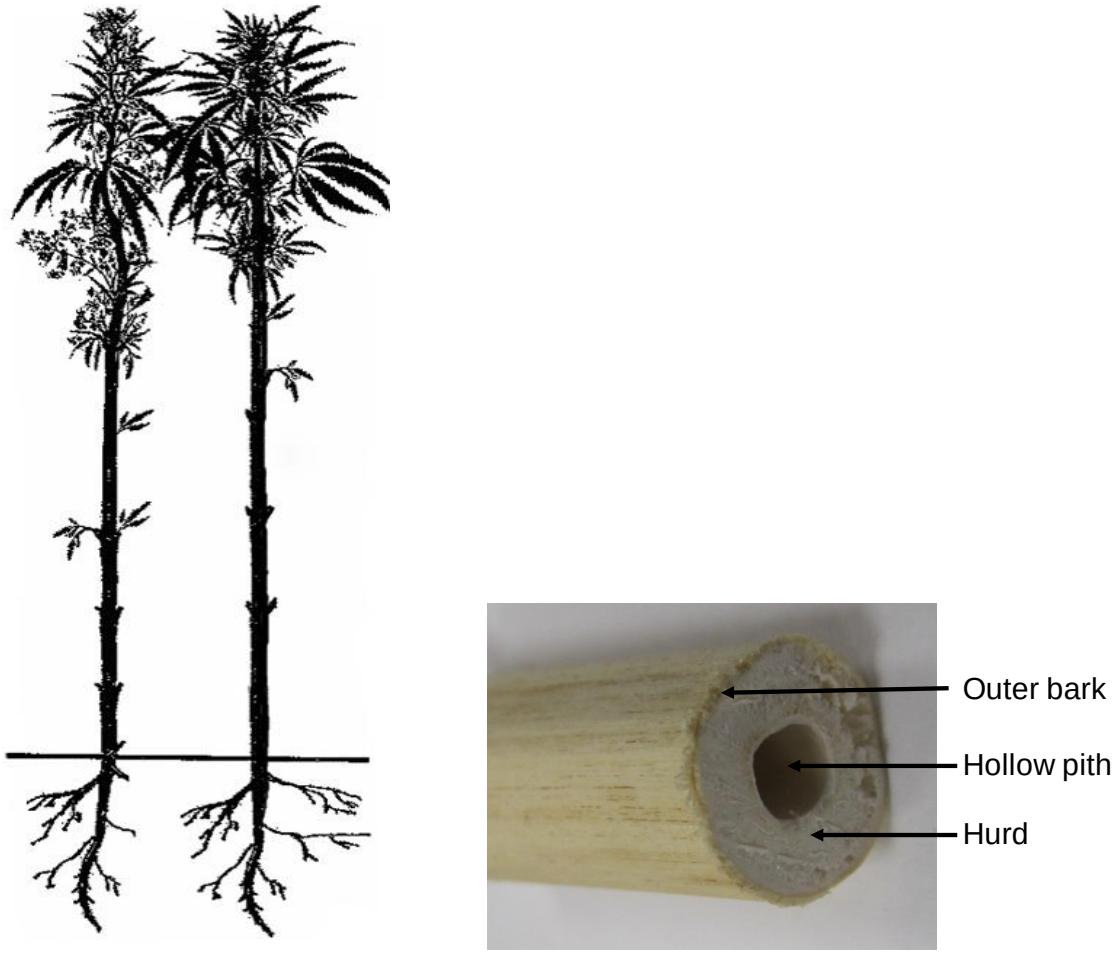

(a) (b)

Fig. 2.1. Industrial hemp plant; a) Male (left) and female (right) plant (Adopted from Beckermann (2007)), b) cross section of the plant.

Bast fibres consist of individual fibres which are bonded together by an interface, which contain mainly cellulose (67%), hemicelluloses (13%); and lignin (4%) (Bocsa and Karus 1997; Keller et al. 2001). These groups of joined single fibres are known collectively as fibre bundles, and are responsible for making up the bark tissue. The woody core consists of parenchyma cells which are composed of cellulose (37%), hemi cellulose (35%) and

Lignin (21%) (Bocsa and Karus 1997). The core are usually shorter in size and have a length of approximately 0.55 mm (Gratton 2002). Because of high its lignin and low cellulose content core is weak and easy to break.

2.2.2. Hemp Cultivation

The cultivation of industrial hemp has a long history and it is estimated that the earliest use of hemp was over 6000 years ago. In the early 19th century, because of drug content in hemp, hemp cultivation was banned in many countries with the introduction of stricter drug laws (Vignon et al. 1996). Canada banned hemp production in 1938 under Canada's federal narcotics regulations (MAFRI 2011), due to economic depression and its similarity to marijuana. In 1998, Canada repermitted cultivation of some varieties of industrial hemp, earlier permitted by European Union (EU) in 1990s. Since then Canada started growing those varieties commercially.

Hemp is a photosensitive crop, thus the harvesting of matured plant varies depending on the seeding date (Gratton 2002). As the day length starts decreasing after the summer solstice, thus maturing time of hemp is a critical issue for the cultivation. Recommended maturing time for most varieties is 120 to 150 days (MAFRI 2011). Hemp grows well on drained loam soil with a pH above 6.0; however, hemp can be grown on other various soils. Hemp is sensitive to saturated soils and prolonged exposure to wet soil condition may result in stunted growth, yellowing and plant death (MAFRI 2011). Hemps are sown in a row and conventional seeding equipment can be used to sow hemp successfully. Industrial hemp is usually sown in 150 to 180 mm row spacing and shallow seeding

depth; typically 19 to 70 mm depth (MAFRI 2011). Higher seeding depth delays the emergence and increases plant competitiveness (Gratton 2002). Recommended seeding rate for hemp fibre crop is approximately 45 kg/ha (OMAFRA 2011). Intensive fertilization is not essential for hemp production; however minimal fertilization is required for hemp in a suitable rotation. In Manitoba soil good result were obtained in soil containing total amounts of 90 to 112, 50, 67, and 17 kg/ha of N, P, K and S respectively (MAFRI 2011). Harvesting time has a big influence on the fibre quality and quantity (Bocsa and Karus 1997). Different plant sex have different optimal harvest date, such as the best harvesting time for male plants is during flowering and for the female plant is at the first appearance of flower (Bocsa and Karus 1997).

After starting growing hemp, the production area has been increasing. In the year 2006, the number of licensed area was highest in Canada. Total licensed area for hemp cultivation was 20,545 hectares in 2006 and reduced to 4,682 hectares in 2007 (MAFRI 2011). A drop of cultivation area was due to the increased inventory and positive economics of producing other crops. In 2009 total hemp cultivated area in Canada was 5,568 hectares (MAFRI 2011). Yield of hemp per hectare is also increasing gradually. Hemp yield in 2004 was 295kg/ha and has increased to 745 kg/ha in 2009 (MAFRI 2011). Currently the market for hemp is small however; potential for the hemp cultivation is high.

2.3. USE OF HEMP

2.3.1. Current Use

Hemp is extensively renewable, self tolerant crop and can be grown in the same field year after year. Also because of better physical property and biodegradability compared to other man-made products, acceptance of hemp is increasing. These properties of hemp allow for the production of a wide range of products including fibre, oils, solvents, dyes, resins, proteins, specialty chemicals, and pharmaceuticals (van Wyk 2007). Currently, Hemp has established market opportunity for the product from fibre, core and seeds. Many automotive industries, (such as several BMW models) have been using hemp fibre for molded parts (trunk liner and press-molded airbag parts) because of its light weight and recyclability (Fortenbery and Bennett 2003). Hemp fibre also has been used as an insulation material. During manufacturing and installation natural fibre has less negative environmental impact. In Europe, France and Germany are the largest producers of hemp insulation and approximately 1500 ha hemp were grown for insulation (Kymäläinen 2004). Another use of hemp fibre is wall and floor covering. Coarse fibres are usually used for making underlay materials or backing of carpet and fine fibres are used for making smooth carpets (Merfield 1999). Sometimes hemp fibre used in a mixture with wool or synthetics to produce carpets with superior characteristics such as wear, non-pilling and biodegradability (Merfield 1999). In addition hemp fibre also has use in concrete reinforcement, composite materials, rope, string and other decorative material.

As like hemp fibre, hemp core is also becoming a valuable product, even though the hemp core was a useless byproduct in the past. Core has been used for animal bedding and cat litter. Hemp core is popular because of its water absorbency, odour suppression and is less allergenic (Fortenbery and Bennett 2003; Merfield 1999). Core is also used for making particle board and ground core is used for thermoplastics. Hemp seeds are used to produce various food product such as hemp flour and hemp oil. Refined hempseed oil is primarily used in body care products and hemp seed oil is used in lubricants, paints, inks, fuel, and plastics.

2.3.2. Future Use

Hemp has very high potential for future market to replace or become as the additive source of man-made food products, cosmetics, textile and industrial materials. These products are already in the market. On the economics of hemp there is a large gap between the potential product and its financial viability (Merfield 1999). The current hemp textile market can be extended by making more fabrics and fashion accessories. Hemp has another potential market in the form of paper production. Hemp paper has better property than other tree based paper such as being more resistant to decomposition, stronger when wet, less prone to yellowing and also requires less chemical in production (Merfield 1999). In addition hemp can be used as a good source of energy as it produces a large amount of biomass.

2.4. PHYSICAL PROPERTIES OF BIOFIBRE

The qualities of fibre product depend on the fibre properties (Xu et al. 1993). Some physical properties such as fibre dimensions, defects, variability, crystallinity and structure are the most important properties that must be considered for making products from biofibre. Mechanical properties are even more important when selecting suitable fibre for composite reinforcement. The most important properties of fibre for determining the quality of end product includes the length and diameter of fibre, fibre density, fineness and the tensile strength of the fibre. Physical and mechanical properties of fibre are described below.

2.4.1. Length and Diameter

Length can be measured by following the measurement technique of the average length and length distribution in wool top under the ASTM standard D 519-04 (ASTM 2007). As diameter is not uniform in a fibre bundle, it is often derived from the fineness. Munder and Fürll (2004) used the following equation to calculate the fibre diameter.

$$d = \sqrt{\frac{4f}{\pi\rho}} \tag{2.1}$$

where

d = Diameter of fibre bundle (μm),

f = Fineness (tex), and

ρ = particle density (kg/m^3).

2.4.2. Density

Fibre density is an important property of hemp fibre. Natural fibre is highly variable in terms of linear density, even among samples coming from the same feedstock or the same plant. Fiber is usually defined by two different types of density: Particle density and linear density. Particle density of fibre is usually measured by the standard particle density measurement method. Linear density is calculated by mass per unit length of fibre.

2.4.3. Fineness

Fibre fineness is usually measured as the mass per 1000 m length of fibre. It is expressed in unit of tex where 1 tex is equal to 1 g/km (Kymälänen 2004). Gratton (2002) reported that the fibre fineness is the measure of the cross-sectional thickness of fibre obtained by counting the number of fibre in each length group and then dividing by the mean length of the weight group.

2.4.4. Tensile Strength

Biofibre has higher tensile strength compared to any other man made fibre. Tensile strength of fibre is the maximum tensile force required during the tensile test by extending the fibre to the breaking point. The unit of tensile strength is expressed in Pascal (Pa). Table 2.1 summarized different properties of hemp fibre reported by researchers.

Table 2.1. Summary of hemp fibre properties

Property	**Average**	**Range**	**Reference**
Length, mm	25	5-55	Rowell et al. (2000); Garcia-Jaldon et al. (1998); Correia et al. (1998); Kirby (1963)
		10-250	Munder and Fürll (2004)
Diameter, µm	22	15-40	Garcia-Jaldon et al. (1998); Correia et al. (1998)
		59-110	Munder and Fürll (2004)
	22	16-50	Kirby (1963)
Particle density, kg m^{-3}	1480		Bledzki et al. (1996)
Fineness, tex		3.9-13.7	Munder and Fürll (2004)
		1.66-2.08	Hobson et al. (2001)
	2.2		Gratton (2002); Doberczak et al. (1964)
		0.33-2.2	Kirby (1963)
Tensile strength, GPa	9.0		Rowell et al. (2000)
	<1.0		Beckermann (2007)
	0.69		Bledzki et al. (1996)
		0.49-0.62	Munder and Fürll (2004)

Some important physical properties of other biofibres are summarized in Table 2.2 for the comparison.

Table 2.2. Properties of other biofibres (Wambua et al. 2003; Bos et al. 2002) cited by Beckermann (2007)

Properties	**Flax**	**Jute**	**Ramie**	**Coir**	**Sisal**	**Cotton**	**Kenaf**
Density, kg m^{-3}	1400	1460	1500	1250	1330	1510	-
Tensile strength, MPa	800-1500	600-1100	500	220	600-700	400	930
Young's modulus, GPa	60-80	10-30	44	6	38	12	-
Specific Stiffness, MN m kg^{-1}	43-57	7-21	29	5	29	8	-

2.5. HEMP FIBRE PROCESSING

Hemp fibre processing is the process of obtaining fibre from the hemp plant. Processing of hemp plant includes two main processes: decortication and cleaning. In these processes, the fibre buddle is usually considered as the main product and the core is considered as the by-product. Decortication is the mechanical separation process of fibre from the raw stalk (Anthony 2002; Webber III et al. 2002; Mwaikambo 2006). Through decortication, hemp was broken into pieces, resulting in different sizes of fibre bundles and cores. Thus, the output of decortication is a mixture of fibre buddle and core as well as chaff. Some small amount of core and chaff may be removed through the decorticatations process. However, the decorticated hemp material may still contain a high percentage of cores and chaff. A cleaning process is to further remove the core and chaff from the decorticated material to obtain cleaner fibres. Figure 2 shows the typical fibre processing steps.

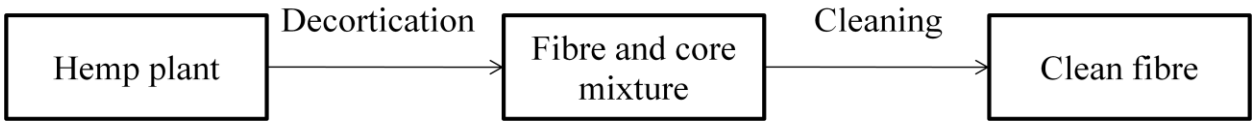

Fig. 2.2. Steps in hemp fibre processing.

Other than mechanical processing of the hemp fibre, there are few well established methods to separate fibre from the plant. These methods are known as biological methods and chemical method. A detailed description of hemp processing is given below

2.5.1. Decortication

In developed countries, mechanical separation is the most common method for fibre processing. Different machinery, including hammermills, crushing rollers, and cutterheads is used for decortications. A hammermill is a drum containing pivoted hammers mounted on a cross-shaped rotor (Feed machinery 2008). Hammermills use continuous impact and shearing force between the rotary walls of the grinding wall. Hammermills are suitable for decortications of unretted stalks where high capacity and low fibre purity are required; such as for non textile applications (Gratton and Chen 2004). Because a hammermill cannot separate the entire fibre from the core (Gratton and Chen 2004; Furll and Hempel 2000) and generate more chaff compared to other machines (Chen et al. 2004a). However, the Hammermill has high separation efficiency and does not require any retting process of the hemp stalk.

Roll crushers are also is widely used for decortication. This technique is energy efficient and used to produce long fibres. A roll crusher consists of two or more rollers with a certain gap between them. Two rollers are placed parallel to one another and rotate in opposite directions (Gupta and Yan 2006). Plants are fed lengthwise into the machine between the rollers. Broken cores fall through the roller gaps and long fibres are collected from the other end. Rollers may be flat, fluted or pinned to allow for the stem to be compressed, crimped or combed of any remaining core respectively. When the rollers has equal diameter and rotate at the same speed then the compression is the primary force; when rollers operate at different speeds shearing and compression are the primary forces.

Gratton and Chen (2004) developed a modified cutterhead machine for in field hemp decortications using a conventional forage harvester. The prototype was constructed by replacing the cutterhead originally featuring 12 knives with three knives and nine scotching bars. This modification was done to increase the cutting length (Gratton and Chen 2004). Higher fibre purity can be achieved from this modified cutterhead with lower feed rate.

2.5.2. Fibre Cleaning

Fibre cleaning is a difficult process due to lack of knowledge and appropriate cleaning equipment. In addition, the challenge of fibers tending to tangle together remains unsolved. Cores are held in tangled fibre bundles during a cleaning process, resulting in poor core removal. Different methods have been tried to separate the core from decorticated hemp material. Few cleaning machines have been specifically designed for

separating hemp core from fibre. In most cases, people have adopted cleaning equipment from other applications, such as screen type machines for separating dry materials into various sizes. Gratton and Chen (2004) used straw walkers for cleaning fibres and found that the straw walker was insufficient for fibre cleaning. Münder et al. (2004) proposed a multiple ultra cleaner for separating fibre from decorticated material. The multiple ultra cleaner shook the material intensively, and short fibres and core were separated from the long fibres. This method could clean fibre with remaining impurity content to <2%, meeting the demands of most industrial fiber applications. Another popular method to remove core is scutching. This method was established for retted hemp.

2.5.3. Biological Method

Retting is a biological process, a practice for separating fibre from the plant. During the retting process microbiological digestion of chemical bonds occurs between fibre and core (Bruce et al. 2001). In this process bacteria (predominantly *Clostridia* species) release enzymes to degrade pectin and hemicellulosic compounds between the individual fibre cells (Di Candilo et al. 2000). This results in the separation of the bast fibres from the woody core. The retting process requires abundant quantities of water and produces a more uniform and higher quality fibre (Morrison et al. 2000), but is not generally practiced because of environmental pollution problems (Keller et al. 2001). It also increases the risk of rotting, fungal or mold attack (Münder et al. 2004). The number of days for retting is important as over retting may damage the fibre quality. Usually, in the retting process fibre plants are submerged into a non-turbulent source of water for approximately 8 to 14 days (Hann 2005).

Another biological treatment is fungal treatment. Some fungi such as white-rot fungi (*Basidiomycotina*) are responsible for some of the most destructive forms of wood degradation (Walker 1993a). They usually remove cell wall constituents (lignin, hemicelluloses, and cellulose) and physically modifying the fibre wall for improved fibre/matrix interfacial bonding.

2.5.4. Chemical Method

Fibre separation process using chemicals play an important role in improving the surface properties of fibres. The most popular treatments include the use of alkalis, anhydrides and anhydride-modified copolymers, silanes and isocyanates. Some alkali treatments, performed at high temperatures, result in selective degradation of lignin, pectin and hemicelluloses in the fibre wall, while having little effect on the cellulose components (Walker 1993b). The removal of these cementing materials helps to produce stronger natural fibre. According to Wang et al. (2003) pectin and hemicelluloses can be easily removed, but lignin in hemp bast fibre can be difficult to remove. Alkali fibre treatments using sodium hydroxide (NaOH) can completely remove the pectins in the hemp fibre, but the rate of lignin removal is dependent on the NaOH concentration (Wang et al. 2003). Wang et al. (2003) also reported that that a combination of NaOH and sodium sulphite (Na2SO3) can be used to remove lignin effectively from hemp fibre.

2.6. DISCRETE ELEMENT METHOD (DEM)

The discrete element method (DEM) is a numerical modeling method introduced by Cundall (1971 and 1974) cited by Cundall and Strack (1979). DEM was originally developed to analyze rock mechanics problem. In DEM materials are represented as finite sized particles and the bulk behavior of the material is monitored by the motion of each particle at their contact point with other particles or the boundary. Later the DEM was used to describe the behavior of granular assemblies (soil) by Cundall and Strack (1979). Since then the DEM has been used in different applications including grain (Lu et al. 1997; Sakaguchi et al. 2001), cohesive materials, such as soil (van der Linde 2007), and manure (Landry et al. 2006b).

2.6.1. DEM Modeling Tool

Particle flow code in three dimensions (PFC^{3D}) is a commercial code based on the DEM, developed by Itasca Consulting Group, Inc., Minneapolis, MN (Itasca 2008).

2.6.2. PFC^{3D} Basics

In a PFC^{3D} model, hemp or other materials are treated as an assembly of particles. The basic particles in PFC^{3D} models are rigid and spherical, named "balls". As hemp materials (fibre bundles or cores) are not spherical in shape, these materials may be constructed using a set of balls to better represent the shapes. A machine surface, such as a screen deck of a separator can be constructed with "walls" in PFC^{3D}, and the motion of a machine can be specified in PFC^{3D} as well. Balls and walls, referred as to entities, contact with one another through the forces that arise at contacts. The contact can be

formed between balls (named as ball-ball contacts) and between balls and walls (named as ball-wall contacts), as shown in Figs. 2.3(a,b). In a PFC^{3D} model, the following assumptions are made for particles/balls and their interactions (Itasca 2008):

1. The particles are treated as rigid bodies.
2. The contacts between entities occur over a vanishingly small area (i.e., at a point).
3. Behavior at the contacts uses a soft-contact approach where the rigid particles are allowed to overlap with one another at contact points.
4. The magnitude of the overlap is related to the contact force via the force-displacement law, and all overlaps are small in relation to particle sizes.
5. Bonds can exist at contacts between particles.
6. All particles are spherical. However, the clump logic supports the creation of super-particles of arbitrary shape. Each clump consists of a set of overlapping particles that act as a rigid body with a deformable boundary.

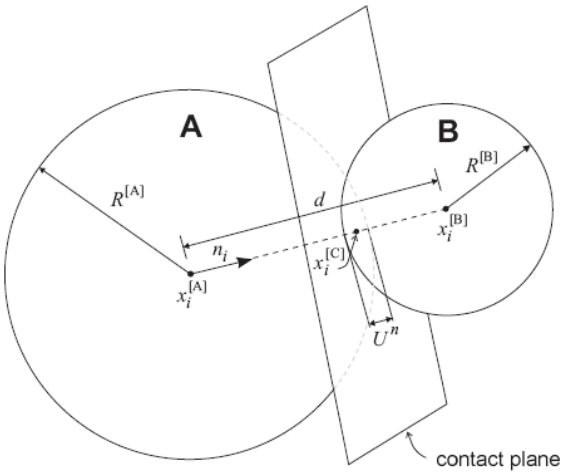

(a)

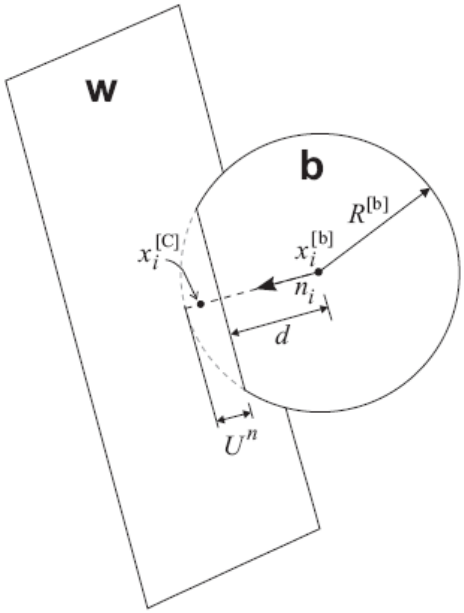

(b)

Fig. 2.3. Contacts of entities in PFC^{3D} models; (a) ball-ball contact; (b) ball-wall contact. n_i = unit normal of the contact plane; U^n = overlap, relative contact displacement in the normal direction; $x_i^{[A]}$, $x_i^{[B]}$, and $x_i^{[b]}$ = the position vectors of the centres of Ball A, Ball B, and Ball b, respectively; $x_i^{[C]}$ = location of the contact point; d = the distance between the centres of entities; R = radius of ball (Itasca 2008).

The relationship between particle motion and the force causing motion is governed by Newton's laws of motion. The mechanical behaviour of the material modeled is predicted in terms of the movement of each particle and the inter-particle forces acting at each contact point. The contact force between entities is calculated by

$$F_i = F_i^n + F_i^s \tag{2.2}$$

where

F_i = contact force vector (N),

F_i^n = normal component vector of the contact force (N),

F_i^s = shear component vector of the contact force (N).

2.6.3. PFC^{3D} Contact Models

Depending on the properties of two contact entities, all the contacts are assigned with any of the two models: linear model and Hertz model. To construct virtual material with PFC^{3D} particles (balls), one needs to determine what kind of interactions should occur between balls. In PFC^{3D} the behavior of the particle during interaction is described by three different component behaviours: Stiffness, Slip, and Bonding. The linear model provides constant stiffness, sliding behavior and contact-bond behavior. A parallel bond component can be used in bonding behavior. The Hertz-Mindlin contact model is a nonlinear contact formulation based on approximation of the theory of Mindlin and Deresiewicz (1953) cited by Cundall (1988). The Hertz model is defined by two parameters: Shear modulus (G) and Poisson's ratio (υ) of the two contacting balls. The Hertz model provides only sliding and stiffness behaviour. These behaviors vary as a function of elastic constants of the two contacting entities, overlap and normal force.

Hertz-Mindlin model cannot be used for the contact bond as the model was not defined for balls that are not in tension, however a parallel bond component can be added where the user to discern the usefulness of such a system. The component behavior of the contact models are described below.

2.6.3.1. Stiffness

In the constant stiffness model, there are no bonds between individual balls and the contact force and deflection between balls are governed by the stiffness of the balls. The contact stiffness is defined by the normal and shear stiffness k_n and k_s of the two contacting entities. In the linear contact model the contact stiffness are calculated by assuming that the stiffness of two contacting entities act in series and can be expressed by the following equation

The contact normal secant stiffness

$$K^n = \frac{k_n^{[A]} k_n^{[B]}}{k_n^{[A]} + k_n^{[B]}} \tag{2.3}$$

and the contact shear secant stiffness

$$k^s = \frac{k_s^{[A]} k_s^{[B]}}{k_s^{[A]} + k_s^{[B]}} \tag{2.4}$$

where

k^n = contact normal stiffness (N m-^{1}),

k_n = ball normal stiffness (N m-^{1}),

k^s = contact shear stiffness (N m-^{1}),

k_s = ball shear stiffness (N m-^{1}),

the superscripts A and B refer to the two entities in contact.

In Hertz-Mindlin model the contact stiffness is given by

$$K^n = \left(\frac{2\langle G \rangle \sqrt{2\tilde{R}}}{3(1-\langle \upsilon \rangle)} \right) \sqrt{U^n} \tag{2.5}$$

and the contact shear secant stiffness is given by

$$k^s = \left(\frac{2\left(\langle G \rangle^2 3(1-\langle \upsilon \rangle)\tilde{R}\right)^{1/3}}{2-\langle \upsilon \rangle} \right) \left| F_i^n \right|^{1/3} \tag{2.6}$$

where

$\left|F_i^n\right|$ = the magnitude of the normal contact force (N),

G = the shear modulus (MPa),

υ = Poisson's ratio.

The contact stiffness is related to the contact force and relative displacement of each contact point and the contact stiffness is expressed in normal and shear directions using the following equations.

Normal stiffness:

$$F_i^n = K^n U^n n_i \tag{2.7}$$

Shear stiffness:

$$\Delta F_i^s = -k^s \Delta U_i^s \tag{2.8}$$

where

F_{in} = total normal force,

ΔF_i^s = the increment of shear force,

K_n) = normal secant (symbolized by a capital letter) stiffness,

k_s = tangent stiffness (symbolized by a small case letter),

U^n = total normal displacement,

ΔU_i^s = increment of shear displacement,

n_i = the unit normal vector to the contact plane,

2.6.3.2. Slip

The Slip Model is similar to the Stiffness Model, but it allows two contacting entities to slip relative to one another. The slip behavior is defined by the friction coefficient (μ) at the contact of two entities and occurs by limiting the shear force provided no normal strength in tension. If the overlap between the contacts is less than or equal to zero, the maximum allowable shear contact force is

$$F_{\max}^s = \mu \left| F_i^n \right| \tag{2.9}$$

The slip will occur, if $\left| F_i^s \right| > F_{\max}^s$.

The Stiffness and Slip Models are more suitable for simulations of free flowing granular materials. The Contact Model allows users to add bonds between balls to connect them together. This model is more suitable for the simulation of cohesive materials.

2.6.3.3. Bonding

PFC^{3D} allows for two different bonding among balls: Contact Bond and Parallel Bond. In both models, bonds are envisioned as a kind of "glue" joining the balls. The glue of the Contact Bond acts only at the contact point (Fig. 2.4a), while the glue of the Parallel-Bond acts over a circular cross-section (disk) lying on the contact plane between the balls (Fig. 2.4b). The former model can transmit only forces, while the latter model can transmit both forces and moments (Fig. 2.4c).

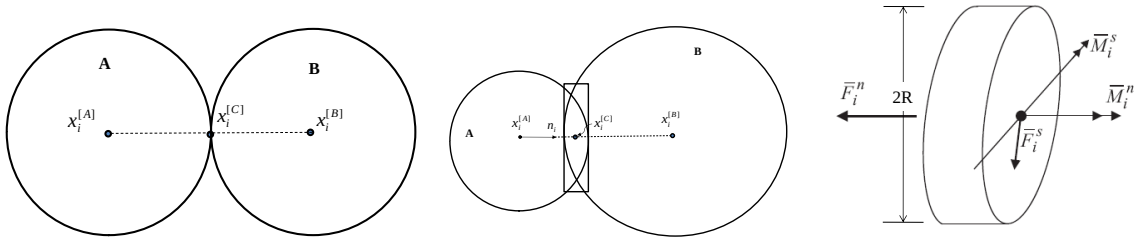

(a) (b) (c)

Fig. 2.4. PFC^{3D} Contact model; (a) Contact bond between two balls, (b) Parallel bond between two balls and (c) Parallel bond force-displacement behavior. n_i = unit normal of the contact plane; $x_i^{[A]}$ and $x_i^{[B]}$ = the position vectors of the centres of Ball A and Ball B; $x_i^{[C]}$ = location of the contact point; $\overline{F}_i^n$, $\overline{M}_i^n$ and $\overline{F}_i^s$, $\overline{M}_i^s$ = normal and shear component vectors of force and moment respectively; $\overline{R}$ = bond disc radius (Itasca 2008).

A contact bond can be envisioned as a pair of elastic springs with constant normal and shear stiffness acting at the contact point. These two springs have specified shear and tensile normal strengths and expressed as normal contact bond strength (F_c^n) and shear

contact bond strength (F_c^s). If the magnitude of the tensile normal contact force equals or exceeds the normal contact bond strength, the bond breaks, and both the normal and shear contact forces are set to zero. If the magnitude of the shear contact force equals or exceeds the shear contact bond strength, the bond breaks, but the contact forces are not altered, provided that the shear force does not exceed the friction limit, and provided that the normal force is compressive.

A parallel bond can be envisioned as a set of elastic springs with constant normal and shear stiffness, uniformly distributed over a circular cross-section lying on the contact plane and centered at the contact point. These springs act in parallel with the point-contact springs that are used to model particle stiffness at a point. A parallel bond is defined by the following five microparameters: normal and shear stiffness $\bar{k}^n$ and $\bar{k}^s$; normal and shear strength, $\bar{\sigma}_c$ and $\bar{\tau}_c$; and bond disk radius, R. The maximum tensile $(\sigma_{\max})$ and shear $(\tau_{\max})$ stresses acting on the bond periphery were calculated using the following equations (Itasca 2008):

$$\sigma_{\max} = \frac{-\bar{F}^n}{A} + \frac{\left|\bar{M}_i^s\right|}{I}\bar{R} \tag{2.10}$$

$$\tau_{\max} = \frac{\left|\bar{F}_i^s\right|}{A} + \frac{\left|\bar{M}^n\right|}{J}\bar{R} \tag{2.11}$$

where

A = area of the bond disk,

J = polar moment of inertia of the disk cross-section,

I = moment of inertia of the disk cross-section about an axis through the contact point,

$\overline{F}_i^n$, $\overline{F}_i^s$ = normal and shear component vectors of force,

$\overline{M}_i^n$, $\overline{M}_i^s$ = normal and shear component vectors of moment.

The parallel bond breaks if the maximum tensile stress exceeds the normal strength $\left(\sigma_{\max} \geq \overline{\sigma}_c\right)$, or the maximum shear stress exceeds the shear strength $\left(\tau_{\max} \geq \overline{\tau}_c\right)$ (Potyondy and Cundall 2004).

2.7. PFC^{3D} MODEL PARAMETERS

The PFC^{3D} Stiff Model requires two model parameters: ball normal stiffness (k_n) and shear stiffness (k_n). The PFC^{3D} Slip Model requires an additional parameter: ball-ball and ball-wall friction coefficient (μ). The PFC^{3D} Bond Models require several more parameters on the bond, such as bond normal strengths (σ) and shear strengths (τ); bond normal stiffness ($\overline{k}^n$) and shear stiffness ($\overline{k}^s$), and Radius multiplier (λ).

One of the challenges of using PFC^{3D} is to specify the model parameters which can significantly affect the model results (Mishra and Murty 2001). There is no robust method for determining the model parameters, and the best methods are calibrations. However, it is not possible to calibrate all parameters at the same time. Thus, assumptions of some parameters are required while other parameters are to be calibrated. This implies that the determination of model parameters is subjective, as long as the

selected model parameters result in the behavior of the model particles matching with those of the real material modeled.

2.8. SELECTION OF MODEL PARAMETER

Direct modeling can be done based on the known properties. This is only applicable if the materials are spherical in shape. The relative importance of the various input parameter depends on the type of simulation and the aspects of interest in the resulting behavior. The common method is the inverse method. In this method parameters are determined by matching model result with the test result.

2.8.1. Particle Stiffness

Particle stiffness is expressed as force per unit length which is representing the deformability of material at each particle-particle contact. This deformability refers to the Young's modulus of the particle and the ratio of particle normal to shear stiffness (k_n/k_s). The moduli are chosen to match the Young's modulus and the ratios of normal to shear stiffness are chosen to match the Poisson's ratio (Potyondy and Cundall 2004). In order to reduce the number of free parameters, the ratio of normal to shear stiffness is often set to a value. Asaf et al. (2007) assumed normal stiffness is equal to shear stiffness (k_n/k_s = 1). Similar value was reported by van der Linde (2007), McDowell and Harireche (2002), and Coetzee et al. (2007) in their models. Other values were also used by different researchers, such as k_n/k_s =2.5 (Potyondy and Cundall 2004); k_n/k_s = 5 (Camusso and Barla 2009).

Asaf et al. (2007) indicated that the equation proposed by Liao and Chang (1997) can be used as a preliminary estimation of k_n.

$$K_n = \frac{\pi R E_c (1+e)}{(1-2\upsilon) C_n} \tag{2.12}$$

Where

e = void ratio,

C_n = average number of contact per particle in the model,

R = radius of the particle,

E_c = Young's modulus,

υ = Poisson's ratio.

Potyondy and Cundall (2004) proposed following relationship for assuming the value of normal stiffness (k_n):

$$K_n = 4RE_c \tag{2.13}$$

2.8.2. Friction Coefficient

Particle friction coefficient (μ) is another important parameter. Potyondy and Cundall (2004) reported that the particle friction coefficient appears to affect only post peak response and used μ = 0.5 as a non zero value. Same value used by van der Linde (2007) and Potyondy and Cundall (2004). Many researchers used the particle friction coefficient value between 0-1, for example, μ = 0.3 (Djordjevic 2003); μ = 0.4 (Yang et al. 2006); μ = 0.7 (Yan and Ji 2010; Mishra and Murty 2001), and μ = 2.1 (Camusso and Barla 2009)

2.8.3. Bond Stiffness

Bond normal and shear stiffness **(** $\bar{k}_n$ and $\bar{k}_s$ **)** can be calculated using the same method as particle stiffness. Only some modification is required during the stiffness calculation. Potyondy and Cundall (2004) proposed following relationship for assuming the value of bond normal stiffness:

$$\bar{k}_n = \bar{E}_c / \left(R_a + R_b\right) \tag{2.14}$$

Where R is the radius of the particle and the superscripts a and b refer to the two entities in contact.

Similar to the particle stiffness the ratio of bond normal to shear stiffness is often set to a value. Potyondy and Cundall (2004) used $\bar{k}_n / \bar{k}_s$ = 2.5. Mndlin (1949) cited by Cundall and Strack (1979) reported a range from 1 to 1.5 for the ratio of $\bar{k}_n / \bar{k}_s$ for elastic bodies in contact with elliptical contact areas. In simulating the soil-tool interaction in a sub-soiling application, van de Linde (2007) used $\bar{k}_n / \bar{k}_s$ = 1.

2.8.4. Bond Normal and Shear Strength

Again the bond normal and shear strength ratio requires to be set as a value in order to reduce the number of free parameter. Potyondy and Cundall (2004) suggested to use $\bar{\sigma} = \bar{\tau}$ to allow both tensile and shear microfailures. For some cases bond normal and shear strengths can be calculated theoretically. In determining the particle bond strengths

for cohesive soil, the $\bar{\sigma}$ can be assumed to be the soil intrinsic stress, and the $\bar{\tau}$ can be assumed to be the soil cohesion. Internal tensile stresses exist between soil particles are caused by the water under tension between particles (Upadhyaya et al. 1994; Zhang and Li 2006) and soil intrinsic stress is the function of cohesion and internal friction angle as: c cotφ (McKyes 1985). Thus,

$$\bar{\sigma} = c \cot\varphi \tag{2.15}$$

$$\bar{\tau} = c \tag{2.16}$$

2.8.5. Radius Multiplier

Radius Multiplier used to determine the radius of the parallel bond disc. Radius multiplier is such that parallel-bond radius equals to the multiplier times the minimum radius of the two bonded balls. The range of radius multiplier varies from 0 to 1. The material will behave like granular material if the value is set to zero ($R = 0$); if the value is set to one ($R = 1$) the bonded material will be "cemented" completely between bonded particle. Any value between 0 and 1 can be chosen depending on the model requirement. Many researchers used the medium value of radius multiplier ($R = 0.5$) (Potyondy and Cundall 2004; Potyondy 2007).

2.9. DEM APPLICATION IN BONDED PARTICLE MATERIAL

Basic DEM models have been developed for the spherical particles; however most of the natural products are not in spherical shape. DEM allows simulating more realistic material shapes by aggregating individual particle or spheres bonded together. These

aggregated bonded particles may either be a clump or a cluster. Modeling using clumps is more suitable for the material with complex shape (eg. grain) and modeling using clusters is suitable for both complex shape material and cohesive medium (eg. soil; fibre). Many studies successfully used clumps (Cho et al. 2007; Ning et al. 1997; Cheng et al. 2003; Lu et al. 2007, Salot et al. 2008) and clusters (Jensen et al. 1999; Landry et al. 2006a) to simulate the behaviours of materials with complex shapes.

Potyondy and Cundall (2004) describe the bonded particle model (BPM) for rocks. That study revealed that rocks behaved more like a complex shaped cemented granular material where both the grain and cement are deformable. BPM is capable to reproduce the significant physical mechanism of the rock.

Yang et al. (2006) studied the effect of microparameters on macroproperties of bonded particle specimens. A theoretical and discrete element simulation was used to determine the relationship between microparameters and macroproperties of bonded particle. Microparameters include geometric and physical parameters which determine the dimension of the specimen, particle size and particle numbers and the constitutive parameters to define the contacts and bonds. Macroproperties are the physical response of the material.That study reported that microparameters had significant effects on the macroproperties of the parallel bonded specimen.

2.10. SUMMARY

From the above literature it is clear that hemp fibre has high potential to contribute to the world economy in a sustainable manner by producing environment friendly products. Thus the development of suitable equipment for hemp fibre processing is essential and understanding the mechanical behavior is a prerequisite. DEM could be a useful simulation tool to understand the mechanical behavior of hemp processing. This knowledge will help to design suitable equipment.

The literature also clearly indicates that different contact models in PFC^{3D} are useful for understanding the mechanical behavior of the hemp materials. To use these contact models a set of microparameters for hemp material (fibre and core) are required to be calibrated. In PFC^{3D} behaviour of hemp fibre and core can be simulated using a bonded model (parallel bond) and cluster logic in PFC^{3D}. Results can be used to simulate the performance of fibre processing equipment.

2.11. REFERENCES

Anandarajah, A. 1994. Discrete-element method for simulating behaviour of cohesive soil. *Journal of Geotech. Engineering*, 120(9): 1593-1613.

Anthony, W.S. 2002. Separation of fiber from seed flax straw. *Applied Engineering in Agriculture* 18: 227-233.

Asaf, Z., D. Rubinstein and I. Shmulevich. 2007. Determination of discrete element model parameters required for soil tillage. *Soil and Tillage Research* 92(2): 227-242.

ASTM. 2007. Standard test method for length of fibre in wool top. Annual book of ASTM standards. Vol.07.01, D 519-04. American Society of Testing Methods. West Conshohocken, PA.

Baritelle, A.L. and G.M. Hyde. 1999. Effect of tuber size on failure properties of potato tissue. *Transactions of the ASAE*, 42(1): 159-161.

Beckermann, G. 2007. Performance of hemp-fibre reinforced polypropylene composite materials. Unpublished PhD Thesis. Materials and Process Engineering, Private Bag, Hamilton University of Waikato.

Bledzki, A. K., S. Reihmane, and J. Gassan. 1996. Properties and modification methods for vegetable fibers for natural fiber composites. *Journal of Applied Polymer Science* 59(8): 1329–1336.

Bocsa, I. and M. Karus. 1997. The cultivation of hemp, Sebastopol, California: Chelsea Green Publishing Company.

Bos, H.L., M.J.A. Van Den Oever and O.C.J.J. Peters. 2002. Tensile and compressive properties of flax fibres for natural fibre reinforced composites. *Journal of Materials Science* 37: 1683-1692.

Bruce, D. M., R. N. Hobson, R. P. White and J. Hobson. 2001. Stripping leaves and flower heads to improve the harvesting of hemp fibre. *Journal of Agricultural Engineering Research* 78(1): 43-50.

Camusso, M and M. Barla. 2009. Microparameters calibration for loose and cemented soil when using particle methods. *International Journal of Geomechanics* 9(5): 217-229.

Chen, Y., J. Liu and J. Gratton. 2004a. Engineering perspectives of hemp plant, harvesting and processing in Canada – A review. *Journal of Industrial Hemp* 9(2): 23-39.

Cho, N., C.D. Martin and D.C. Sego. 2007. A clumped particle model for rock. *International Journal of Rock Mechanics and Mining Science* 44(7): 997-1010.

Coetzee CJ, A.H. Basson and P.A. Vermeer. 2007. Discrete and continuum modeling of excavator bucket filling. *Journal of Terramechanics* 44: 177-186.

Correia, F., D.N. Roy and K. Goel. 1998. Pulping of Canadian industrial hemp. Pulp and Paper Canada. 99(9): 39-41.

Cundall, P. A. 1971. A computer model for rock-mass behavior using interactive graphics for the input and output of geometrical data. Report MRD -2-74 prepared at the University of Minnesota under contract no DACW 45-74-C-006, for the Missouri river division, US Army corps of Engineers, available from National Technical Information Service – report no AD/A-001 602.

Cundall, P. A. 1971. A Computer Model for Simulating Progressive Large Scale Movements in Blocky Rock Systems," in *Proceedings of the Symposium of the International Society of Rock Mechanics*; Vol. 1, Paper No. II-8. Nancy, France.

Cundall, P.A. and O.D.L. Strack. 1979. A discrete numerical model for granular assemblies. *Geotechnique* 29: 47-65.

de Meijer, E.P.M. 1995. Fibre hemp cultivars: A survey of origin, ancestry, availability and brief agronomic characteristics. *Journal of the international hemp association* 2(2): 66-73.

Di Candilo, M., P. Ranalli, C. Bozzi, B. Focher, and G. Mastromei. 2000. Preliminary results of tests facing with the controlled retting of hemp. *Industrial Crops and Products* 11(2-3): 197-203.

Djordjevic, N. 2003. Discrete element modeling of the influence of lifters on powder draw of tumbling mills. *Minerals Engineering* 16: 331-336.

Doberczak, A., St. Dowgielewicz and W. Surek. 1964. Cotton, Bast and Wool Fibres (Translated from Polish). Published for department of agriculture and National science foundation, Washington D.C. Warszawa, Poland.

Feed Machinery. 2008. Feed Mill Machinery and Equipment. www.feedmachinery.com (2008/01/15).

Fortenbery, T. R. and M. Bennett. 2003. Opportunities for commercial hemp production. *Review of agricultural Economics* 26(1): 97-117.

Furll, C. and H. Hempel. 2000. Optimization of a new machine for fibre processing by impact stress. Research report, Postdam-Bornim, Germany: Institute fur Agrartechnic.

Gan-Mor, S. and N. Galili. 2000. Rheological model for fruit collision with an elastic plate. *Journal of Agricultural Engineering Research* 75: 139-147.

Garcia-Jaldon, C., D. Dupeyre, and M.R. Vignon. 1998. Fibres from semiretted hemp bundles by steam explosion treatment. *Biomass and Bioenergy* 14(3): 251-260.

Gratton, J. L. 2002. Design and evolution of an on-field hemp fibre processing machine. Unpublished M. Sc. Thesis. Winnipeg, MB: Department of Biosystems Engineering, University of Manitoba.

Gratton, J. L. and Y. Chen. 2004. Development of field-going unit to separate fibre from hemp (Cannabis sativa) stalk. *Applied Engineering in Agriculture* 20(2):139-145.

Gupta, A. and D.S. Yan. 2006. Roll crusher. In Mineral processing design and operation. 142-160. Amsterdam, The Netherlands: Elsevier.

Hann, M.A. 2005. Innovation in linen manufacture. *Textile progress* 37(3):1-42.

Hobson, R. N.; D. G. Hepworth; D. M. Bruce. 2001. Quality of fibre separated from unretted hemp stems by decortication. *Journal of agricultural Engineering Research* 78 (2): 153-158.

Itasca. 2008. PFC^{3D} particle flow code in 3 dimensions, theory and background. Itasca Consulting Group, Inc. Minneapolis, Minnesota, USA.

Jensen, R.P., P.J. Bosscher, M.E. Plesha, and T.B. Edil. 1999. DEM simulation of granular media-structure interface: effects of surface roughness and particle shape. *International Journal for Numerical and Analytical Methods in Geomechanics* 23: 531-547.

Keller, A., M. Leupin, V. Mediavilla, and E. Wintermantel. 2001. Influence of the growth stage of industrial hemp on chemical and physical properties of the fibres. *Industrial Crops and Products* 13(1): 35-48.

Kirby, R.H. 1963. Vegetable Fibres. Botany, Cultivation and Utilization. Leonard Hill Ltd. London.

Kymäläinen, H.R. 2004. Quality of *Linum usitissimum* L. (flex and linseed) and *Cannabis sativa* L. (hemp fibre) during the production chain of fibre raw material for thermal insulation. Unpublished academic dissertation. Helsinki, Finland: Department of Agricultural engineering and household technology, University of Helsinki.

Landry, H., C. Laguë and M. Roberge. 2006a. Discrete element representation of manure products. *Computers and Electronics in Agriculture* 51: 17-34.

Landry, H., F. Thirion, C. Laguë and M. Roberge. 2006b. Numerical modeling of the flow of organic fertilizers in land application equipment. *Computers and Electronics in Agriculture* 51: 35-53.

Liao, C.L. and C.S. Chang. 1997. Stress strain relationship for granular material based on the hypothesis of best fit. *International journal of solid structure* 34(31): 4087-4100.

Liu SH, D. Sun and H. Matsuoka. 2005. On the interface friction in direct shear test. *Computers and Geotechnics* 32: 317–325.

Lu, M. and G.R. McDowell. 2007. The importance of modelling ballast particle shape in the discrete element method. *Granular matter* 9:69-80.

Lu, Z., S.C. Negi and J.C. Jofriet. 1997. A numerical model for flow of granular materials in silos. Part 1: model development. *Journal of Agricultural Engineering Research* 68: 223-229.

MAFRI. 2011. Industrial hemp. http://www.gov.mb.ca/agriculture/crops/hemp/bko01s00.html (2011/02/14).

McDowell, G.R. and O. Harireche. 2002. Discrete element modelling of yielding and normal compression of sand. *Géotechnique* 52(4): 299-304.

McKyes E. 1985. Soil Cutting and Tillage. New York: Elsevier Scientific Pub. Co.

Merfield, C.N. 1999. Industrial hemp and its potential for New Zealand. Annual report. Caterbury, New Zealand: Kellogg Rural Leadership Course.

Mishra, B. K., and C. V. R. Murty. 2001. On the determination of contact parameters for realistic DEM simulations of ball mills. *Powder Technology* 115: 290-297.

Morrison, W.H., D.D. Archibald, H.S.S. Sharma, and D.E. Akin. 2000. Chemical and physical characterization of water- and dew-retted flax fibres. *Industrial crops and products* 12: 39-46.

Munder, F. and C. Fürll. 2004. Effective processing of bast fiber plants and mechanical properties of the fibers. ASAE/CSAE Annual International Meeting, Ottawa, Ontario, Canada.

Munder, F. C. Fürll and H. Hempel. 2004. Results of an advanced technology for decortication of hemp, flax and linseed. *Molecular Crystals and Liquid Crystals* 418: 165/[893]–179/[907].

Mwaikambo, L. Y. 2006. Review of the history, properties and application of plant fibres. *African journal of science and technology* 7(2): 120-133.

Netravali, A. N. and S. Chabba. 2003. Composites get greener. *Materials Today* 6: 22–29.

Ning, Z., R. Boerefijn, M. Ghadiri and C. Thornton. 1997. Distinct element simulation of impact breakage of lactose agglomerates. *Advanced Powder Technology* 8: 15-37.

OMAFRA. 2011. Growing Industrial Hemp in Ontario. http://www.omafra.gov.on.ca/english/crops/facts/00-067.htm (2011/02/14).

Potyondy, D.O. 2007. Simulating stress corrosion with a bonded-particle model for rock. *International Journal of Rock Mechanics and Mining Science* 44:677-691.

Potyondy, D.O. and P.A. Cundall. 2004. A bonded-particle model for rock. *International Journal of Rock Mechanics & Mining Sciences* 41(8): 1329-1364.

Rowell, R.M., J.S. Han and J.S. Rowell. 2000. Characterization and Factors Effecting Fiber Properties. Natural Polymers and Agrofibers Composites. 115-134. ISBN: 85-86463-06-X.

Sakaguchi, F., M. Suzuki, J.F. Favier and S. Kawakami. 2001. Numerical simulation of the shaking separation of paddy and brown rice using the discrete element method. *Journal of Agricultural Engineering Research* 79(3): 307-315.

Salot, C., P. Gotteland and P. Villard. 2009. Influence of relative density on granular materials behavior: DEM simulations of triaxial tests. *Granular Matter* 11(4): 231-236.

Upadhyaya, S.K., W.J. Chancellor, J.V. Perumpral, R.L. Schafer, W.R. Gill and G.E. VandenBerg. 1994. Advances in Soil Dynamics. ASAE Monograph Number 12. St. Joseph, MI: ASABE;

Van der Linde, J. 2007. Discrete element modeling of a vibratory subsoiler. Matieland, South Africa: Department of Mechanical and Mechatronic Engineering, University of Stellenbosch.

Van Wyk, L. 2007. The application of natural fibre composites in construction: a research case study. In *Sixth International Conference on Composite Science and Technology,* ICCST/6, Durban, South Africa.

Vignon, M.R., D. Dupeyre, and C. Garcia-Jaldon. 1996. Morphological characterization of steam-exploded hemp fibers and their utilization in polypropylene-based composites. *Bioresource Technology* 58(2): 203-215.

Walker, J.C.F. 1993a. Timber preservation, in Primary Wood Processing. Chapman and Hall: London. 285-289.Walker, J.C.F. 1993b. Wood chemistry and cell wall ultrastructure, in Primary Wood Processing. Chapman and Hall: London. 44-51.

Wambua, P., J. Ivens, and I. Verpoest. 2003. Natural fibres: can they replace glass in fibre reinforced plastics? *Composites Science and Technology* 63(9):1259-1264.

Wang, H.M., Postle, R., Kessler, R.W., and Kessler, W. 2003. Removing pectin and lignin during chemical processing of hemp for textile applications. *Textile Research Journal* **7**3(8): 664-669.

Webber III, C., V. K. Bledsoe, and R. E. Bledsoe. 2002. Kenaf harvesting and processing. In Trends in New Crops and New Uses, eds. J. Janick and A. Whipkey. Alexandria, VA: ASHS Press.

Xu, B., B. Pourdeyhimi and J. Sobus. 1993. Fibre cross-sectional shape analysis using image processing technique. *Textile Research Journal* 63(12): 717-730.

Yan, Y. and S. Ji. 2010. Discrete element modeling of direct shear tests for a granular material. *International Journal for Numerical and Analytical Methods in geomechanics* 34: 978-990.

Yang, B., Y. Jiao and S. Lei. 2006. A study on the effect of microparameters on macroproperties for specimens created by bonded particles. *Engineering Computations: International journal for computer aided engineering and software* 23(6): 607-631.

Zhang, R. and J. Li 2006. Simulation on mechanical behavior of cohesive soil by Distinct Element Method. *Journal of Terramechanics* 43: 303–316.

Chapter 3

Characterization of the Shear Properties of Hemp Fibre and Core using Discrete Element Method

3.1. SIGNIFICANCE

The basic properties of the hemp material are important for understanding the hemp processing during fibre production. For simulating the hemp processing using discrete element method (DEM), selection of appropriate PFC^{3D} model microproperies is essential. From the literature review it was found that no one has reported the model microproperties for hemp fibre and core. The first step of the research reported here was to measure the hemp shear properties using direct shear test and use the measured results in determining the particle microproperies for the hemp fibre and core. The following manuscript details this first step. It corresponds to the objective 1 of the thesis. The content of this chapter was published (***M. A. Sadek,*** *Y. Chen, C. Laguë, H. Landry, Q. Peng, and W. Zhong. 2011****.*** *Characterization of the Shear Properties of Hemp using Discrete Element Method. Trans. Of the ASABE 54(6): 2279-2285*). The simulation and the writing of the manuscript were done by the candidate while the co-authors, Drs. Chen, Laguë, Landry, Peng, and Zhong, reviewed it. A peer-reviewing process was involved in the publication of the manuscript. Three reviewers submitted comments prior to the acceptance of the manuscript. The reviewers recognized the original work presented in the manuscript and its importance to the understanding of shear properties of

hemp and to establish the PFC^{3D} particle microproperties for hemp fibre and core. Because the work presented in this chapter was published before the submission of the thesis, the content of the published article is similar to the published article.

3.2. ABSTRACT

Processing of hemp for fiber involves mechanical separation of the outer fiber layer from the inner core of the hemp stem. Existing processing equipment is often not effective due to lack of information on the mechanical properties of hemp fiber and core. In this study, direct shear tests of hemp fiber and core were performed to measure the yield strength, cohesion, and internal friction of these two materials. The materials were ground into small particles before testing. A numerical model was also developed to simulate the direct shear tests using PFC^{3D} (Particle Flow Code in Three Dimension), a discrete element software. The model consisted of an assembly of spherical model particles (diameter: 2 mm) which represented ground fiber and core particles. The particle assembly was virtually sheared under different normal loads to obtain the shear properties of the model particles: yield strength, cohesion, and internal friction. The microproperties (particle friction and stiffness) of model particles were calibrated using the measurements from the direct shear tests. The calibrated values of normal stiffness and shear stiffness were 5e4 N/m for the ground fiber, and 8e4 N/m for the ground core and the calibrated friction coefficient of particle was 1.0 for both the ground fiber and core. The shear properties simulated with the model were validated with the measurements and they agreed well with the measurements in most cases.

3.3. INTRODUCTION

Industrial hemp has become one of the best commercial cash crops in Canada, because hemp fiber can be used in many applications, including textile, bio-composites, and building materials. These applications demand large quantities of hemp fiber. Therefore, processing hemp for fiber has become a priority for fiber industries. A typical hemp processing machine generates bast fiber (the outer layer of hemp plant stem) as the product and core (the inner layer of hemp stem) as by-product. Hemp processing involves a mechanical process to separate fiber from the core by shearing, impacting, and compressing of hemp stalk, using machines such as roll crushers and hammer mills. The output of these machines is a mixture of fibers and cores. A subsequent process is required to remove the separated core from the mixture to obtain pure (clean) fibers, using machines such as rotary screens and carders. Most of these hemp processing machines were adopted from other applications, such as mining, food, and cotton industries. For fiber processing, these machines are either not efficient in terms of processing capacity, or not effective, in terms of fiber purity. Therefore, development of more effective and efficient machines is required. The first step is to study mechanical and physical properties of hemp material, as any machine development is tailored by properties of the material to be handled.

This study was aimed at determining the shear properties (yield strength, internal friction, and cohesion) of hemp fiber and core using direct shear test. Direct shear test is one of the common laboratory methods to measure material shear properties and it has been used to test many bio-materials. For example, Afzalinia and Roberge (2007) used direct

shear tests to determine the physical and mechanical properties of selected forage materials at different cut lengths and observed that the angle of internal friction had an effect on different cut lengths. Opoku et al. (2007) used direct shear tests to observe the frictional properties of chemically treated flax and found that chemical treatment had effect on the internal friction angle. However, no studies were found on shear properties of hemp materials.

Direct shear test can be simulated by using numerical modeling to further understand mechanical behaviors of material under shear. Numerical modeling can be performed using Finite Element Method (FEM) and Discrete Element Method (DEM). The DEM is a new numerical modeling method proposed by Cundall and Strack (1979). In the DEM, material to be simulated is treated as an assembly of individual particles. The method uses contact mechanics between particles to simulate the dynamics of the particles in the assembly (Cundall 1988). As compared with the FEM, the DEM can describe detail interactions between any individual particles and this method can deal with larger displacement of particles. PFC^{3D} (Particle Flow Code in Three Dimension) by Itasca Consulting Group, Inc., Minneapolis, MN is a widely used commercial simulation tool developed based on the theory of the DEM. PFC^{3D} has been successfully applied to rock (Potyondy 2007), soil (Ni et al. 2000), powders (Djordjevic 2003), and other materials (Landry et al. 2006; Opoku et al. 2007). Simulation of direct shear test using PFC is considered as a promising approach to understand shear behaviors of a material. In PFC^{3D}, particle properties are described with some specific microproperties. These

microproperties affect the accuracy of the model outputs (Mishra and Murty 2001). PFC^{3D} models can be successful only if those microproperties are determined correctly.

The objectives of this study were

a) to measure shear properties (yield strength, internal friction, and cohesion) of hemp fiber and core;
b) to develop a model to simulate direct shear test of hemp fiber and core using PFC^{3D}, and calibrate and validate the model using experimental data.

3.4. MATERIALS AND METHODS

3.4.1. Shear Testing Apparatus

The shear testing apparatus (Wykeham Farrance, Inc., Slough, England) consisted of a shear box for containing material sample, a load cell to measure shear force, two sensors to measure horizontal and vertical displacement, and a data acquisition system (Fig. 3.1a). The shear box was formed by two cylindrical rings (Fig. 3.1b) had an inside diameter of 52 mm; the depth of 46 mm. Normal load was added to the material sample through dead weights.

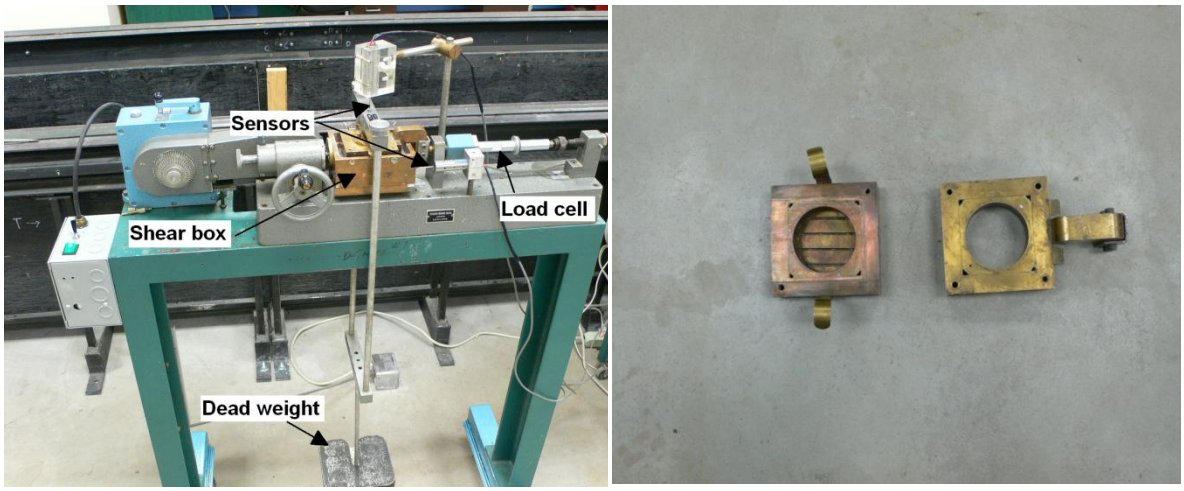

(a) (b)

Fig. 3.1. Direct shear testing apparatus; (a) experimental setup, (b) cylindrical rings.

3.4.2. Hemp Fiber and Core

The shear apparatus shown in Fig. 3.1 was used for direct shear tests of hemp material. The hemp material was from unretted hemp (variety: USO31) grown and processed in Manitoba, Canada. The material was a mixture of bast fiber and woody core. Before direct shear tests, fiber and core were separated manually and then ground to small particles (Fig. 3.2) using a coffee grinder. The average particle size was approximately 1.2 mm for fiber and 0.6 mm for core. Both materials were in air dry conditions. The moisture contents of the ground hemp fiber and core were 3.8% and 6.5% (dry basis), respectively, measured using the oven-dry method (ASABE 2003).

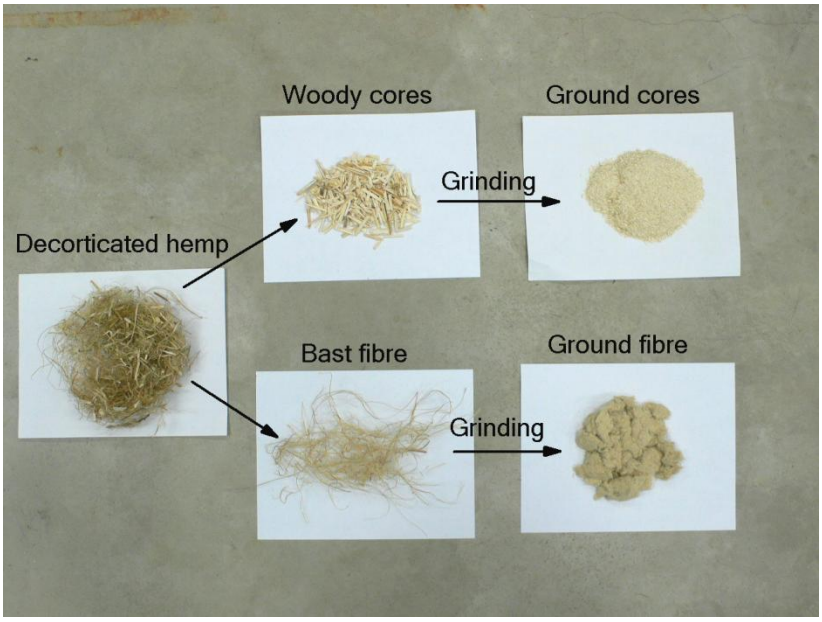

Fig. 3.2. Hemp materials and ground fiber and core used for direct shear tests.

3.4.3. Direct Shear Test

The Standard Test Method for Direct Shear Test of Soils under Consolidated Drained Conditions (ASTM 2007) was followed to conduct the tests, as no standards for direct shear test of hemp materials were available. Shear tests were performed under three normal forces of 94, 144, and 194 N, which were corresponding to normal stresses of 44.3, 67.8, and 91.3 kPa respectively, given the cross-section area of the shear box. The hemp sample was placed in the shear box and a predetermined normal load was applied. The sample in the shear box was consolidated under the normal force for 5 minutes to release the air within the shear box. Then, the lower ring of the shear box was laterally moved with respect to the upper ring at a constant speed of 0.2 mm/min according to ASTM (2007) for soil. During the shear test, the readings of shear force, lateral, and vertical displacements were recorded every second by the computer. Each test required approximately 48 minutes. Tests were performed for each of three normal loads for both

ground fiber and core. Internal friction and cohesion were derived from the regression line of the data of shear strength versus normal stress, as demonstrated in the Results and Discussion section.

3.5. SIMULATION OF DIRECT SHEAR TEST

3.5.1. Description of the PFC^{3D} Modeling Tool

The basic PFC^{3D} entity is spherical, named as "ball" which was used to define ground hemp fiber and core particles. Another basic entity in PFC^{3D}, “wall” was used to define the shear box. Figure 3.3 shows interactions between entities (ball to ball, and ball to wall). During interactions forces develop at the contacts. Contacts are created when two balls, or a ball and a wall, overlap; this corresponds to physical deformation of particles. Mechanical behavior of particles is predicted in terms of the movement of each particle and the inter-particle forces acting at each contact point. In a PFC^{3D} model, the relationship between particle motion and force causing motion is governed by Newton's law of motion, and several assumptions are made for particles and their interactions. For detail information, readers are referred to Cundall and Strack (1979).

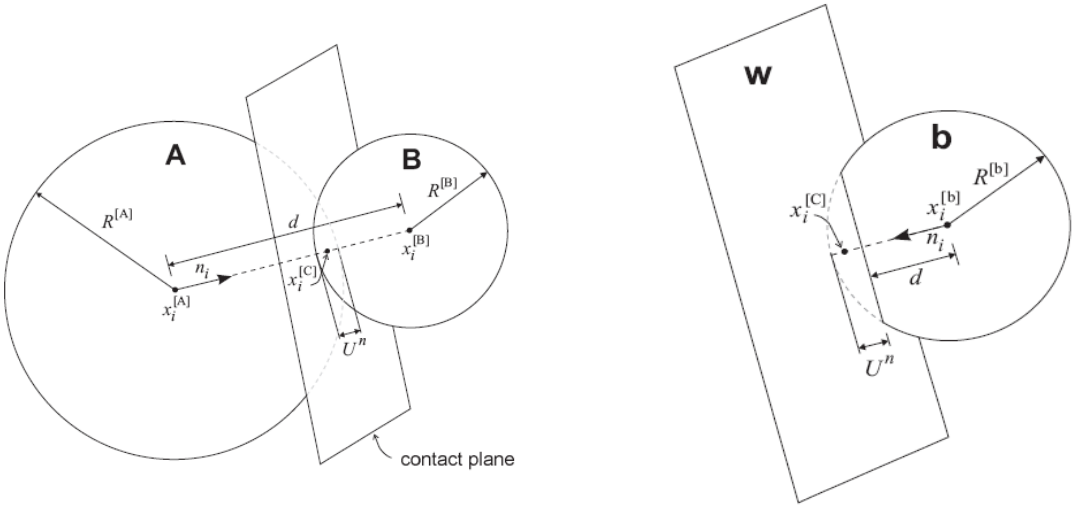

(a) (b)

Fig. 3.3. Contacts of entities in PFC^{3D} models: (a) ball-ball contact; (b) ball-wall contact. n_i = unit normal of the contact plane; U^n = overlap, relative contact displacement in the normal direction; $x_i^{[A]}$, $x_i^{[B]}$, and $x_i^{[b]}$ = the position vectors of the centers of Ball A, Ball B, and Ball b, respectively; $x_i^{[C]}$ = location of the contact point; d = the distance between the centers of entities; R = Radius of ball (Itasca 2008).

3.5.2. Development of A PFC^{3D} Model to Simulate Direct Shear Test

A PFC^{3D} model was developed to simulate direct shear tests. The model allowed virtual direct shear tests of hemp material to be performed in the same fashion as the real direct shear tests described above. Results of yield strength, cohesion, and friction from the virtual tests were compared with those from the real tests in the calibration and validation of the model.

3.5.2.1. Virtual direct shear apparatus

The virtual direct shear apparatus was constructed using the PFC^{3D} wall logic to represent the direct shear apparatus. Two cylindrical walls were placed one above another (Fig. 3.4). The top and bottom of the cylindrical walls were closed with a top flat wall and a bottom flat wall to confine particles. Wall surfaces were in contact with model particles during a virtual shear test. The friction of the top and bottom walls was selected as 1.0 and the cylindrical walls were considered frictionless (Franco et al. 2007).

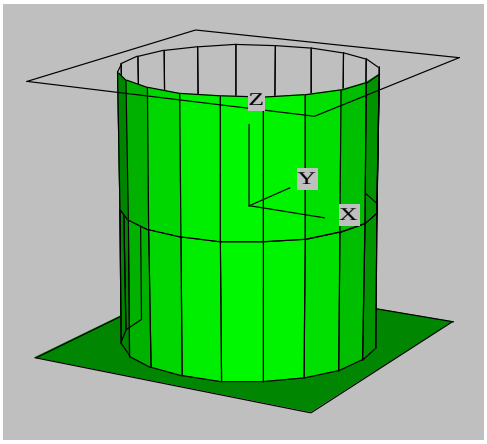

Fig. 3.4. Virtual direct shear apparatus with two cylindrical walls, a top flat wall, and a bottom flat wall.

3.5.2.2. Generating particle assembly

The particle assembly consisted of balls with a uniform diameter of 2 mm. This particle size was larger than the actual sizes of the ground fiber or core. Smaller ball sizes were not used due to the limited computing power of the computer. However, model particle size is not critical, if properties of model particles are calibrated with measurements (Momozu et al. 2003). Two-mm particles were generated into the virtual cylindrical walls

(Fig. 3.5) with a particle density of 1480 kg/m^3. This density value was reported by Lilholt and Lawther (2000) for hemp fiber. There was no existing value for core particle density and it was assumed the same as the particle density of fiber. After particle generation, the initial porosity of the particle assembly was adjusted to 30% for both fiber and core. This porosity was assumed to ensure a reasonably tight initial packing of the assembly (Potyondy and Cundall 2004). The porosity of the assembly was set by measuring the volume of all particles and the volume of the two cylindrical walls using a subroutine in the program.

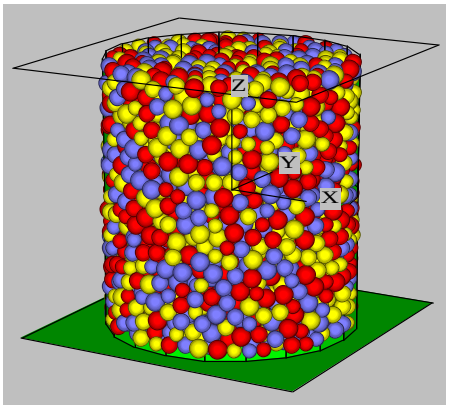

Fig. 3.5. Particle assembly in the virtual direct shear apparatus.

3.5.2.3. Virtual shear tests

Before the virtual shear tests, particles in the virtual direct shear apparatus underwent a number of calculation cycles (steps) to minimize the unbalanced forces acting over them. In each cycle, particles change their position due to the contact forces acting on the particles. Based on the force and displacement of a particle, the net force vector acting on the particle centroid is recalculated, and the particle changes its position again based on the force acting on it. The model is considered to be equilibrium when the maximum (or

average) unbalanced force is small compared to the maximum (or average) contact force in the model for a packed assembly of particles.

To simulate the constant normal loading process of direct shear test, the top flat wall was replaced with a circular servo control wall. The servo controlled wall controls the normal load by changing the wall velocity so that the force became equal to the required normal load. To simulate direct shear test, the bottom cylindrical wall was moved horizontally, as demonstrated in Fig. 3.6. The speed of the moving wall was the same as in the real test.

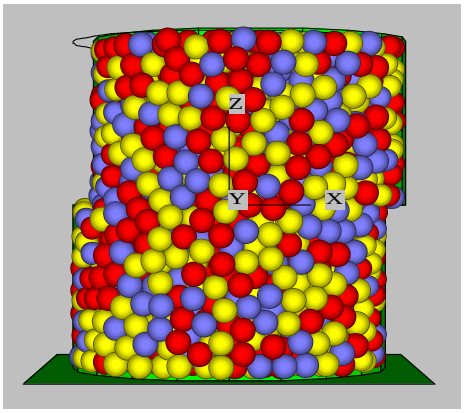

Fig. 3.6. Snapshot of virtual shear test.

3.5.3. Calibration of Ball Microproperties

The Linear Slip Model implemented in PFC^{3D} was selected to simulate the particle contacts. In the Linear Slip Model, contact forces and deflections between particles are governed by the stiffness and friction coefficient of the particles. The model microproperties for the Linear Slip Model included particle normal stiffness (k_n), shear stiffness (k_s), and friction coefficient (μ). As only one microproperty could be calibrated,

it was assumed that the particle shear stiffness, k_s, has the same value as the particle normal stiffness, k_n, (i.e. k_n/k_s=1). Other researchers (Asaf et al. 2007; McDowell and Harireche, 2002) have also assumed that k_n/k_s=1. Through preliminary simulations, it was found that the model outputs were more sensitive to k_n than to μ, meaning that k_n was more crucial. Thus, in calibrations, an initial value was assumed for μ first, while k_n was calibrated by trial and error method until the simulated shear stress matches the test result. Then the initial value of μ was checked with the calibrated k_n.

3.6. RESULTS AND DISCUSSION

3.6.1. Measured Shear Properties

3.6.1.1. Hemp fiber

Shear forces for different normal loads were plotted against the lateral displacement. For the ground fiber (Fig. 3.7a), apparent initial yield points could not be found under any of three normal loads. Thus, the force at a 15% of the lateral displacement relative to the diameter of the material sample was considered to be the yield force. This percentage selected was based on the studies from Chevanan et al. (2009) who reported that yield shear force was reached at a relative displacement of 10 to 20% for chopped biomass (switchgrass, wheat straw, and corn stover) tested in their direct shear experiments. ASTM (2007) also states that the yield point of soil is normally located at 10 to 20% relative lateral displacement. From Fig. 3.7a, the yield forces at 15% relative displacement (7.8 mm lateral displacement) were 91.50, 126.98 and 181.60 N for the normal loads of 44.3, 67.8, and 91.3 kPa respectively.

The yield forces were converted to yield stresses with the cross-section area of the shear surface of the sample. They were then plotted with the normal loads (Fig. 3.7b), and a linear trend line with the coefficient of determination (R^2) of 0.98 was obtained. According to the regression equation of the linear line, the cohesion of the ground fiber was 1.59 kPa (the intersection of the trend line) and the internal friction coefficient was 0.90 (the slope of the line). These measured values for hemp fiber were comparable with those for other biomaterials reported in the literature. The internal friction coefficient of hemp fiber was slightly higher than the range of friction coefficients (0.46 - 0.71) measured for wheat flour by Duffy and Puri (1999) and that (0.37 - 0.82) measured by Opoku et al. (2007) for flax fiber, but within the range (0.57-1.04) measured by Chevanan et al. (2009) for three types of biomass. The cohesion of the fiber obtained from this study was slightly higher than the range (0.31-1.17 kPa) measured by Chevanan et al. (2009) for biomass, but within the range (0.52 and 2.21 kPa) measured by Duffy and Puri (1999) for wheat flour.

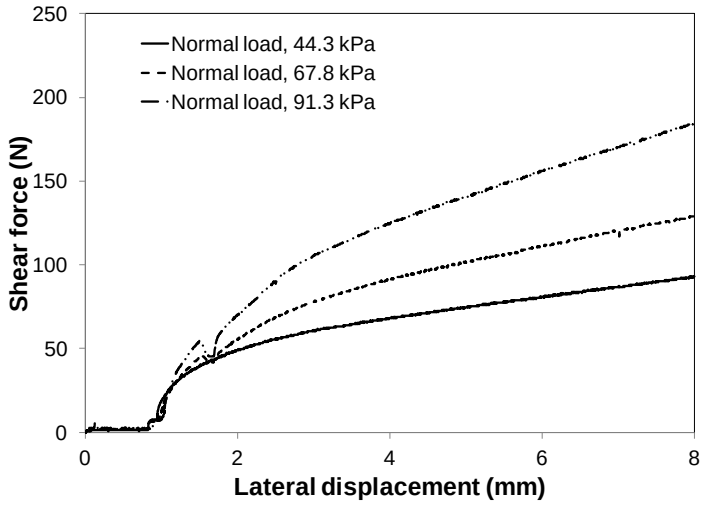

(a)

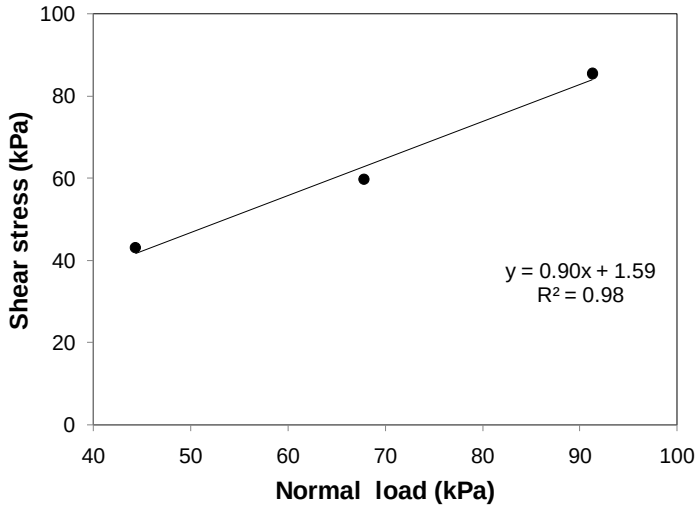

(b)

Fig. 3.7. Direct shear test results for ground fiber: (a) shear force-displacement curve; (b) yield stress versus normal load.

3.6.1.2. Hemp core

The force-displacement curves for core did not show any yield points either (Fig. 3.8a). Yield forces for core were also read from the force-displacement curves at 15% relative

displacement, and they were 98.59, 143.28, and 207.14 N for the normal loads of 44.3, 67.8, and 91.3 kPa, respectively. These yield forces were greater than those of the ground fiber, indicating that core had higher shear strength. Through the linear regression of the normal loads and the yield stresses, it was found that the cohesion of the ground core was zero and the internal friction coefficient was 1.04 (Fig. 3.8b). The cohesionless behavior may be attributable to the dry and smooth surface of the core particles. When compared to the literature data mentioned above for other biomaterials, the cohesion measured in this study for hemp core was low, and the friction coefficient was at the higher end.

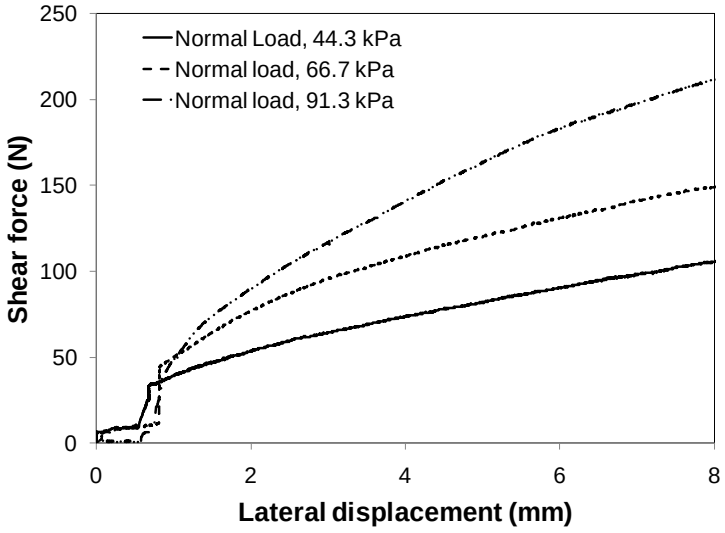

(a)

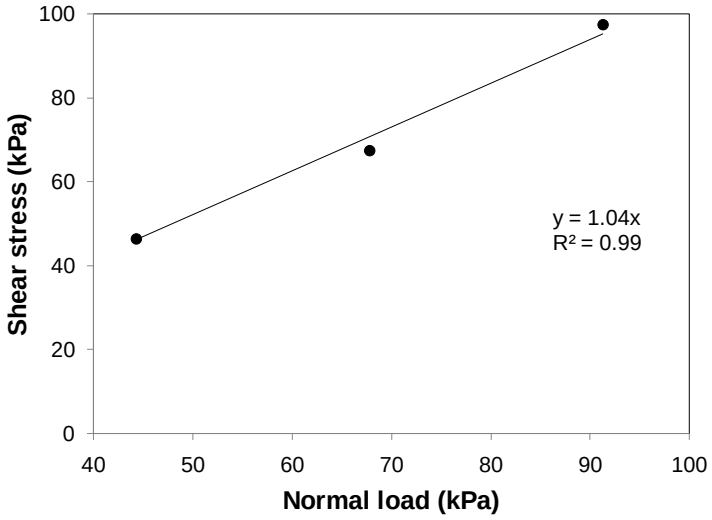

(b)

Fig. 3.8. Direct shear test results for ground hemp core: (a) shear force-displacement curves; (b) yield stress versus normal load.

3.6.2. Calibrated Microproperties

Commonly used values of particle friction coefficient are between 0 and 1.0; for example $\mu = 0.3$ in Djordjevic (2003); $\mu = 0.4$ in Yang et al. (2006); $\mu = 0.7$ in Yan and Ji (2010) and Mishra and Murty (2001). From preliminary simulations using the PFC^{3D} model, it was found that higher μ values gave force-displacement curves closer to the measured ones over all normal loads, regardless of the particle stiffness. Thus, an initial value of 1.0 was chosen for the subsequent calibration of k_n for both fiber and core. Using this initial μ value, virtual direct shear tests were performed using the model. The simulated shear force-displacement curve was obtained under each of the three normal loads. Figure 3.9 shows a typical simulated curve. The first part of the curve had a rapid increasing trend in shear force as the material is being sheared, then force started fluctuating. Fluctuating outputs have been also observed in DEM simulations by other researchers (Shmulevich et al. 2009).

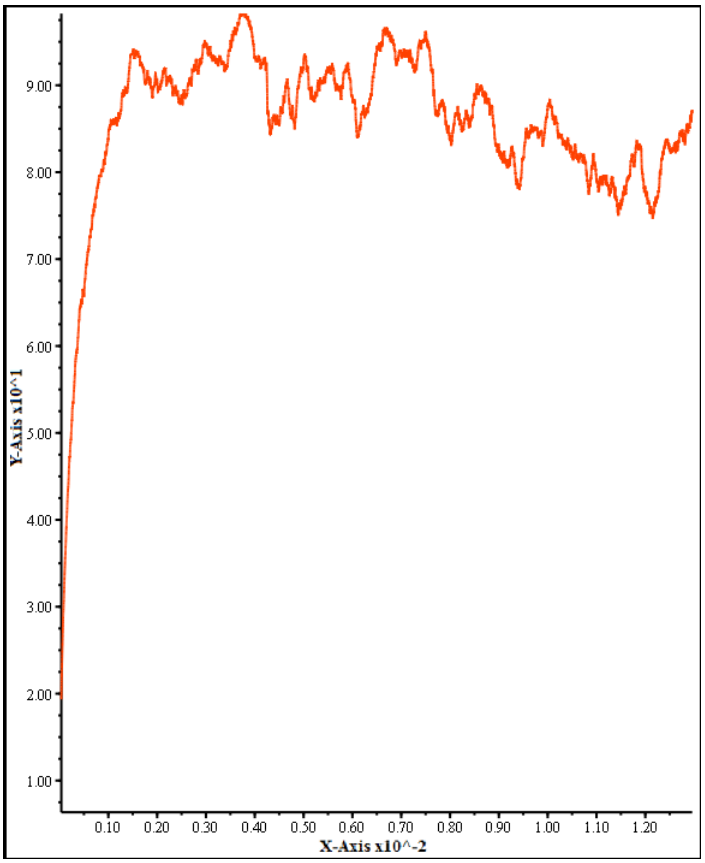

Fig. 3.9. A typical simulated shear force versus lateral displacement for fiber (normal load: 44.3 kPa); X-axis: displacement in m and Y-axis: shear force in N.

The simulated stresses at the yield points were read at the peak point of the shear force and displacement curve and compared with the measured yield stresses. The results showed that the k_n which resulted in the best match between the measurements and the simulations over all three normal loads was 5e4 N/m for fiber and 8e4 N/m for core. With these calibrated k_n values, the model was rerun to check if the assumed initial value, 1.0 for μ was appropriate. Results with three arbitrarily selected values of μ showed that the simulated yield stress increases with the increase of μ (Fig. 3.10) and that μ=1.0

resulted in a simulated yield stress which is the closest to the measured yield stress. This confirmed that the selected initial value 1.0 of μ was appropriate.

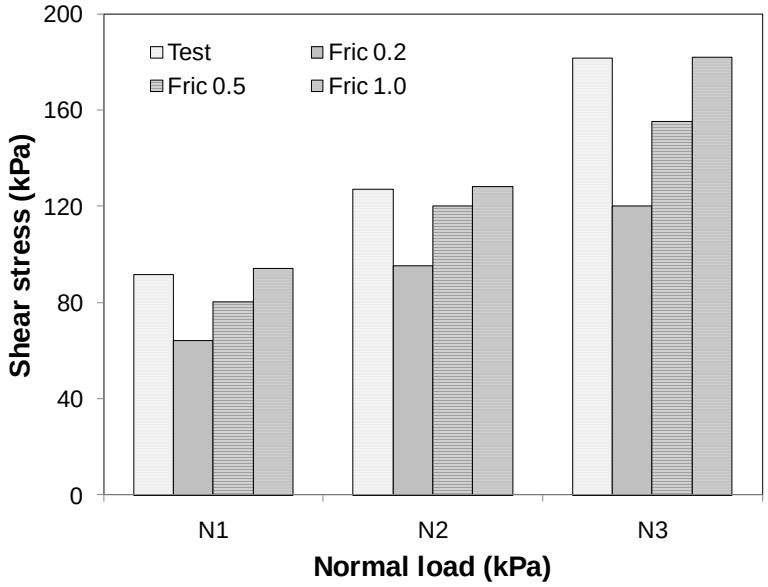

Fig. 3.10. Simulated shear stresses at yield points versus normal loads for different particle friction coefficients.

3.6.3. Model Validation

To validate the model, simulations were performed using normal loads which were different with those used in the measurements. This was based on the fact that internal friction coefficient and cohesion of a material are independent of the normal loads applied in direct shear tests. If the model particles represented for the real hemp material particles, the friction coefficient and cohesion simulated and measured should match each other, regardless of the normal loads. The model was run with normal loads: 50, 70, 80 and 99 kPa, and the calibrated μ, k_n and k_s. The resultant yield stresses were plotted to

generate internal friction coefficient and cohesion. The simulated yield stresses were highly linear as those from tests, as demonstrated by the high R^2 values: 0.98 for hemp fiber (Fig. 3.11a) and 0.99 for core (Fig. 3.11b). Simulated values of cohesion and internal friction coefficient were obtained from the linear regression equations. Comparisons between simulated and measured shear properties were made using relative errors. Results are summarized in Table 3.1. The relative errors between simulations and measurements were lower than 10%, except for the cohesion of fiber where the relative error was high, and the reasons were unknown.

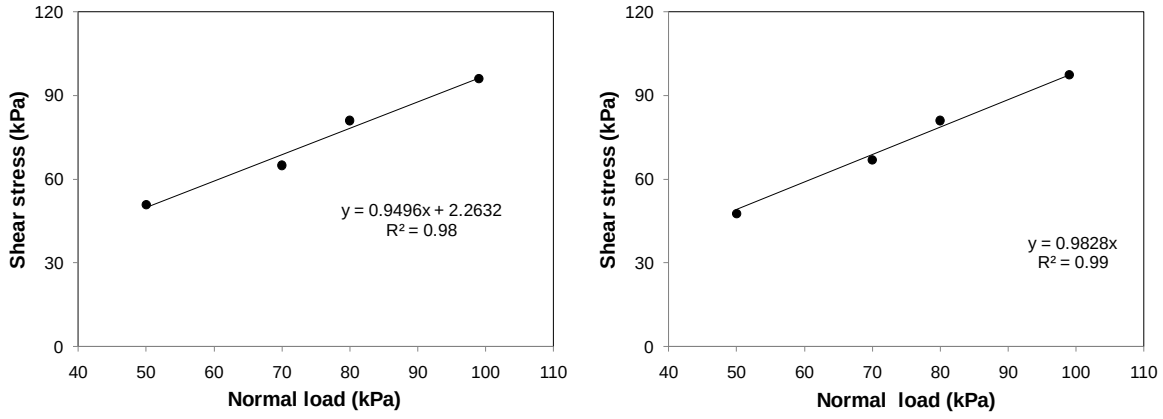

(a) (b)

Fig. 3.11. Simulated shear strengths versus normal loads: (a) hemp fiber; (b) hemp core.

Table 3.1. Comparisons of shear properties between measurements and simulations

Material	Shear property	Measurement	Simulation	Relative error (%)
Ground hemp fiber	Cohesion (kPa)	1.59	2.26	42.14
	Internal friction coefficient	0.90	0.94	4.10
Ground hemp core	Cohesion (kPa)	0.00	0.00	0.00
	Internal friction coefficient	1.04	0.98	5.77

3.7. CONCLUSION

The range of the yield forces for ground hemp fiber was between 91.50 and 181.60 N and that for ground hemp core was 98.59 to 207.14 N, under the given normal loads. The cohesion and internal friction coefficient of ground hemp fiber were 1.59 kPa and 0.90 respectively. Lower cohesion and greater friction were observed for ground hemp core, and the corresponding values were zero and 1.04. The model developed using the PFC^{3D} Linear Slip Model for particle contact can be used to simulate direct shear tests of hemp fiber and core. With a particle friction coefficient of 1.0 and under an assumption of the model particle shear stiffness being equal to the normal stiffness, the model particle normal stiffness was calibrated using the measurements, and it was 5e4 N/m for ground fiber and 8e4 N/m for ground core. When compared the model results of shear properties with the measurements, the model agreed well with the measurements, except for the result of the cohesion of hemp fiber.

It should be noted that the microproperties were calibrated based on a uniform particle size (particle diameter: 2 mm) for both fiber and core particles. The calibration results may vary when different particle sizes are chosen. Also, the results were obtained from a

given hemp variety under a given moisture condition (air dried). Caution should be taken when using the results for different hemp varieties under different conditions.

3.8. ACKNOWLEDGEMENTS

This work was supported by the Natural Sciences and Engineering Research Council of Canada (NSERC). The authors would also like to thank Fangliang Chen for conducting direct shear tests and Dr. Sacha Emam, Itasca Consulting Group, Inc for his guidance during model development. Thanks are also given to Composites Innovation Centre Manitoba Inc., Emerson Hemp Distribution Company, and Parkland Industrial Hemp Growers Co-op Ltd for their support to the project.

3.9. REFERENCES

Afzalinia, S., and M. Roberge. 2007. Physical and mechanical properties of selected forage materials. *Canadian Biosystems Engineering* 49(2): 23-27.

ASABE Standards. 2003. S358.2: Moisture measurement-Forages. St. Joseph, Mich.: ASAE.

Asaf, Z., D. Rubinstein, and I. Shmulevich. 2007. Determination of discrete element model parameters required for soil tillage. *Soil and Tillage Research* 92(2): 227-242.

ASTM. 2007. Annual Book of ASTM Standards. Vol. 4.08 D3080-04. Standard test method for direct shear test of soils under consolidated drained conditions. West Conshohocken, PA.: American Society for Testing and Materials.

Chevanan N, A. R. Womac, V. S. P. Bitra, D. C. Yoder, and S. Sokhansanj. 2009. Flowability parameters for chopped switchgrass, wheat straw and corn stover. *Powder Technology* 193: 79–86.

Cundall, P. A. 1988. Computer simulations of dense sphere assemblies. In *Micromechanics of Granular Materials,* 113-123. M. Satake, and J. T. Jenkins, eds. Wageningen, The Netherlands: Elsevier Science.

Cundall, P. A., and O. D. L. Strack. 1979. A discrete numerical model for granular assemblies. *Geotechnique* 29: 47-65.

Djordjevic, N. 2003. Discrete element modeling of the influence of lifters on power draw of tumbling mills. *Minerals Engineering* 16: 331-336.

Duffy, S. P., and V. M. Puri. 1999. Evaluation of the computer controlled dynamic yield locus tester. *Powder Technology* 101: 257-265.

Franco, Y., D. Rubinstein, and I. Shmulevich. 2007. Prediction of soil-bulldozer blade interaction using discrete element method. *Transaction of ASABE* 50(2): 345-353.

Itasca. 2008. Theory and Background. PFC^{3D} (Particle flow code in three Dimensions), version 4.0 Minneapolis, MN.: Itasca Consulting Group, Inc.

Landry, H., F. Thirion, C. Laguë, and M. Roberge. 2006. Numerical modeling of the flow of organic fertilizers in land application equipment. *Computers and Electronics in Agriculture* 51: 35-53.

Lilholt, H., and J. M. Lawther. 2000. Fiber reinforcements and general theory of comprehensive composite materials. In *Comprehensive Composite Materials,* 1: 303-325. Kelly, A., and C. Zweben, eds. Wageningen, The Netherlands: Elsevier Science.

McDowell, G. R., and O. Harireche. 2002. Discrete element modeling of yielding and normal compression of sand. *Géotechnique* 52(4): 299-304.

Mishra, B. K., and C. V. R. Murty. 2001. On the determination of contact parameters for realistic DEM simulations of ball mills. *Powder Technology* 115(3): 290-297.

Momozu, M., A. Oida, M. Yamazaki, and A. J. Koolen. 2003. Simulation of a soil loosening process by means of the modified distinct element method. *Journal of Terramechanics* 39: 207-220.

Ni, Q., W. Powrie, X. Zhang, and R. Harkness. 2000**.** Effect of particle properties on soil behaviour: 3-D numerical modelling of shearbox tests. *Geotechnical Special Publication* 96: 58-70.

Opoku, A., S. Panigrahi, and L. G. Tabil. 2007. Frictional properties of natural and chemically treated flax fiber. ASABE Paper No. 076188. St-Joseph, MI: ASABE.

Potyondy, D. O. 2007. Simulating stress corrosion with a bonded-particle model for rock. *International Journal of Rock Mechanics and Mining Science* 44: 677-691.

Potyondy, D. O., and P. A. Cundall. 2004. A bonded-particle model for rock. *International Journal of Rock Mechanics and Mining Science* 41(8): 1329-1364.

Shmulevich, I., Rubinstein, D., and Asaf. Z., 2009. Discrete Element Modeling of Soil-Machine Interactions, in Advances in Soil Dynamics, Volume 3, Chapter 5, pp. 399-433 St. Joseph, MI: ASABE.

Yan, Y., and S. Ji. 2010. Discrete element modeling of direct shear tests for a granular material. *International Journal of Numerical and Analytical Methods in geomechanics* 34: 978-990.

Yang, B., Y. Jiao, and S. Lei. 2006. A study on the effect of microparameters on macroproperties for specimens created by bonded particles. *Engineering Computations: International Journal of Computer Aided Enggineering and Software* 23(6): 607-631.

Chapter 4

Simulation of Tensile Tests of Hemp Fibre using Discrete Element Method (DEM)

4.1. SIGNIFICANCE

In the previous chapter only the ball microproperties were determined. Calibrating bond microperoperties would be the next step of the simulation process. As a continuation of the work this chapter focused on determining more hemp properties. Experiments were carried out to determine the tensile properties of the hemp fibre. The experiment results were used to calibrate the bond microproperties of hemp fibre through virtual tensile test using PFC^{3D}. This chapter corresponds to the objective 2 of the thesis.

4.2. ABSTRACT

Tensile strength is an important property of hemp fibre, because it plays an important role in determining the mechanical strength of fibre-based products such as biocomposites. A commercial discrete element software, Particle Flow Code in Three Dimensions (PFC^{3D}), was used to develop a numerical model which simulates tensile tests of hemp fibre. The model was able to simulate tensile tests and predict the tensile properties (such as strength and elongation) of a hemp fibre. In the model, a virtual hemp fibre was defined as a string of spherical balls (the basic PFC^{3D} particles), held together by cylindrical bonds implemented in PFC^{3D}. To calibrate the model, tensile data was collected for both unretted and retted hemp fibres using a commercial Instron testing system. The average

fibre diameter was 0.34 mm for the unretted fibres and 0.30 mm for the retted fibres. The average tensile strength measured was 358 MPa for the unretted fibres and 343 MPa for the retted fibre. The corresponding average elongations for the two types of fibres were 0.88 and 0.80 mm, for an original fibre length of 25 mm. The bond stiffness, the most sensitive microproperty of the model was calibrated. The calibrated value was $1x10^{14}$ Pa m^{-1} for both the retted and unretted fibres. The model was validated with literature data. The validation results showed that the simulated elongation reasonably well correlated to the literature data with a relative error of 17.5%.

4.3. INTRODUCTION

Hemp fibre is the outer layer of the hemp stem, also called bast fibre (Garcia et al. 1998; Mediavilla et al. 2001). Hemp fibres extracted through mechanical processing are bundles (Fig. 4.1). Each fibre bundle consists of many single fibres. This study did not deal with single fibres, but with fibre bundle (referred to as fibre hereafter for simplicity). Hemp fibre is a valuable source for making environmentally friendly and biodegradable products. Also, hemp fibre has very high tensile strength ranged between 0.49 to 1 GPa (Williams and Wool 2000; Munder and Fürll 2004; Beckermann and Pickering 2008). As a result, hemp fibre has been used in textile applications for a long time. Lately, hemp fibre has been used in many other industrial products such as biocomposites for automobile industries. Development of any hemp fibre products requires the knowledge of physical and mechanical properties of hemp fibre.

Fig. 4.1. A hemp fibre bundle.

Tensile strength is one of the important fibre properties because of its extensive use in evaluating the strength of fibre products (Bledzki et al. 1996). The tensile properties of hemp fibres may be affected by chemical treatment (Beckermann and Pickering 2008) and retting of the hemp (Munder and Fürll 2004). Retting is a biological process by which pectin and hemicellulosic compounds between the individual fibre cells are degraded. The main reason for retting hemp is to reduce the effort of mechanical extraction of fibre. Although fibre properties have been measured by several researchers (e.g. Rowell et al. 2000; Hobson et al. 2001; Munder and Fürll 2004), little work has been done to numerically simulate fibre properties.

This study used the discrete element method (DEM) to simulate tensile test of a hemp fibre to determine the tensile properties of the fibre. The DEM is a numerical method to model a material as an assemblage of discrete particles. The DEM was first introduced by Cundall and Strack (1979) for analyzing geological materials (rocks and soils). Since then, the DEM has become a promising tool to simulate mechanical behaviours of various other materials, including fibre (Sadek et al. 2011). However, no simulations have been carried out on tensile tests of fibre using the DEM.

One commercial DEM software is Particle Flow Code in Three Dimensions (PFC^{3D}) (Itasca Consulting Group, Inc., Minneapolis, MN). In PFC^{3D}, the basic particles are spherical and they are referred to as balls. Materials to be simulated are represented by assemblies of individual balls. A group of balls can be arranged together to simulate any arbitrary shape of particle assembly. PFC^{3D} provides users with different contact models among particles, which allows to model different particle interaction behaviours, for example, free-flowing granular material, such as powder (Djordjevic 2003) and grains (Lu et al. 1997; Sakaguchi et al. 2001), cohesive and frictional materials, such as soil (Ni et al. 2000; van der Linde 2007; Mak et al. 2011) and manure (Landry et al. 2006) and solid materials, such as rock (Potyondy and Cundall 2004; Pierce 2004). PFC^{3D} is considered as a potential tool for the simulation of hemp fibres.

Regardless of the type of material to be simulated, a set of microproperties is required as input parameters for any PFC^{3D} models. Microproperties define a model at the particle level, and they significantly affect the model outputs. Most microproperties are not measurable at the current time, and they are determined either using analytical assumption or inverse calibration methods. In analytical assumption methods, microproperties are determined using existing theory of the material. For example, Young modulus and Poisson's ratio of bulk material were used to determine particle normal and shear stiffness of the material (Cundall and Strack 1982; Walton 1987; Rothenburg and Bathurst 1989; Chang et al. 2003). In inverse calibration methods, microproperties are determined by matching the simulated results with experimental data. For example, direct shear tests were used to calibrate model microproperties of a material

through matching simulated friction angles with measured data (Franco et al. 2007; Coetzee and Els, 2009; Sadek et al. 2011a; Sadek et al. 2011b). Similarly, Tanaka et al. (2000) and Asaf et al. (2007) used penetration test data for calibrating a soil model, and Vu-Quoc et al. (2000) used drop weight test data for calibrating a model for soybean grains.

In summary, understanding the properties of hemp fibre is important to industries which use hemp fibre for their products. To date, no discrete element models have been developed for simulations of fibre tensile properties. The objectives of this study were to

a) develop a discrete element model to simulate the tensile properties of hemp fibre using PFC^{3D},
b) measure tensile properties of hemp fibres, and
c) calibrate the model using the measurements and validate the model using the literature data.

4.4. THE TENSILE TEST OF HEMP FIBRE

Laboratory tests were first carried out in this study for a better understanding of hemp fibre properties. Results from the tests were also used to support model development and calibration.

4.4.1. Experimental Methods

4.4.1.1. The tensile test frame

The Instron electromechanical testing system (3366, Instron Corporation, MA, USA) was used for fibre tensile tests. The testing system (Fig. 4.2) consisted of a frame, a crosshead, two clamps, a load cell, a drive system, and a controller. The bottom clamp was stationary and affixed to the base of the frame, and the top clamp was connected to the crosshead through the load cell (2 kN capacity). The test sample was secured using the clamps. As the drive system moved the crosshead up, it applied a tensile load on the sample. The system was controlled via an Instron proprietary software (Bluehill2) which allowed users to set the test parameters and analyze the data.

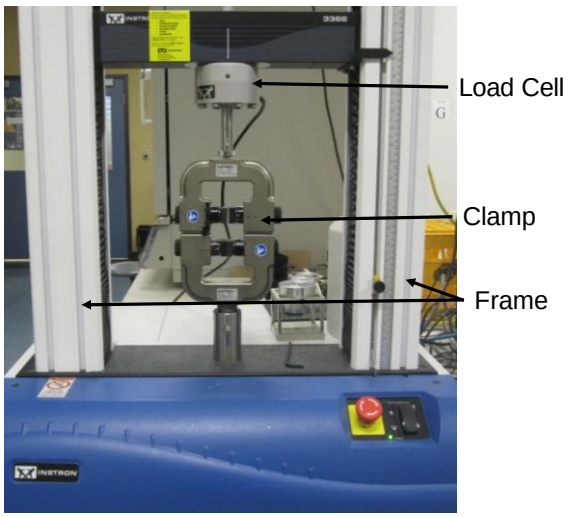

Fig. 4.2. The Instron testing system and its components.

4.4.1.2. Fibre sample preparation

Hemp fibre samples used for tensile tests were from two types of fibre: unretted and retted hemps. The unretted hemp was baled shortly after being swathed and the retted hemp was left to ret in the field for approximately six weeks prior to being baled. To obtain fibres, hemp was mechanically processed as shown in Figs 4.3a and 4.3b. Fibre samples for tensile tests were picked up from those processed material. To obtain representative fibre samples, each of the retted and unretted hemp materials was divided into six arbitrary groups and each group was assigned a number of one to six. A random number generator was used to generate an array of 30 random numbers between one and six. Selecting fibres was done by picking one fibre from each group at a time, and at the end, 30 retted and 30 unretted samples were selected for tensile tests. Selected fibres were cut to a length of approximately 45 mm, and they were assigned an identification number from 1 to 30 (Fig. 4.3c) for the purpose of randomising the tests.

(a) (b) (c)

Fig. 4.3. Hemp materials; (a) processed unretted hemp, (b) processed retted hemp, (c) hemp fibre samples prepared for tensile tests.

4.4.1.3. Sample conditioning

The humidity of the environment where the measurements are taken has a significant effect on the strength and strain of textile materials (Saville 1999). The National Standard of Canada on Textile Test Methods defines the standard atmosphere as air maintained at a relative humidity of 65% and a temperature of 21 ºC (CGSB 2001). Therefore, before tensile tests, all fibre samples were exposed to this standard atmosphere in an environmental chamber for a period of three days to bring the samples to moisture equilibrium with the standard atmosphere.

4.4.1.4. Tensile tests

Prior to the test, each fibre sample was attached to a thin cardboard frame (Fig. 4.4a) to avoid slippage from the clamps of the testing system during pulling. The sample was secured inside the cardboard window using polyepoxide (Epoxy) glue. The window gave an effective testing fibre length of 25 mm. To start testing, the cardboard frame was fitted into the grips. Then, the sides of the cardboard frame were cut so that only the fibre was

pulled during the test. Tension was applied to the fibre by moving the crosshead up and continued until the sample broke as shown in Fig. 4.4b.

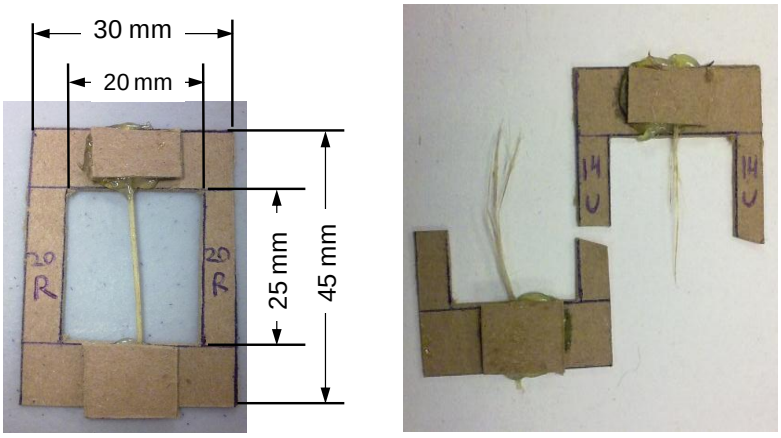

(a) (b)

Fig. 4.4. Tensile testing samples: (a) a fibre sample on a cardboard frame before test, (b) a broken fibre sample after test.

4.4.2. Measurements

4.4.2.1. Fineness and diameter of fibre

Fibre fineness corresponds to the linear mass density of fibre. The unit of fibre fineness is expressed as tex which is equal to a mass of 1 gram per kilometer of fibre length (Kymäläinen 2004). The mass of the fibres was measured using a high-precision analytical scale (Symmetry PA 220, QC, Canada), and the length was measured using a ruler. The mass and the length were used to determine the fineness. Then, fibre diameter was estimated using the following equation, assuming that fibre had a circular cross-section (Munder and Fürll 2004).

$$d = \sqrt{\frac{4f}{\pi\rho}} \quad (4.1)$$

where

d = fibre diameter (μm),

f = fibre fineness (tex),

ρ = fibre particle density (kg m^{-3}).

The particle density of hemp fibre was taken as 1,480 kg m^{-3}. This density value was reported by Lilholt and Lawther (2000).

4.4.2.2. Tensile strength

The Bluehill2 software of the Instron testing system recorded the load-extension curve during a test. The sensitivity of the software was adjusted to determine the maximum load at 10% after drop in maximum force. Consequently, the software detected the maximum load at the fibre failure. The fibre strength can be also described in stress format. The maximum stress was the maximum tensile force divided by the cross-section area.

4.4.2.3. Specific stress

The measurement of specific stress provides the means of comparing individual fibres in equivalent terms and methodology. The specific stress was the maximum tensile force divided by the fineness of the fibre (Khan et al. 2011).

4.4.2.4. Maximum strain and elongation

The maximum strain was the relative change in length of the sample at the maximum tensile force, recorded by the Bluehill2 software. The elongation at the fibre failure was determined from the maximum strain, given the initial fibre length of 25 mm.

4.4.2.5. Modulus of elasticity

The criteria for measuring the modulus of elasticity was implemented by an algorithm built within the Bluehill2 software. The software used a least square fit algorithm in determining the modulus of elasticity from the load-extension curve. The modulus of elasticity in this study was expressed in the same units as the specific stress.

4.4.2.6. Work of rupture

To determine the work of rupture, the Bluehill2 software measured the amount of energy required to reach the yield point; this energy was calculated by determination of the area under the load-extension curve before the yield point. The yield point is the point where the slope of the load-extension curve is zero.

4.4.3. Data Processing

Each fibre sample was examined after the test to see if the data should be kept or discarded. The majority of the fibre samples broke along the intermediate section of the length within the cardboard window as shown in Fig. 4.4b. In such cases, the data were kept. In instances where the glue was not able to maintain the sample attached to the cardboard frame, the data were discarded. Out of 30 samples, the data considered valid

included 21 samples for the unretted fibres and nine samples only for the retted samples. It is important to note that the main objective of the tensile tests in this study was to support model development. Therefore, in spite of the limited number of fibre samples, the data was deemed sufficient for the purpose of model calibration. Student's t-tests were used to examine differences in those measured variables between the retted and unretted fibres at the probability of 0.05.

4.4.4. Results from the Laboratory Tests

4.4.4.1. Load-extension curve

Load-extension curves from the tensile tests could be classified into three types of curves. One type was that as the fibre was extended, the load increased in a linear fashion; at a certain point of extension, the load reached its peak, and the fibre sample suddenly broke and the load dropped to zero (Fig. 4.5a). This behaviour of hemp fibre is similar to that of a brittle material. For the particular fibre shown in Fig. 4.5a, the maximum load and the elongation of the fibre were 30 N and 0.65 mm, respectively. Another type of curve also showed the brittle behaviour; however, the increasing load portion of the curve was not linear, but polynomial (Fig. 4.5b). The third type of curve had the similar increasing portion (in either linear or polynomial fashion), but a gradual failure pattern (Fig. 4.5c). In the last case, the fibre must split into multiple thinner fibres which broke at different times during testing, and the incompletely broken fibre could still carry some load until being completely broken.

For the unretted fibres, the majority (approximately 80%) of the samples behaved like either Fig. 4.5a or Fig. 4.5b, and the other 20% behaved more like Fig. 4.5c. For the retted fibres, approximately 50% experienced a form of behaviour like Fig. 4.5a, and the other 50% behaved like Fig. 4.5c. One may say that the unretted fibres were more brittle than the retted fibres. However, this would need to be further verified with a larger number of samples.

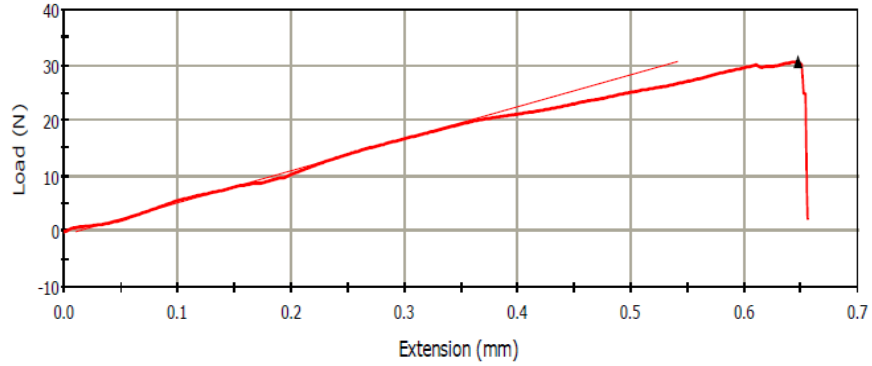

(a)

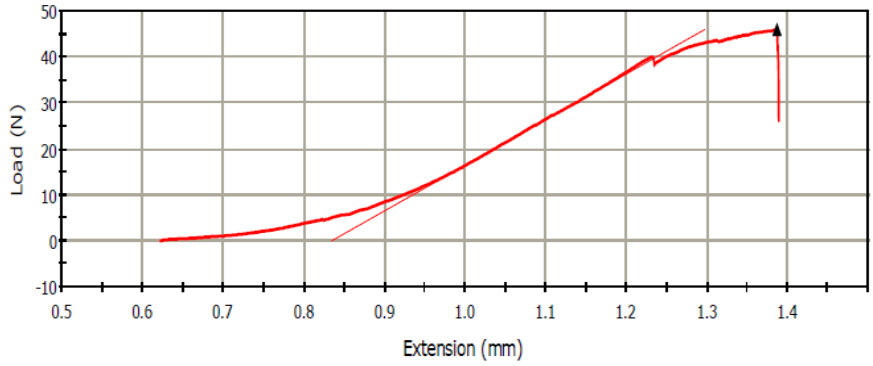

(b)

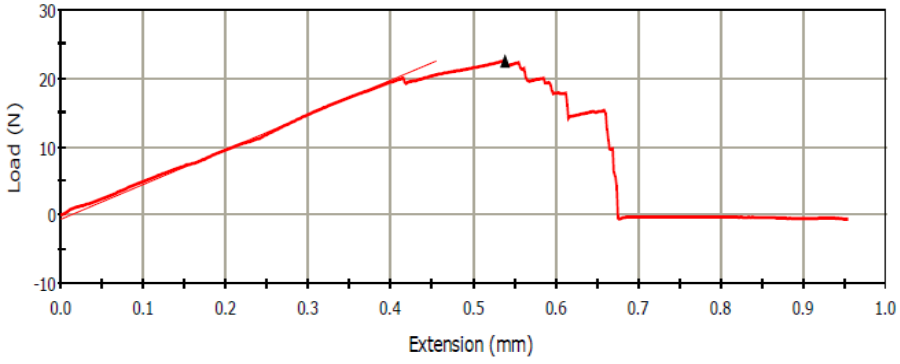

(c)

Fig. 4.5. Typical results of load-extension curves from the tensile tests: (a) linear curve and sudden failure, (b) polynomial curve and sudden failure, (c) gradual failure; the triangle sign on the figure stands for the point where the maximum load and strain were taken.

4.4.4.2. Fibre properties

The results of statistical analysis showed that none of the measured variables were significantly different between the retted and unretted fibres at the probability of 0.05. This was due to the highly variable nature of fibre properties. However, the data showed some important trends of the effects of retting conditions on fibre properties.

The retted fibre had approximately 23% lower fineness and 35% lower standard deviation than the unretted fibre (Table 4.1). This indicated that retting hemp could improve the fineness and the uniformity of fineness. Accordingly, the diameters of the retted fibre were smaller and less variable than those of the unretted fibre. On average, the retted hemp fibre carried 22% lower loads than the unretted fibre, the corresponding maximum loads were 24.5 and 31.6 N respectively. As the retted fibre had smaller diameter and lower fineness, only 4% lower maximum stress and 8% lower specific stress were observed for the retted fibre. Similar strength was reported by Khan et al. (2011) for unretted fibre which was comparable with the range of the specific stress observed in this study. Munder and Fürll (2004) found that the maximum tensile stresses of hemp fibre varied from 0.5 to 0.9 GPa. Slightly lower maximum tensile stresses were observed in this study.

The maximum strain and elongation of the retted fibre were also slightly lower, when compared to those of the unretted fibre. As a result of their lower loads and strains, the retted fibre had lower work of rupture and higher modulus. Sankari (2000) studied the properties of 14 varieties of hemp fibre and reported higher specific stresses ranging from

41 to 74 cN tex^{-1}, but the reported maximum strains (3.3 to 5.0%) were similar to this study. Higher specific stresses were also reported by Hobson et al. (2001) for retted and unretted hemp fibre. Schäfer and Honermeier (2006) also reported higher specific stress of hemp fibre.

Table 4.1. Summary of measured properties of the unretted and retted fibres

Property	Unretted fibre		Retted fibre	
	Mean	SD*	Mean	SD*
Fineness, tex	139	59.6	107	39.0
Diameter, mm	0.34	0.071	0.30	0.057
Maximum load, N	31.6	15.6	24.5	15.9
Maximum stress, MPa	358	173	343	157
Specific stress, cN tex^{-1}	24.2	11.7	23.2	10.6
Maximum strain, %	3.55	1.78	3.20	2.34
Elongation, mm	0.88	0.44	0.80	0.58
Work of rupture, mJ	17.1	14.4	12.9	14.6
Modulus, cN tex^{-1}	1136	651	1397	603

*SD is Standard deviation.

4.5. SIMULATION OF THE TENSILE TEST

4.5.1. Model Development

4.5.1.1. Construction of virtual fibre

For simulations of tensile tests, a virtual fibre was first constructed with a set of PFC^{3D} basic particles (balls). This was done using the cluster logic of PFC^{3D}. A PFC^{3D} cluster

consists of a series of balls. Balls can be arranged to construct a cluster with any desired shape. For the virtual fibre, balls in the cluster were arranged like a string and all the balls had the same diameter (Fig. 4.6a). The ball diameter and number of balls can be varied to match the diameter and length of the fibre to be simulated. The number of balls required for a fibre with a given length and a given diameter is calculated by the following equation:

$$n = \frac{l}{D} + 1 \tag{4.2}$$

where

n = number of balls in virtual fibre,

D = diameter of balls, equal to the diameter of fibre (mm),

l = length of virtual fibre (mm).

The next step was to define the contact between balls in the virtual fibre, so that the virtual fibre could withstand tensile load like a real fibre. The different contact models implemented in PFC^{3D} include stiffness model, slip model, and bond models. In the stiffness or slip models, the contact force and relative movement between balls are governed by the stiffness or friction of the balls. These contacts are more appropriate for describing free flowing granular materials such as grain and sand particles. The bond models are more suitable for fibres, because the bond at the contact between balls provides certain inter-particle tensile capacity. PFC^{3D} provides two types of contact bond: point and cylindrical bonds. The cylindrical bond model, named as parallel bond model

(PBM), is more suitable for modelling hemp fibre, as it provides higher tensile strength between balls.

Examples of virtual fibres with the PBM are shown in Fig. 4.6b. Bonds act over a circular cross section at the contact point of two balls. The cylindrical bond withstands tensile load and the bond breaks if the maximum external load exceeds the prescribed strength of the bond (Potyondy and Cundall 2004). Breaking of any bonds in a virtual fibre means the failure of the virtual fibre. Therefore, the strength of the virtual fibre is determined by the properties of the bond to be specified by users.

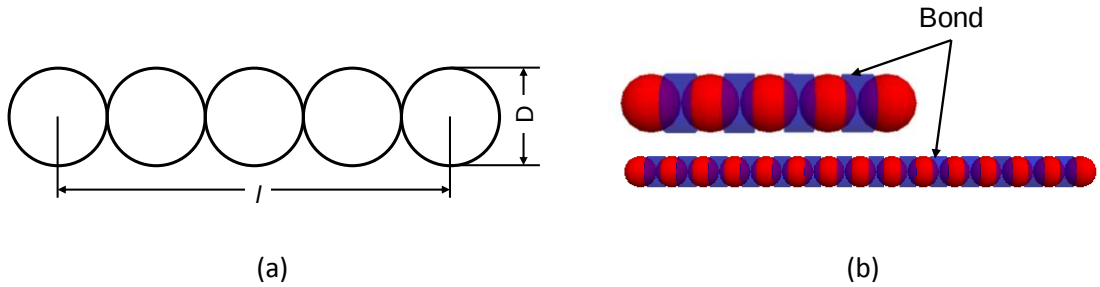

Fig. 4.6. Virtual fibres; (a) dimensions of a virtual fibre, *l* is fibre length, D fibre is diameter; (b) examples of PFC^{3D} virtual fibres.

4.5.1.2. Microproperties of virtual fibre

When using the PFC^{3D} PBM, material to be modeled is defined by three ball microproperties: normal stiffness (k_n), shear stiffness (k_s), and friction coefficient (μ), and five bond microproperties: the radius of the cylindrical bond (R), normal and shear stiffness (*pb_kn* and *pb_ks*), normal and shear strength (σ_c and τ_c). In the case of a fibre subjected to a tensile load, the bond microproperties are more relevant than the ball microproperties as the balls are only in contact with parallel bonds and there will be no

further interaction among the balls under tension. In this study, the previously calibrated ball microproperties (k_n = k_s = 5x10^4 N m^{-1} and μ = 1.0) by Sadek et al. (2011a) were used. The value of *R* was set to be equal to the ball radius, as illustrated in Fig. 4.6b. To reduce the number of bond microproperties to be calibrated, τ_c was set to be equal to σ_c, and *pb_kn* was set to be equal to *pb_ks*. The same assumptions have been made in the literature for modelling other materials (Asaf et al. 2007; McDowell and Harireche, 2002). On the other hand, τ_c and *pb_ks* are not critical in this particular case having tensile load only. In summary, only σ_c and *pb_kn* were unknown.

4.5.1.3. Virtual tensile test

A virtual fibre with the desired diameter and length was first constructed using balls and bonds as described above. The centre of the first ball of the virtual fibre was set as the origin of the coordinate system and the *x*-axis was along the centre line of the virtual fibre (Fig. 4.7). To simulate a tensile test, the ball at the origin was fixed by applying a zero velocity boundary condition to it. All other balls in the virtual fibre are free to move. A tensile load along the x-axis was applied at the free end of the virtual fibre by pulling the last ball at a constant velocity. This model simulates the laboratory tests conducted with the Instron testing system, and it allows altering magnitudes of fibre diameter, length, pulling velocity, and microproperties.

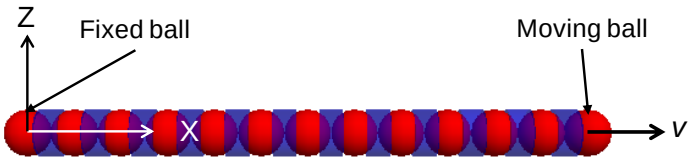

Fig. 4.7. A virtual fibre subjected to a pulling action at a constant velocity, *v*.

During the virtual testing, the velocity of the last ball will cause increasing extension of the virtual fibre and increasing tensile load within the virtual fibre, more specifically within the cylindrical bonds. The extension and stress of the virtual fibre is mainly determined by the microproperties of the bond. The virtual fibre will fail if the maximum tensile load exceeds the tensile strength of the bond. This concept has been verified in PFC^{3D} using an example of a cantilever beam subjected to a tensile load (Itasca 2008). Given these facts, the bond strength, σ_c, was envisioned to be equivalent to the maximum stress measured in the tensile tests, while the bond stiffness, *pb_kn*, was being calibrated, as described in the model calibration section.

4.5.1.4. Model behaviour

Before calibrations, the behaviour of the model was observed through simulating the unretted and retted fibres tested. The model input parameters are listed in Table 4.2. At that point, the value of the bond stiffness was assumed.

Table 4.2. Model input parameters for simulations

Model parameters	**Unretted**	**Retterd**	**Source**
Length of the fibre, mm	25	25	Same as the fibre samples tested
Diameter of the fibre, mm	0.34	0.30	Average of all the fibre samples
Number of balls	74	84	Determined using Equation (2)
Ball normal and shear stiffness, N m^{-1}	$5x10^4$	$5x10^4$	Sadek et al. (2011)
Ball friction	1.0	1.0	Sadek et al. (2011)
Bond normal and shear strength, Pa	$3.58x10^8$	$3.43x10^8$	Average maximum stress measured
Diameter of the cylindrical bond, mm	0.34	0.30	Equal to the fibre diameter

4.5.1.5. Failure pattern of virtual fibre

When a tensile load is applied to a virtual fibre, i.e. when the ball at the free end of the fibre is being pulled at a constant velocity, the virtual fibre is extended. Then, detachment between balls within the virtual fibre occurs (Fig. 4.8), and the virtual fibre is considered to be broken at that stage. The example shown in Fig. 4.8 has four breaking points, and they appeared to be in random locations along the fibre. At those points, there are no more bonds between the balls. This was because bond exists only when two balls are in contact in PFC^{3D}.

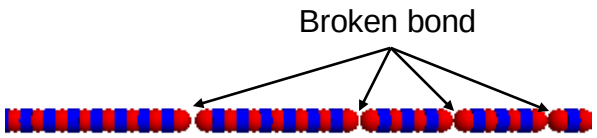

Fig. 4.8. Screenshot from a virtual tensile test showing failure of a virtual fibre.

As the virtual fibre continues to be pulled, the stress of the virtual fibre is increasing in a linear fashion and fails suddenly. The extension of the virtual fibre is considered as the displacement of the last ball along the x-axis direction. This displacement and the stress of virtual fibre were monitored and plotted in Fig. 4.9. Although not all load-extension curves from the virtual tests were like those from the laboratory tests shown in Fig. 4.5, the general behaviour of the load increasing with extension and the sudden failure pattern were similar between the virtual and laboratory tests.

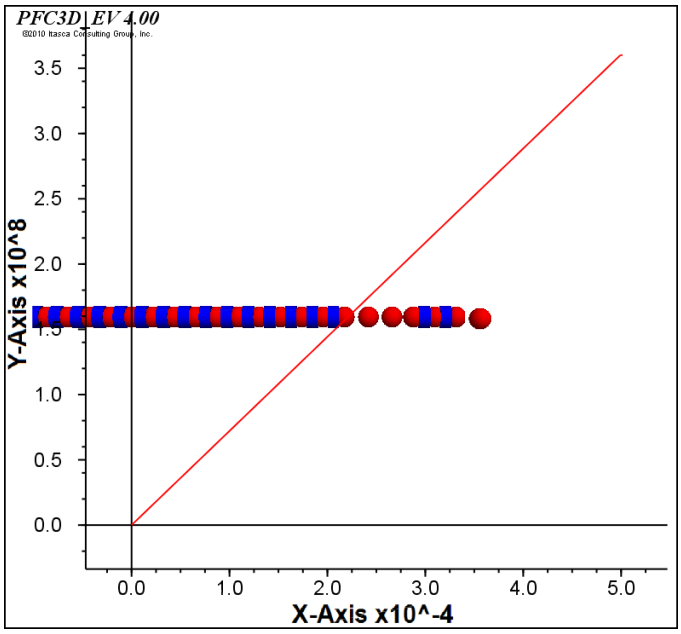

Fig. 4.9. A typical load-extension curve from a virtual tensile test.

4.5.2. Model Calibration and Validation

4.5.2.1. Calibration of bond stiffness

In running the model for calibrations of *pb_kn*, comparisons in stress are being made between simulated and measured fibre stresses at very computing cycle. When the stress of the virtual fibre reaches the maximum stress measured, the extension of the virtual fibre was recorded as the elongation of the virtual fibre and the simulation ends shortly. The input parameters are those listed in Table 4.2, together with different assumed values of *pb_kn.* The simulated elongation was recorded for each of the assumed *pb_kn* values. To assess which assumed value of *pb_kn* results in the elongation which best match the measured elongation, relative errors between simulations and measurements were calculated using the following equation:

$$RE = \frac{(e_m - e_s) \times 100}{e_m} \tag{4.3}$$

where

RE = relative error (%),

e_m = elongation measured (mm),

e_s = elongation simulated (mm).

The results revealed that fibre elongations are extremely sensitive to the *pb_kn*. Some of the results are listed in Table 4.3 to demonstrate how the calibrated *pb_kn* was selected. As can be seen, the assumed value of *pb_kn*, $1x10^{14}$ Pa m^{-1} resulted in the best match to the measurements for both the unretted and retted fibres, and the corresponding relative

errors are 2% and 1% respectively. Whereas either increasing or decreasing the *pb_kn* value results in a much greater relative error. Therefore, $1x10^{14}$ Pa m^{-1} was selected as the final calibrated *pb_kn* for both fibres.

Table 4.3. Summary of calibration results using the data from the unretted and retted fibres

Bond stiffness, Pa m^{-1}	**Unretted**			**Retted**		
	Measured elongation, mm	Simulated elongation, mm	Relative error, %	Measured elongation, mm	Simulated elongation, mm	Relative error, %
$1x10^{13}$	0.88	3.22	266	0.80	3.32	315
$5x10^{13}$	0.88	1.12	27	0.80	1.07	33
$1x10^{14}$	0.88	0.86	2	0.80	0.79	1
$5x10^{14}$	0.88	0.65	26	0.80	0.57	29
$1x10^{15}$	0.88	0.63	28	0.80	0.54	32

4.5.2.2.Effects of fibre length and diameter on fibre elongation

Once the bond stiffness was calibrated, the model can be used to predict elongations for fibres with any length and diameter. Here, virtual tensile tests were performed with the calibrated model for five different fibre lengths: 20, 25, 30, 35 and 40 mm with a constant fibre diameter of 0.30 mm to examine effects of fibre length on elongation. Similarly, simulations were performed for five different diameters: 0.20, 0.25, 0.30, 0.35 and 0.40 mm with a constant fibre length of 30 mm to examine effects of fibre diameter on elongation. The simulation results show that elongation is increased linearly (R^2 = 0.99)

with the increase of the fibre length (Fig. 4.10a). The simulated elongations range from 0.24 to 0.48 mm when fibre length varies from 20 to 40 mm. The average of the maximum strains is 1.18% with a very small standard deviation: 0.0049%. The small standard deviation means that length has little influence on the maximum strain. This implies that model is reliable for simulations of all fibre lengths. Elongation is affected by the fibre diameter in a reverse trend (Fig. 4.10b). Elongation decreases with the increase of the fibre diameter in a power curve (R^2 = 0.99). The simulated elongations vary from 0.27 to 0.54 mm, meaning that the strains vary between 0.89% and 1.79%. The results indicated that fibre diameter has more influence on the elongation than fibre length, which reflects the reality.

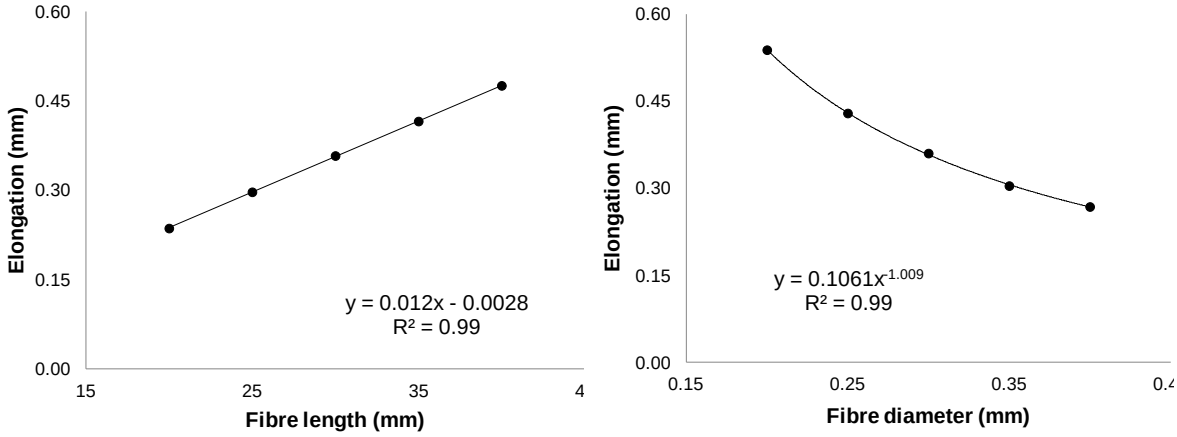

(a) (b)

Fig. 4.10. Model result of fibre elongation: (a) effect of fibre length, (b) effect of fibre diameter.

4.5.2.3. Validation of fibre elongation

The calibrated model was validated, in terms of its output of elongation. This was done using the literature data of tensile tests of hemp fibre conducted by Khan et al. (2011). The setup of the tests and results of interest are briefly summarised here for the information of the readers. Samples of hemp fibre were obtained from manual processing of unretted hemp. An Instron machine was used for the tensile tests. Effective length of fibre samples was 35 mm. The average diameter of 75 fibre samples was 0.27 mm, and the average measured elongation and strength of all samples was 0.56 mm and 3.58×10^8 Pa respectively. The inputs for the model validation are listed in Table 4.4.

Table 4.4. Model input parameters for validations

Model parameters	**Value**	**Source**
Fibre length, mm	35	Khan et al. (2011)
Fibre diameter, mm	0.27	Khan et al. (2011)
Number of balls	105	Determined using Equation (2)
Ball normal and shear stiffness, N m^{-1}	5×10^4	Sadek et al. (2011)
Ball friction	1.0	Sadek et al. (2011)
Bond normal and shear strength, Pa	3.58×10^8	Maximum stress measured
Diameter of the cylindrical bond, mm	0.27	Equal to the fibre diameter
Bond normal and shear stiffness, Pa m^{-1}	1×10^{14}	Calibrated

To validate the model, the virtual fibre with the specific diameter and length was constructed. The simulation results showed an elongation of 0.46 mm for the specific fibre. As compared with the literature data of elongation, 0.56 mm, the relative error of

the model was found to be 17.5%. Relative errors below 20% are considered to be acceptable for materials with highly variable nature of properties, such as hemp fibre.

4.6. CONCLUSION

Hemp fibres (fibre bundles) can be simulated with the numerical model developed using PFC^{3D}, a commercial discrete element software. A virtual fibre, formed using spherical particles connected with bonds implemented in the PFC^{3D} parallel bond model, reflects tensile behaviours of real fibre. Specifying a given velocity to one end of the virtual fibre represents well a tensile load, while the other end of the virtual fibre is affixed. The model is capable of simulating numerous tensile behaviours of fibre, including load-extension curve, maximum stress, and elongation. The model allows users to alter diameter and length of the fibre. Among the several microproperties for particles and bonds in a virtual fibre, the bond microproperties in the normal direction are more critical as they determine the tensile strength of the virtual fibre. An important microproperty, normal bond strength, can be envisioned as the strength (maximum stress) of the fibre. Another important microproperty, normal bond stiffness, can be calibrated through matching elongation behaviours between virtual and real fibres. The calibrated normal bond stiffness using the laboratory tensile test data from both unretted and retted fibres was $1x10^{14}$ Pa m^{-1} with a relative error of 2% and 1% respectively. The elongation predicted by the calibrated model was comparable with the literature data with 17.5% relative error.

4.7. REFERENCES

Asaf, Z., D. Rubinsteinand and I.Shmulevich. 2007. Determination of discrete element model parameters required for soil tillage. *Soil and Tillage Research* 92(2): 227-242.

Beckermann, G. W. and K. L. Pickering. 2008. Engineering and evaluation of hemp fibre reinforced polypropylene composites: Fibre treatment and matrix modification. *Composites: Part A* 39: 979-988.

Bledzki, A. K., S. Reihmane, and J. Gassan. 1996. Properties and modification methods for vegetable fibers for natural fiber composites. *Journal of Applied Polymer Science* 59(8): 1329–1336.

CGSB. 2001. Conditioning textile materials for testing. Canadian General Standards Board and Standards Council of Canada, CAN/CGSB-4.2 no. 2-M88.

Chang, C. S., C. L. Liao and Q. Shi. 2003. Elastic granular materials modeled as first order strain gradient continua. *International Journal of Solids and Structures* 40: 5565–5582.

Coetzee, C. J. and D. N. J. Els. 2009. Calibration of discrete element parameters and the modelling of silo discharge and bucket filling. *Computers and Electronics in Agriculture* 65: 198–212.

Cundall, P. A., and Strack, O. D. L. (1979). A discrete numerical model for granular assemblies. *Geotechnique*, 29, 47-65.

Cundall, P. A. and O. D. L. Strack. 1982. Modeling of microscopic mechanics in granular material. In: J. T. Jenkins, and M. Satake (Eds.), *Mechanics of Granular*

Materials: New Models and Constitutive Relations (pp. 113–149). Amsterdam: Elsevier.

Djordjevic, N. 2003. Discrete element modeling of the influence of lifters on powder draw of tumbling mills. *Minerals Engineering* 16: 331-336.

Franco, Y., D. Rubinsteinand and I. Shmulevich. 2007. Prediction of soil-bulldozer blade interaction using discrete element method. *Transactions of the ASABE* 50(2): 345-353.

Garcia, C., D. D. Jaldon and M. R. Vignon. 1998. Fibres from semi-retted hemp bundles by steam explosion treatment. *Biomass and Bioenergy* 14(3): 251-260.

Hobson, R. N., D. G. Hepworth and D. M. Bruce. 2001. Quality of fibre separated from unretted hemp stems by decortication. *Journal of Agricultural Engineering Research* 78(2): 153-158.

Itasca. 2008. PFC^{3D} particle flow code in 3 dimensions, verification problems and example applications. Itasca Consulting Group, Inc. Minneapolis, Minnesota, USA.

Khan, M. R., Y. Chen, T. Belsham, C. Lague, H. Landry, Q. Peng, and W. Zhong. 2011. Fineness and tensile properties of hemp (Cannabis sativa L.) fibres. *Biosystems Engineering* 108(1): 9-17.

Kymäläinen, H. R. 2004. Quality of *Linum usitissimum* L. (flex and linseed) and *Cannabis sativa* L. (hemp fibre) during the production chain of fibre raw material for thermal insulation. Helsinki, Finland: Department of Agricultural Engineering and Household Technology, University of Helsinki.

Landry, H., C. Laguë, and M. Roberge. 2006. Discrete element representation of manure products. *Computers and Electronics in Agriculture* 51: 17-34.

Landry, H., F. Thirion, C. Laguë, and M. Roberge. 2006. Numerical modeling of the flow of organic fertilizers in land application equipment. *Computers and Electronics in Agriculture* 51: 35-53.

Lilholt, H. and J. M. Lawther. 2000. Natural organic fibers. In A. Kelly, and C. Zweben (Eds.), *Fibre reinforcements and general theory of comprehensive composite materials* (pp. 303-325). Amsterdam: Elsevier.

Lu, Z., S. C. Negi and J. C. Jofriet. 1997. A numerical model for flow of granular materials in silos. Part 1: model development. *Journal of Agricultural Engineering Research* 68: 223-229.

Mak, J., Y. Chen and M. A. Sadek. 2012. Determining parameters of a discrete element model for soil–tool interaction. *Soil and Tillage Research* 118: 117–122.

McDowell, G. R. and O. Harireche. 2002. Discrete element modeling of yielding and normal compression of sand. *Geotechnique* 52(4): 299-304.

Mediavilla, V., M. Leupin, and A. Keller. 2001. Influence of the growth stage of industrial hemp on the yield formation in relation to certain fibre quality traits. *Industrial Crops and Products* 13: 49-56.

Munder, F. and C. Fürll. 2004. Effective processing of bast fiber plants and mechanical properties of the fibers. ASAE/CSAE Annual International Meeting, Ottawa, Ontario, Canada.

Ni, Q., W. Powrie, X. Zhang and R. Harkness. 2000. Effect of particle properties on soil behaviour: 3-D numerical modeling of shearbox tests. In Numerical Methods in Geotechnical Engineering (GSP 96), 58-70. Reston, VA, USA: ASCE.

Pierce, M. E. 2004. PFC^{3D} modeling of inter-particle percolation in caved rock under draw. In Y. Shimizu, R. Hart, and P. A. Cundall (Eds.), *Numerical Modeling in Micromechanics Via Particle Methods* (pp. 149-156). Kyoto: Taylor and Francis.

Potyondy, D. O. and P. A. Cundall. 2004. A bonded-particle model for rock. *International Journal of Rock Mechanics and Mining Sciences* 41(8): 1329-1364.

Rothenburg, L. and J. R. Bathurst. 1989. Analytical study of anisotropy in idealized granular materials. *Geotechnique* 39 (4): 601–614.

Rowell, R. M., J. S. Han and J. S. Rowell. 2000. Characterization and Factors Effecting Fiber Properties. *Natural Polymers and Agrofibers Composites* 115-134.

Sadek, M. A., Y. Chen, C. Laguë, H. Landry, Q. Peng and W. Zhong. 2011a. Characterization of the shear properties of hemp using discrete element method. *Transaction of the ASABE* 54(6): 2279-2285.

Sadek, M. A., Y. Chen, and J. Liu. 2011b. Simulating shear behavior of a sandy soil under different soil conditions. *Journal of Terramechanics* 48: 451–458.

Sakaguchi, F., M. Suzuki, J. F. Favierand and S. Kawakami. 2001. Numerical simulation of the shaking separation of paddy and brown rice using the discrete element method. *Journal of Agricultural Engineering Research* 79(3): 307-315.

Sankari, H. 2000. Comparison of bast fibre yield and mechanical fibre properties of hemp (Cannabis sativa L.) cultivars. *Industrial Crops and Products* 11: 73-84.

Saville, B. P. 1999. Physical Testing of Textiles. Textile Institute. Manchester, England. Woodhead publishing.

Schäfer, T. and B. Honermeier. 2006. Effect of sowing date and plant density on the cell morphology of hemp (Cannabis sativa L.). *Industrial Crops and Products* 23: 88-98.

Tanaka, H., M. Momozo, A. Oida, and M. Yamazaki. 2000. Simulation of soil deformation and resistance at bar penetration by distinct element method. *Journal of Terramechanics* 37: 41–56.

Van der Linde, J. 2007. Discrete element modeling of a vibratory subsoiler. Matieland, South Africa: Department of Mechanical and Mechatronic Engineering, University of Stellenbosch.

Vu-Quoc, L., X. Zhang, and O. R. Walton. 2000. A 3-D discrete-element method for dry granular flows of ellipsoidal particles. *Computer Methods in Applied Mechanics and Engineering* 187: 483–528.

Walton, K. 1987. The effective elastic moduli of random packing of spheres. *Journal of the Mechanics and Physics of Solids* 35(3): 213–226.

Williams, G. I. and R. P. Wool. 2000. Composites from natural fibers and soy oil resins. *Applied Composite Materials* 7: 421-432.

Chapter 5

Discrete Element Modeling of Hemp Processing using a Hammermill

5.1. SIGNIFICANCE

The application of the discrete element method (DEM) to a hammermill for hemp processing posses the challenge of defining virtual hemp particles and a virtual hammermill. No literature was found which numerically simulate the interactions between hemp material and machines. In the previous chapters, only virtual fibre and core particles were defined and microproperties were determined for only fibre and core particles. It would be logical to define a virtual hemp stem and establish its microproperties at this stage. This information could be then applied to understanding the breaking mechanism and the dynamic behaviour of hemp material subjected to different hammermill operating conditions. This chapter corresponds to objective 3 of the thesis.

5.2. ABSTRACT

The discrete element method (DEM) was used to develop a model which simulates hemp processing using a hammermill. The model was computed using the Particle Flow Code in Three Dimensions (PFC^{3D}). In the model, a virtual hemp stem was defined using spherical particles connected with parallel bonds implemented in the PFC^{3D}. The breakage of the bonds mimics the hemp breaking phenomenon within the hammermill. A

microproperty, bond strength of the hemp stems was calibrated using the literature data from compression tests of hemp stems. The calibrated bond strength was 2.2 $x10^6$ Pa. With the calibrated bond strength, the model was used to simulate the power and energy distributions within the hammermill. The simulations were performed for different hammer rotational speeds and feeding masses. The results showed that both the specific kinetic and strain energies increased with the increase of the feeding mass however the effects of the hammer rotational speed did not follow any particular trends.

5.3. INTRODUCTION

Hammermill has been used for processing a wide range of materials because of its high processing capacity, simple design, and versatility. For example, hammermill is used for biomass size reduction in forage industry (Shi et al., 2003) and agriculture (Mani et al., 2004; Miao et al., 2011). A hammermill is an energy intensive machine. Energy consumption of hammermill depends on many factors including particle size and moisture content of the feed, feeding rate, screen opening, and operational conditions of the hammermill (Yu et al., 2006; Lopo, 2002; Shi et al., 2003; Vigneault et al., 1992). Djordjevic et al. (2003) reported that the specific energy was independent of particle size at low rotational speeds. With a higher rotational speed the specific energy increases significantly below certain particle sizes, but decreases for larger particle sizes. Higher moisture content resulted in higher energy consumption when a hammermill was used for processing biomass (switchgrass, barley, and wheat straw) (Mani et al., 2004; Miao et al., 2011).

Baker (2009) studied hemp processing using a hammermill and reported that larger feed mass required more energy for processing. That study also found that when using smaller screen opening, more power was required to process hemp. Similar results were reported by other researchers (Yu et al., 2006; Savoie et al., 1989). All those experimental studies, except for Baker (2009), concerned materials other than hemp.

During hemp processing using a hammermill, hemp stalk is impacted by rapidly rotating hammers, breaking hemp stalk into pieces. This dynamic process is complicated, involving particle movement and contact forces between particles and machine parts. These dynamic behaviours are important as they determine the energy requirement of the hammermill. Due to the non-homogenous nature of hemp material and larger displacement of particles, it is not possible to quantify this dynamic behaviour using analytical methods or traditional numerical methods. Therefore, the discrete element method (DEM) was used in this study to understand the dynamic behaviour of hemp material impacted by highly rotating hammers.

The discrete element method (DEM) is a promising tool to study particle dynamic behaviours like the interaction between hemp particles and rotating hammers. The DEM is a numerical method which models a material as an assemblage of discrete particles. The DEM was first introduced by Cundall and Strack (1979) to model the dynamics of the rocks. Since then DEM has been used in diverse areas including milling machines, such as ball mill (Cleary, 1998, 2000; van Nierop et al., 2001; Mishra and Murty, 2001), tumbling mill (Djordjevic, 2003); SAG mill (Rajamani et al., 2000), centrifugal mill

(Inoue and Okaya, 1996; Cleary and Hoyer, 2000), and impact crusher (Hammermill) (Djordjevic et al., 2003). Little work has been done for hammermill.

In this study, the DEM method was used to model the interaction of hemp particles and hammermill. The computation of the model was done using the Particle Flow Code in Three Dimensions (PFC^{3D}) (Itasca Consulting Group, Inc., Minneapolis, MN). PFC^{3D} works with two major components, Ball and Wall. Balls are spherical in shape and walls are rectangular, cylindrical, ring, disc, or 3D line shaped. Materials to be simulated are represented by assemblies of individual balls. A group of balls can be arranged together to simulate any arbitrary shape of particle assembly. Particles in an assembly could be either bonded together or free flowing. Depending on the nature of the materials to be simulated. A set of microproperties need to be assigned to the balls and bonds, so that the model particles behave as the real material particles to be simulated. Those microproperties either need to be determined from the theory or calibrated before the simulation. Fundamental material property tests can be used for calibrations. For example, Franco et al. (2007) and Coetzee and Els (2009) used direct shear tests to calibrate model microproperties of a soil through matching simulated friction angles with measured angles of the soil. Sadek et al. (2011) also used direct shear tests in calibrating some microproperties of hemp fibre and core (ground), and those calibrated microproperties were used in the simulations of this study, and additional microproerties required were calibrated in this study using compression tests.

In summary, understanding the interaction between hemp particles and a hammermill is essential to the understanding of energy consumption of the hammermill. The objectives of the study were

(a) to develop a model to simulate hemp processing with a hammermill using PFC^{3D};

(b) to calibrate a model microproperty using compression tests of hemp stem;

(c) to simulate the power requirement of a hammermill and the dynamic behaviour of hemp particles under different operating conditions of hammer mill.

5.4. METHODOLOGY

5.4.1. Defining Virtual Hemp

5.4.1.1. Structure of virtual hemp

A real hemp stem has a hollow structure, mainly consisting of core surrounded by a thin layer of bast fibre (Fig. 5.1a). In constructing a virtual hemp stem, a set of PFC^{3D} basic particles (balls) connected with bonds using PFC^{3D} cluster logic. Balls in the cluster were arranged as a hollow structure as shown in Fig. 5.1b. The construction process starts with a circle of a desired diameter, and then extending along the axial direction up to a desired length. Two layers of balls were used for the virtual hemp stem to have sufficient structure for internal fracturing. All the balls in a virtual hemp stem had the same diameter. Then, the PFC^{3D} Parallel-Bonds were installed between all balls which are in

contact. The bonds connect balls over a circular cross-section lying on the contact plane between the balls. In PFC^{3D}, a ball is considered to be rigid body and cannot be broken (Itasca, 2008). Thus, breaking of the virtual hemp means breaking of the bonds only.

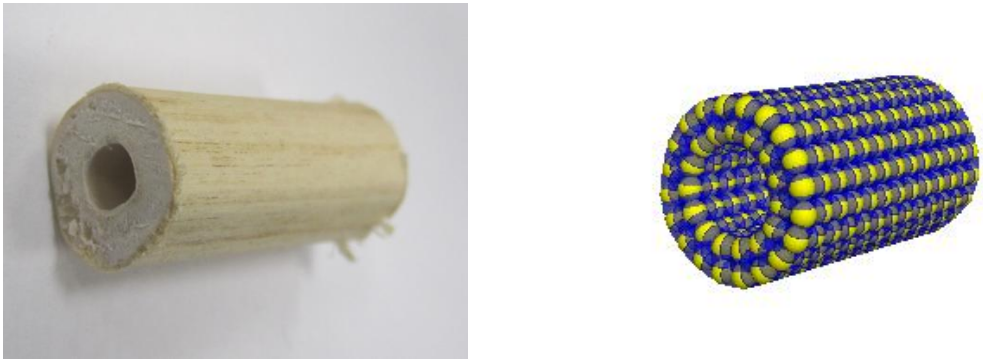

(a) (b)

Fig. 5.1. Hemp stem; (a) Real, (b) virtual.

5.4.1.2. Microproperties of virtual hemp

In PFC^{3D}, the virtual hemp described above is defined by a set of ball and bond microproperties. The ball microproperties include normal stiffness (K_n), shear stiffness (K_s), and friction coefficient (μ), and the bond microproperties include normal and shear stiffness ($\bar{k}^n$ and $\bar{k}^s$), normal and shear strength (σ_c and τ_c), and the bond-radius multiplier (λ). The bond-radius multiplier is the ratio of the bond radius and ball radius. Calibrations of these microproperties are essential to simulate the behaviours of any materials. However, only one of these parameters can be calibrated at one time. Others need to be determined based on literature, theories, or assumptions.

Sadek et al. (2011) has calibrated the ball properties of hemp fibre and core. Their values for core (K_n = K_s = 5x10^4 N m^{-1} and μ = 1.0) were used in this study to represent the ball microproperties of virtual hemp stem, as a hemp stem is mainly composed of core. For bond microproperties, τ_c was set to be equal to σ_c, and $\bar{k}^n$ was set to be equal to $\bar{k}^s$ to reduce the number of unknowns. Similar assumptions have been made in the literature for modelling other materials (Asaf et al., 2007; McDowell and Harireche, 2002). The value of λ was set to be equal to one for the maximum contact areas between balls and bonds.

The bond stiffness, $\bar{k}^n$ was determined based on its relationship with the ball stiffness, K_n. Potyondy and Cundall (2004) described the following relationship between stiffness and Young's modulus. For balls,

$$K_n = 4RE_c \tag{5.1}$$

where

K_n = Stiffness of the ball (N m^{-1}),

R = radius of the ball (m),

E_c = Young's modulus of ball (Pa).

For bonds,

$$\bar{k}^n = \frac{\bar{E}_c}{R^A + R^B} \tag{5.2}$$

where

$\bar{k}^n$ = Stiffness of the bond (Pa m^{-1}),

R^A, R^B = radius of two connecting ball A and B respectively (m),

$\bar{E}_c$ = Young's modulus of bond (Pa).

Here the radius of the balls is known. Assuming $E_c = \bar{E}_c$ and using the value of K_n, $\bar{k}^n$ can be determined. Thus, only the bond strength, σ_c needs to be calibrated.

5.4.2. Calibration of the Bond Strength

Literature data were available for compression of hemp stems (Khan et al., 2010). To use those data for calibrations, virtual compression tests were conducted using PFC^{3D}. The maximum breaking strength of hemp stem obtained from the virtual tests was compared with data from Khan et al. (2010) to calibrate the bond strength. The calibration process is described in detail in the following sections.

5.4.2.1. Source of the literature data

Data for calibrations were from compression tests of hemp stems conducted by Khan et al. (2010). Here is a brief description of their tests for readers' information. All specimens of hemp stem used in the compression tests were 25 mm long (Fig. 5.2a). A universal testing system (Fig. 5.2b) was used to compress the hemp specimens. As the compression rod of the testing system moved down, the hemp specimen subjected a vertical load. The force-displacement curve of specimen was recorded until the specimen failed. The maximum compressive force was then identified from the recorded curve. A

total of 240 specimens were tested by Khan et al. (2010). Those specimens had an average diameter and an average wall thickness of 10 mm and 4 mm, respectively. The average maximum compressive force of those specimens was 93.67 N. These average values were used in this study for calibrations of the bond strength.

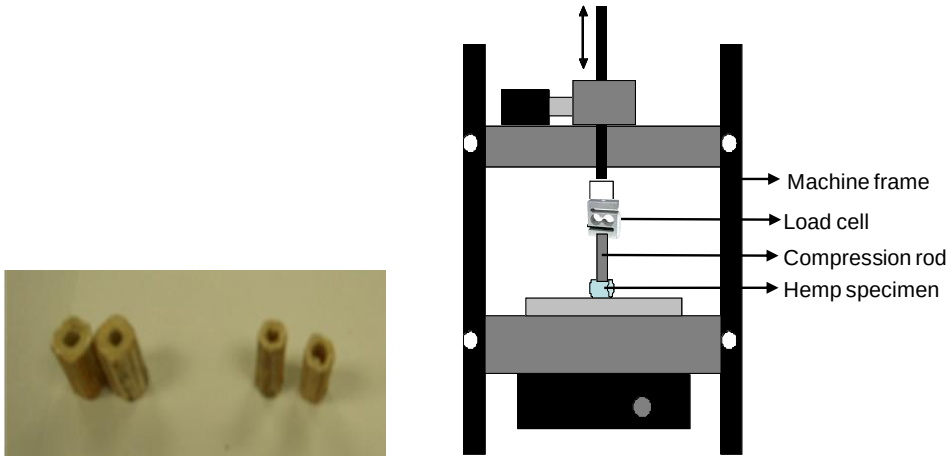

(a) (b)

Fig. 5.2. Compression test of the hemp stem; (a) hemp specimen, (b) schematic of universal testing system (Khan et al. 2010).

5.4.3. Virtual Compression Test

Virtual compression test was conducted to simulate the compression tests conducted by Khan et al. (2010). A virtual platform was constructed using the PFC^{3D} wall commands to simulate the universal testing system shown in Fig. 5.2b. The platform consisted of a rectangular base and a compression rod (Fig. 5.3). A virtual hemp stem with the diameter 10 mm, thickness 4 mm and length 25 mm was placed on the top of the rectangular base. These dimensions were the same as the average dimensions of those specimens used by Khan et al. (2010). The bond stiffness was calculated as 2.5×10^9 Pa m^{-1} using these

dimensions based on Eqs. 1 and 2. The centre of the virtual hemp stem was lined up with the centre of the compression rod. Therefore, the compression force was applied at the centre of the virtual hemp stem.

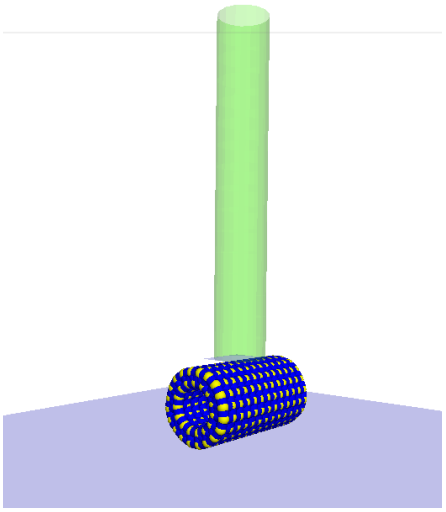

Fig. 5.3. Virtual platform and hemp stem for simulating compression tests.

A constant downward velocity was applied to the compression rod to simulate the compression test. The compression rod moved down until the hemp stem fails, reflected by the drop of the force. The total force acting on the compression rod was considered as the compression force. The force-displacement of the rod was recorded during the virtual test. The maximum compression force was read from the first peak point of the force curve.

5.4.4. Hammermill Model Development

The main components of a real hammermill typically include a drum, hammers mounted on the drum, and a housing which has a screen at the bottom. When the hammermill is in operation, the drum and hammers rotate at a high speed. The rotating hammers impact the hemp being fed into the housing. As the result, the hemp stalk is broken into pieces. Small pieces fall down through the screen and discharged into the "fine" stream or waste stream, and large pieces are collected as the main product. These main features of hammermill were used to develop a virtual hammermill in this study.

5.4.4.1. Virtual hammermill and virtual hemp generation

The virtual hammermill consisted of a housing, a drum, six hammers, and a screen, which were simplified as PFC^{3D} walls and lines (Fig. 5.4). A cylindrical wall was placed at the centre to make the drum. Six hammers were made with three intersecting flat walls passing through the centre of the drum. The hammers were surrounded by a cylindrical mesh functioning as a screen. The mesh was constructed by using numerous rings around the axis of the drum and numerous lines on the periphery of the rings along the axis of the drum. Both rings and lines were spaced 20 mm to obtain a mesh opening of 20 mm. Then the whole assembly was fitted in to box shaped housing constructed using flat walls. The dimensions of the virtual hammermill were similar to the hammermill used by Baker (2009) for processing hemp. The diameter of the drum was 560 mm. The three crossing walls extended 175 mm outside the drum, which was the effective hammer length.

In practice, before fed to a hammermill, hemp stalk may be cut into segments, for example, 40 mm long segments (Baker, 2009). Therefore, the virtual hemp segments of 40 mm length were fed into the hammermill. As PFC^{3D} does not allow generating particle clusters like the virtual hemp stems defined above, the assembly of segments were generated in several steps. The first step was generating balls into the virtual hammermill. The second step was replacing the balls with clumps. The clumps had the same shapes and dimensions as the virtual hemp segments. A clump in PCF^{3D} is a rigid body formed by a set of balls attached together, and it cannot be broken by force. The final step was converting the clumps to clusters by releasing the balls within the clump without changing the shapes and dimensions. Then the selected and calibrated microproperties were assigned to the particles and bonds. Figure 5.4 shows the hemp segment distribution in the virtual hammermill. The number of hemp segments is determined based on the feed mass desired.

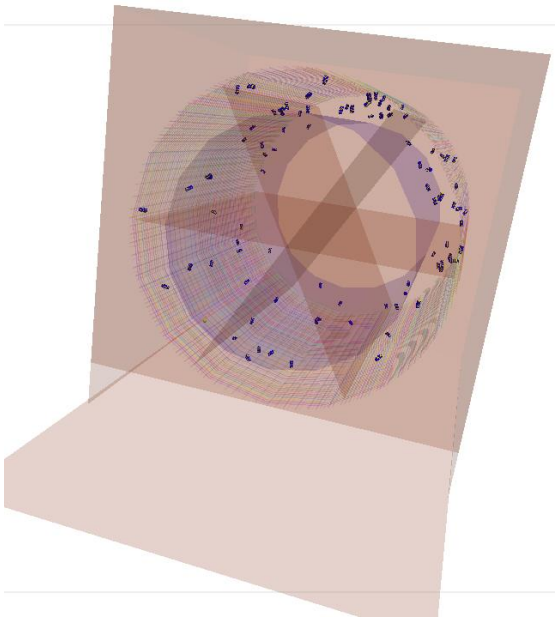

Fig. 5.4. Hemp segments generated in the hammermill.

5.4.4.2. Simulations of hammermill operation

After generating the virtual hemp segments into the hammermill, the hammermill was assigned a rotational speed. The model allowed changing the operational parameters, including feed mass, rotational speed, and duration. The simulation allows one to observe the dynamic behaviors of hemp particles while being processed in the hammermill. In this study, the dynamic attributes of interest included the power requirement of the hammermill as well as the particle kinetic and strain energies. These attributes were recorded using the PFC^{3D} history command during the simulations.

Power of the virtual hammermill was determined from the power applied to the virtual hammers by all moments and forces arising from all particles which are contacting the hammers. The average power of the six individual hammers was considered as the virtual hammermill power.

Total kinetic energy of particles is the energy of all balls accounting for both translational and rotational motions. Total kinetic energy is expressed as (Itasca, 2008)

$$E_k = \frac{1}{2}\sum_{N_b}\left(m_i V_i^2 + I_i \omega_i^2\right) \tag{5.3}$$

where

E_k = kinetic energy (J),

N_b = number of balls,

m_i = inertial mass of ith body (kg),

I_i = inertia tensor of i^{th} body (kg m^2),

V_i = translational velocities of i^{th} body (m s^{-1}),

ω_i = rotational velocities of i^{th} body (Radian s^{-1}).

Total strain energy is the energy of the entire assembly stored at all contacts. Total strain energy is expressed by (Itasca 2008)

$$E_s = \frac{1}{2}\sum_{N_c}\left(\left|F_i^n\right|^2/\bar{k}^n + \left|F_i^s\right|^2/\bar{k}^s\right) \tag{5.4}$$

where

E_s = strain energy (J),

N_c = number of contacts,

$\left|F_i^n\right|$ = magnitudes of the normal components of the i^{th} contact force (N),

$\left|F_i^s\right|$ = magnitudes of the shear components of the i^{th} contact force (N),

$\bar{k}^n$ = bond normal stiffness (Pa m^{-1}),

$\bar{k}^s$ = bond shear stiffness (Pa m^{-1})

5.5. RESULTS AND DISCUSSION

5.5.1. Calibration Results

5.5.1.1. Compression behaviour of hemp

The loading condition of the specimen is illustrated in Fig. 5.5. The virtual compression tests using the constructed compression platform (Fig. 5.6a) showed that breakage of the specimen occurred at the bonds and fracturing of the specimen followed several steps. At the beginning of the compression, fracturing occurred near the contact point between the specimen and the base of the compression platform, followed by fracturing on the sides of the specimen, resulting in the specimen being broken into three pieces (Fig. 5.6b). Finally, fractures were developed at the top of the specimen, resulting in the specimen being broken into four pieces (Fig. 5.6c).

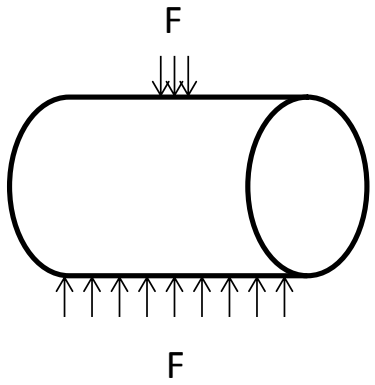

Fig. 5.5. Free body diagram of compression load on the hemp stem.

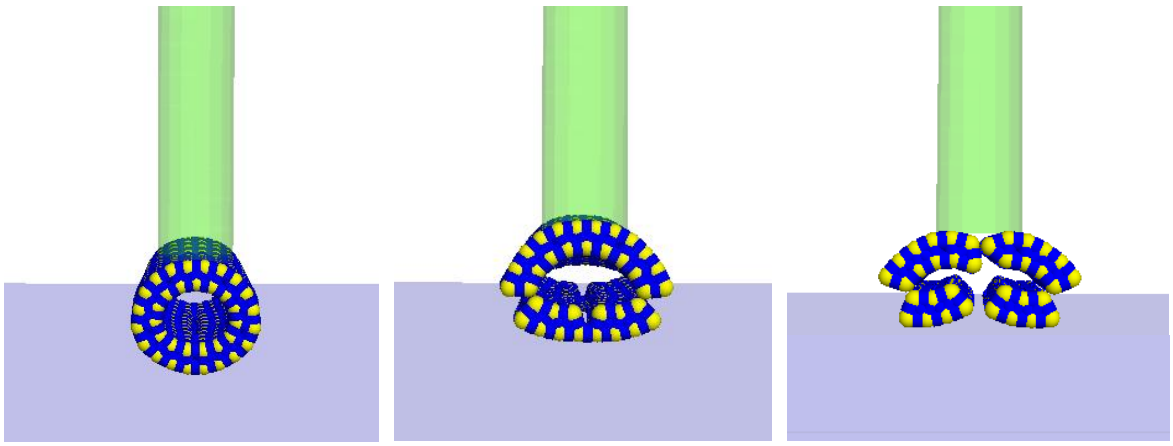

(a) (b) (c)

Fig. 5.6. Breaking steps of hemp specimen during a virtual compression test.

The sequence of the fracturing of the specimen can be explained through the diagram shown in fig. 5.5. The end cross-section of the specimen subjects to the reaction force throughout the entire length of the specimen at the bottom, and the top subjects to zero force. The stress within the specimen at the bottom is resulting from both the transverse force (compression force) and the resultant moment; the stress at the sides of the specimen is resulting from the transverse force only; whereas the stress at the top of the specimen is zero. This explains the process of the fracturing of the specimen.

Typical force-time curve from the virtual compression test is shown in Fig. 5.7. The curve matches the phenomenon of the breakage shown in Fig. 5.6. When the hemp specimen was compressed, the force increased in a nearly linear fashion; at a certain point, the force reached its peak; then fracturing started within the structure of the specimen. The fluctuating part of the curve is represented by the several steps of the fracturing process. When the entire specimen collapsed, the force dropped completely.

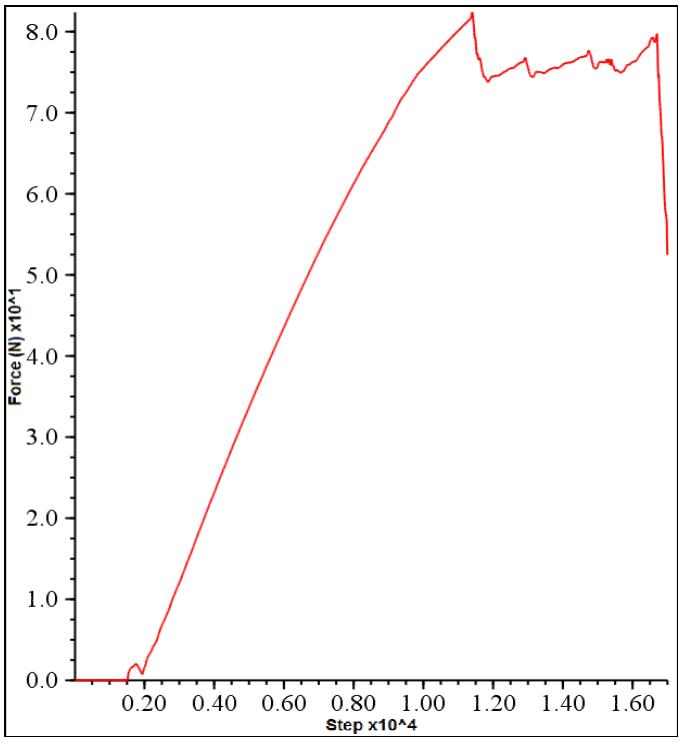

Fig. 5.7. Typical force-time curve obtained in a virtual compression test.

5.5.1.2. Calibrated microproperties

The results from the virtual compression tests were used to calibrate the bond strength of the particles. In the simulations, while keeping the other microproperties constant, the value of bond strength was varied. For each assumed bond strength, the test gave a force-time curve where the maximum force was read and listed in Table 5.1. Then the relative error between each simulated maximum force and the force (93.67 N) measured by Khan et al. (2010) was determined using the following equation:

$$RE = \frac{(f_m - f_s) \times 100}{f_m} \tag{5.5}$$

where

RE = Relative error (%),

f_m = Measured maximum force (N),

f_s = Simulated maximum force (N).

The relative errors for various assumed bond strengths are listed in Table 1. The best match between the simulated and measured maximum forces was when the bond strength was $2.2x10^6$ Pa, as it gave the least relative error: 0.54%. This calibrated value of bond strength was used to simulate hemp processing discussed below.

Table 5.1: Summary of calibration results

Assumed bond strength, Pa	Simulated max. force, N	Relative error, %
$2.0x10^6$	84.65	9.63
$2.2\ x10^6$	93.16	0.54
$2.5\ x10^6$	107.59	14.86
$3.0\ x10^6$	129.35	38.09
$4.0\ x10^6$	352.47	275.79

5.5.2. Hammermill Simulation Results

The calibrated model was used for predicting dynamic behaviours of the hemp particles in the hammermill. The hammermill was operated under three different feed masses and three rotational speeds. The power requirement of the hammermill, the kinetic and strain energies of hemp particles were recorded for each condition.

5.5.2.1. Failure patterns of particles

After being impacted by the rotating hammers, the hollow structures of the hemp segments were broken into clusters of balls. Those clusters had various sizes, depending on the rotational speed of the hammers. It was observed that the overall cluster sizes were smaller, i.e. containing fewer numbers of balls, at a higher rotational speed. With the 1000 rpm speed, most hemp segments were broken along the axial direction, i.e. the most broken pieces kept the whole length of the original hemp segments (Fig. 5.8a). With the 2000 rpm speed, breakage occurred along both axial and radial directions, forming smaller and shorter pieces (Fig. 5.8b). Even smaller and shorter pieces were observed with the 3000 rpm (Fig. 5.8c).

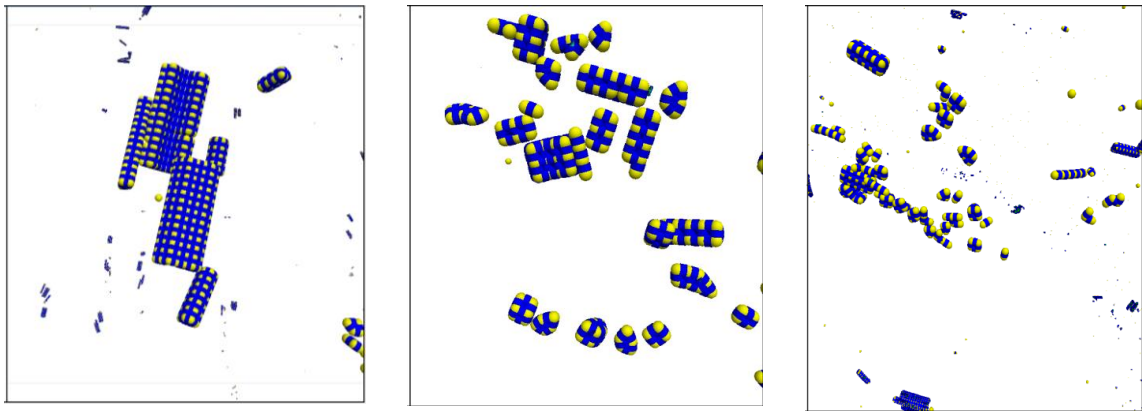

(a) (b) (c)

Fig. 5.8. Screenshots of hemp particles impacted by the hammers at different rotating speeds; (a) 1000 rpm, (b) 2000 rpm, and (c) 3000 rpm.

5.5.2.2. Power requirement of hammermill

Figure 5.9 shows that the power requirement of the hammermill highly fluctuated over time, representing by numerous peaks. After the hammers were given a rotational speed, the magnitude of the power increased rapidly to the maximum value. At that time, the hammers reached their constant speed and hit large amount of unbroken hemp segments, and therefore the highest power peak was observed. In some observation the power peak did not occur at the beginning because of the hammer had not been in contact with a large volume of particles immediately after it started rotating. While being continuously impacted by the hammers, hemp pieces became smaller and smaller. Some of those small pieces fell through the screen, resulting in less number of particles in the hammermill housing. As a result, fewer numbers of particles were being in contact with the hammers, the magnitudes of those peak powers were being reduced.

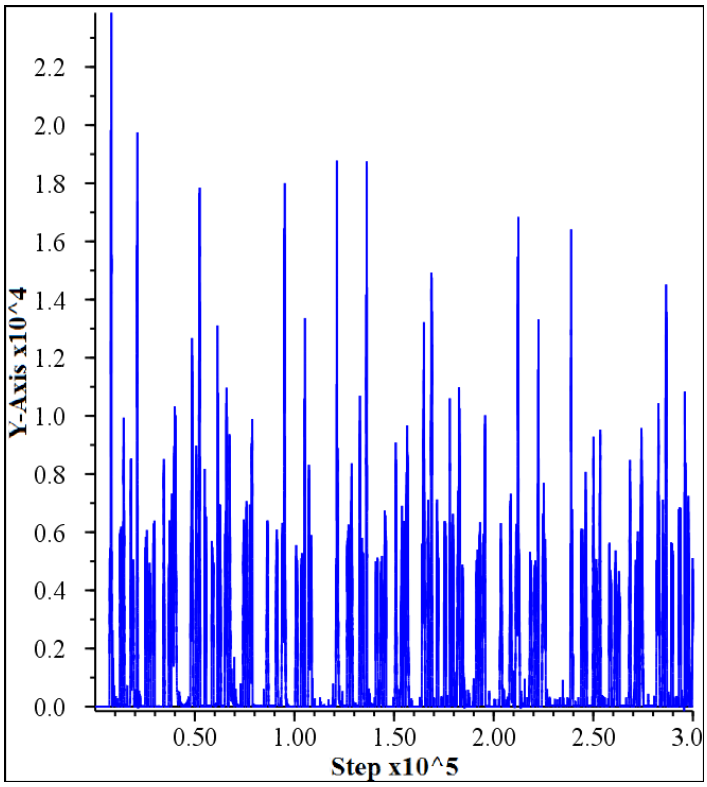

Fig. 5.9. Typical model output for the power of hammermill; X-axis: time step, Y-axis: power (W).

The maximum power shown in Fig. 5.9 was recorded for each of the feeding rates: 80, 130, and 260 g. The results showed that the power requirement increased with the increase of feed mass, especially at a higher rotational speed (Fig. 5.10). The power requirement also increased with the increase of the rotational speed. The maximum power for different feed masses ranged from 4.52-6.54 kW, 7.03-11.7 kW, and 22.6-30.1 kW for 1000, 2000, and 3000 rpm respectively. The power requirements for the 1000 and 2000 rpm were close at all the feed masses. However, for the 3000 rpm the power requirements were much higher, regardless of the feeding mass. The average power over

all scenarios was 13.57 kW. This was comparable with the power requirement (14.25 kW) reported by Baker (2009) for processing hemp with hammers rotating at 3600 rpm.

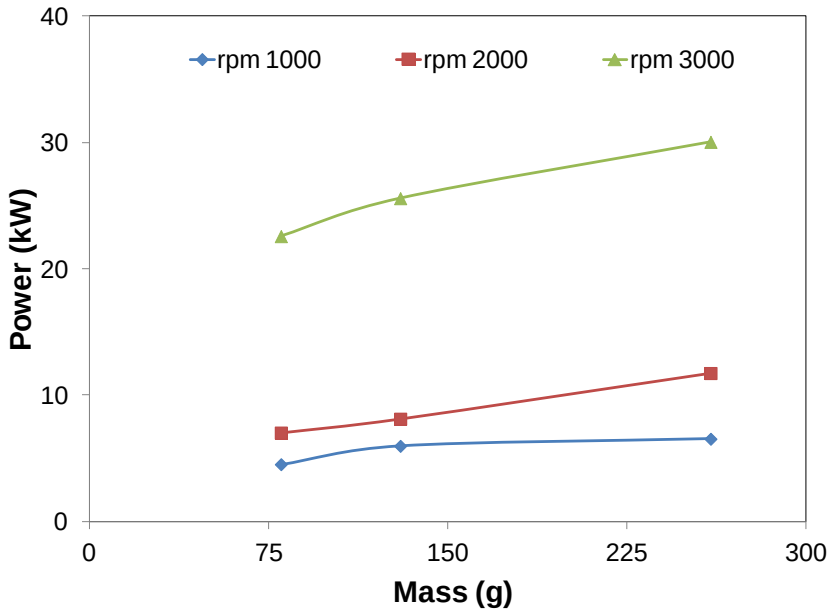

Fig. 5.10. Maximum power of the hammermill as affected by the feeding mass.

5.5.2.3. Kinetic energy of hemp particles

As the hammers started rotating, the kinetic energy of hemp particles increased rapidly. Within a short time, it reached the peak value. Then it decreased by approximately 50%, where, the kinetic energy fluctuated around a nearly constant value (Fig. 5.11). These reflected the different stages of hemp processing. The power increasing at the beginning represented for the stage of the increasing hammer rotational speed and accelerating of hemp particles. The peak kinetic energy implied that the maximum rotation speed of the hammers had been reached, and hemp particles fed in the hammermill housing were in a full motion. The following decreasing power meant that the hemp segments were being broken into pieces, and some of those pieces were being falling through the screen, while

the hammers rotated. Therefore, fewer and fewer numbers of particles in the hammermill housing contributed to the total kinetic energy.

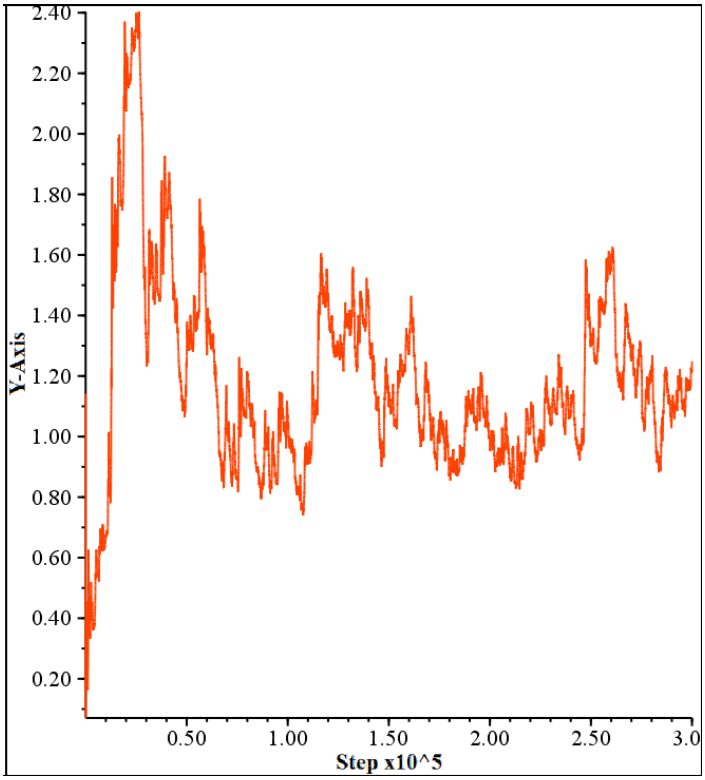

Fig. 5.11. Typical model output of kinetic energy; X-axis: time steps, Y-axis: kinetic energy (J).

The maximum kinetic energy was read from the energy-time curve shown in Fig. 5.11 for each simulation. The values of the maximum kinetic energy were then converted to the specific kinetic energies, expressed as the energy per unit weight of hemp material fed into the hammermill. The results showed that the overall specific kinetic energy ranged from 0.09 to 2.14 kW hr t^{-1} for all feed masses and rotational speeds (Fig. 5.12). The specific energy was increased with the increase of the feed mass. At the same feed mass,

the lower rotational speed generally resulted in lower specific kinetic energy. This could be explained by the fact that hemp stems were broken into smaller pieces at higher rotational speed; those small pieces passed through screen openings and did not contribute to the kinetic energy.

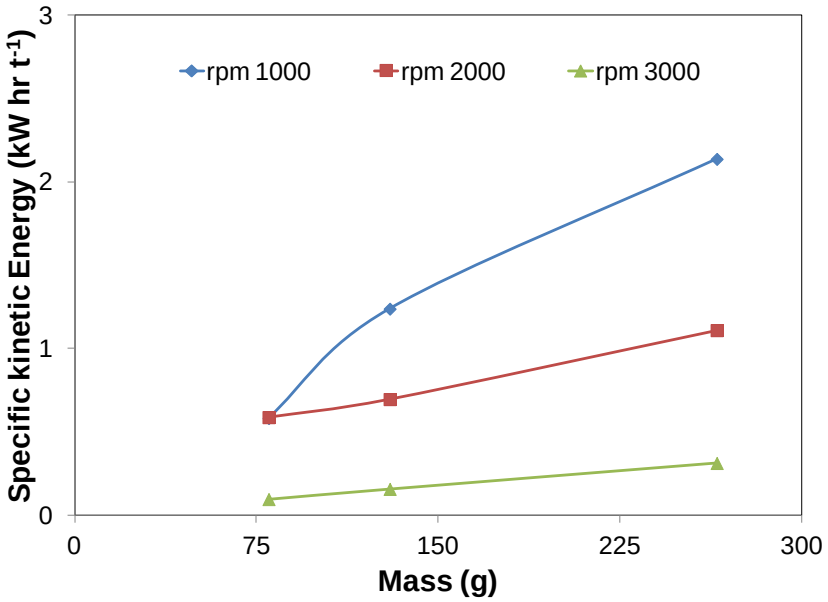

Fig. 5.12. Specific kinetic energy of hammermill as affected by the feed mass.

5.5.2.4. Strain energy of hemp particles

Strain energy develops within the contacts of particles. The simulated strain energy was the highest at the beginning, and reduced over time (Fig. 5.13). Before hemp segments were broken inside the hammermill, more hemp particles were in contact within the clusters, and therefore the total strain energy was higher. With time, more hemp segments were being broken, meaning the breakage of more bonds between particles within the clusters. Therefore, there would be less and less contacts among the particles. This explains the reduced trend of the total strain energy over time. Near the end of the

simulation, the strain energy was fluctuating around a constant value, indicating that the remaining bonds between hemp particles were not being further broken.

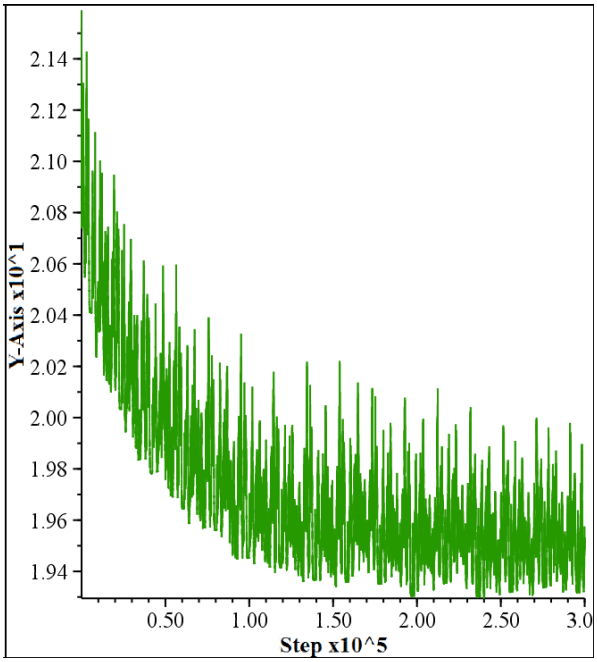

Fig. 5.13. Typical model output of strain energy; X-axis: time steps, Y-axis: strain energy (J).

The specific strain energy ranged from 1.93 to 8.68 kW hr t^{-1}, depending on the feed masse and rotational speed. Under each speed, the specific strain energy was linearly increased with the increase of the feed mass (Fig. 5.14). It was interesting to notice that the values of specific strain energy of the 2000 rpm were lower than that of the 1000 rpm at the same feed mass. This phenomenon could be attributable to the different failure pattern of the hemp clusters at different speeds as shown in Fig. 5.7.

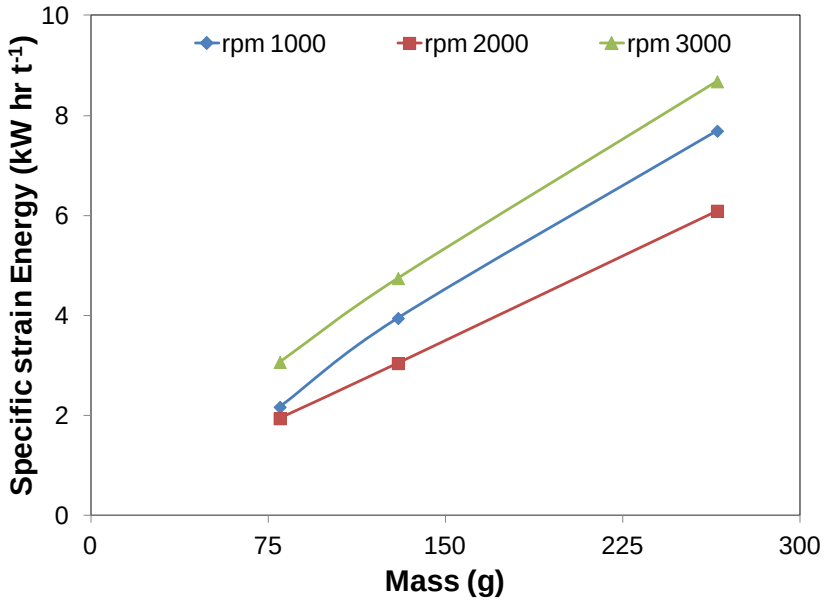

Fig. 5.14. Specific strain energy of particles as affected by the feed mass.

The strain energy was not only related to the number of particles which are in contact, but also related to the orientation of the particles. A cluster with the same number of particles could have different particle orientations, and therefore different numbers of contacts. Figure 5.15 illustrates that a four particle cluster can have three contacts (Fig. 5.15a), four contacts (Fig. 5.15b), or six contact (Fig. 5.15c), depending on the particle orientation. All contacts in Figs. 5.15a and 5.15b are within a same plane, while contacts in Fig. 5.15c are in different planes. It was speculate that the contacts of the particles for the 2000 rpm might be more like those shown in Figs. 5.15a and 5.15b. As the result, the specific strain energies were low at this speed.

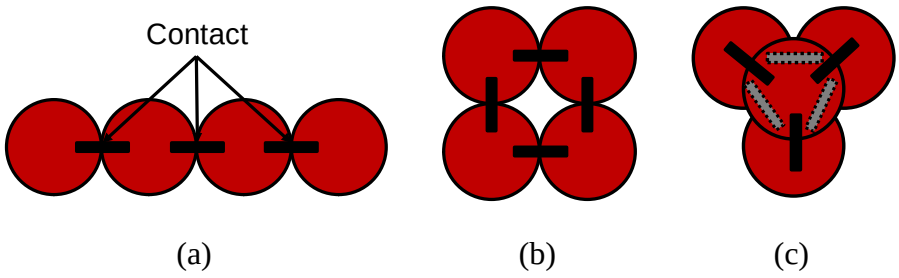

Fig. 5.15. Number of contacts for different particle orientations in a four-particle cluster.

5.6. CONCLUSION

PFC^{3D} has been successfully used for developing a model to simulate hemp processing using a hammermill. With PFC^{3D}, a virtual hemp stem can be formed using a cluster of balls and bonds. Calibration of particle microproperties can be achieved using virtual compression tests. The calibrated bond stiffness of hemp stem was 2.2×10^6 Pa with a relative error of 0.54% when compared to the literature data of hemp compression tests. The model was able to predict the power and energy distributions inside the hammermill under different feeding masses and hammer rotational speeds. The predicted values varied from 4.52 to 30.05 kW for the power requirement, from 0.09 to 2.14 kW hr t^{-1} for the specific kinetic energy, and from 1.93 to 8.68 kW hr t^{-1} for the specific strain energy, depending on the feed masse and rotational speed. In general, all these predicted variables were greater at higher feed mass, with the specific strain energy being the most sensitive variable to the feed mass. As for the effects of hammer rotational speed, an increasing trend was observed for the power requirement, a decreasing trend was observed for the specific kinetic energy, and a mix result was observed for the specific strain energy. Given the following observations: the much greater power requirement at the 3000 rpm than at the 2000 rpm, the decreasing trend of the kinetic energy, and the

lowest strain energy at the 2000 rpm, it is recommended to operate the hammermill at 2000 rpm. Further research is needed to verify the conclusion.

5.7. REFERENCES

Asaf, Z., D. Rubinstein and I. Shmulevich. 2007. Determination of discrete element model parameters required for soil tillage. *Soil and Tillage Research* 92(2): 227-242.

Baker, M. 2009. Evaluation of hammermill and planetary ball mill for hemp fibre decortications. Unpublished Masters Thesis. Winnipeg, MB: Department of Biosystems Engineering, University of Manitoba.

Cleary, P.W. 1998. Predicting charge motion, power draw, segregation, and wear and particle breakage in ball mills using discrete element methods. *Mineral Engineering* 11(11): 1061–1080.

Cleary, P.W. and D. Hoyer. 2000. Centrifugal mill charge motion and power draw: comparison of DEM predictions with experiment. *International Journal of Mineral Processing* 59: 131–148.

Coetzee, C.J. and D.N.J. Els. 2009. Calibration of discrete element parameters and the modelling of silo discharge and bucket filling. *Computers and Electronics in Agriculture* 65:198–212.

Cundall, P.A. and O.D.L. Strack. 1979. A discrete numerical model for granular assemblies. *Geotechnique* 29: 47-65.

Djordjevic, N. 2003. Discrete element modeling of the influence of lifters on powder draw of tumbling mills. *Minerals Engineering* 16: 331-336.

Djordjevic, N., F.N. Shi and R.D. Morrison. 2003. Applying discrete element modelling to vertical and horizontal shaft impact crushers. *Minerals Engineering* 16: 983–991.

Franco, Y., D. Rubinstein and I. Shmulevich. 2007. Prediction of soil-bulldozer blade interaction using discrete element method. *Transactions of the ASABE* 50(2): 345-353.

Inoue, T. and K. Okaya. 1996. Grinding mechanism of centrifugal mills - a simulation study based on the discrete element method. *International Journal of Mineral Processing* 44–45: 425–435.

Itasca. 2008. PFC^{3D} particle flow code in 3 dimensions, theory and background. Itasca Consulting Group, Inc. Minneapolis, Minnesota, USA.

Khan M.R., Y. Chen, C. Lague, H. Landry, Q. Peng and W. Zhong. 2010. Compressive properties of Hemp (Cannabis sativa L.) stalks. *Biosystems Engineering* 106: 315 - 323.

Landry, H., C. Laguë and M. Roberge. 2006a. Discrete element representation of manure products. *Computers and Electronics in Agriculture* 51: 17-34.

Landry, H., F. Thirion, C. Laguë and M. Roberge. 2006b. Numerical modeling of the flow of organic fertilizers in land application equipment. *Computers and Electronics in Agriculture* 51: 35-53.

Lopo, P. 2002. The right grinding solution for you: roll, horizontal or vertical. *Feed Management* 53(3): 23-26.

Lu, Z., S.C. Negi and J.C. Jofriet. 1997. A numerical model for flow of granular materials in silos. Part 1: model development. *Journal of Agricultural Engineering Research* 68: 223-229.

Mak, J., Y. Chen and M.A. Sadek. 2012. Determining parameters of a discrete element model for soil–tool interaction. *Soil and Tillage Research* 118: 117–122.

Mani, S., L.G. Tabil and S. Sokhansanj. 2004. Grinding performance and physical properties of wheat and barley straws, corn stover and switchgrass. *Biomass and Bioenergy* 27: 339 – 352.

McDowell, G.R. and O. Harireche. 2002. Discrete element modelling of yielding and normal compression of sand. *Géotechnique* 52(4): 299-304.

Miao, Z., T.E. Grift, A.C. Hansena and K.C. Ting. 2011. Energy requirement for comminution of biomass in relation to particle physical properties. *Industrial Crops and Products* 33: 504–513.

Mishra, B.K. and C.V.R. Murty. 2001. On the determination of contact parameters for realistic DEM simulations of ball mills. *Powder Technology* 115: 290-297.

Ni, Q., W. Powrie, X. Zhang and R. Harkness. 2000. Effect of particle properties on soil behaviour: 3-D numerical modeling of shearbox tests. In *Numerical Methods in Geotechnical Engineering (GSP 96)*, 58-70. Reston, Va.: ASCE.

Pierce, M.E. 2004. PFC^{3D} modeling of inter-particle percolation in caved rock under draw. Numerical modeling in micromechanics via particle methods. 1(6): 149-156.

Potyondy, D.O. and P.A. Cundall. 2004. A bonded-particle model for rock. *International Journal of Rock Mechanics and Mining Sciences* 41(8): 1329-1364.

Rajamani, R.K., B.K. Mishra, R. Venugopal and A. Datta. 2000. Discrete element analysis of tumbling mills. *Powder Technology* 109: 105–112.

Sadek, M. A., Y. Chen and J. Liu. 2011a. Simulating shear behavior of a sandy soil under different soil conditions. *Journal of Terramechanics* 48: 451–458.

Sadek, M. A., Y. Chen, C. Laguë, H. Landry, Q. Peng and W. Zhong. 2011b. Characterization of the shear properties of hemp using discrete element method. *Transaction of ASABE* 54(6): 2279-2285.

Sakaguchi, F., M. Suzuki, J.F. Favier and S. Kawakami. 2001. Numerical simulation of the shaking separation of paddy and brown rice using the discrete element method. *Journal of Agricultural Engineering Research* 79(3): 307-315.

Savoie, P., D. Trebly, R. Theriault. J.M. Wauthy and C. Vigneault. 1989. Forage chopping energy vs. length of cut. *Transactions of ASAE* 32(2): 437-442.

Shi, F., T. Kojovic, J. S. Esterle and D. David. 2003. An energy-based model for swing hammermills. *International Journal of Mineral Processing* 71: 147 -166.

Van der Linde, J. 2007. Discrete element modeling of a vibratory subsoiler. Unpublished Maters thesis. Matieland, South Africa: Department of Mechanical and Mechatronic Engineering, University of Stellenbosch.

van Nierop, M.A., G. Glover, A.L. Hinde and M.H. Moys. 2001. A discrete element method investigation of the charge motion and power draw of an experimental two-dimensional mill. *International Journal of Mineral Processing* 61: 77–92.

Vigneault, C.T., T.M. Rothwell and G. Bougeois. 1992. Hammermill grinding rate and energy requirement for thin and conventional hammers. *Canadian Agricultural Engineering* 34(2): 203-206.

Yu, M., A. R. Womac, P.I. Miu, C. Igathinathane, S. Sokhansanj and S. Narayan. 2006. Direct Energy Measurement Systems for Rotary Biomass Grinder – Hammermill. ASABE Paper no. 066217. St. Joseph, MI: ASAE.

Chapter 6

Discrete Element Modeling of Hemp Particle Separation using a 3D Vibratory Separator

6.1. SIGNIFICANCE

Having studied the physical properties of the hemp materials and established the PFC^{3D} model microproperties, the final step was to investigate how hemp material behaves when interacting with a machine system, a 3D vibratory separator specifically. A numerical model was developed using the discrete element method (DEM) to simulate the separation process using the 3D separator. The model allows for determining the separation efficiency of any compositions of hemp fibre, core, and chaff. The model also allows for studying many other dynamic behaviours of hemp material during the separating process, such as particle movement, velocity, and contact regime with the separator. However, these will be included in the future work. This chapter corresponds to the objective 4 of the thesis.

6.2. ABSTRACT

Existing cleaning equipment was ineffective for cleaning processed hemp material. One of the major obstacles was the lack of the knowledge on the interactions between hemp material and the equipment. In this study, a 3D vibratory separator (screen-type) was experimentally studied for separating processed hemp to remove the chaff (small particles). In the experiment, the separation efficiency of the 3D vibratory separator was

measured for different horizontal and vertical vibratory forces. Results showed that the separation efficiency varied from 23 to 86%, depending on the vibratory forces. This low separation efficiency was due to the fibre entanglement which prevented small particles from passing through the screen. A numerical model was developed to simulate the 3D vibratory separator using the discrete element method (DEM). The main model components included virtual particles of fibres and cores as well as a virtual 3D vibratory separator. The model is able to predict the separation efficiency of the vibratory separator for mixtures of various particles and found the ratio of the small and large particle into the mixture and the separation duration was critical for serration performance. When compared to the test results, the simulated separation efficiency was higher, because there was no entanglement problem with the virtual hemp particles.

6.3. INTRODUCTION

Because of the diverse use of natural fibre, current demands for hemp fibre are increasing. Obtaining high quality hemp fibre requires several processing steps from the field to the final product. Separation of processed hemp is one of the major steps to obtain clean fibre. Processed hemp consists of core, also named as hurds (the inner layer of hemp stem), fibre (the outer layer), and chaff. The ultimate goal is to completely separate the core and chaff from the fibre to obtain clean fibre. This ultimate goal is typically achieved in several stages. The first stage is to remove the chaff which has less market value than fibre or core. Chaff particles can be either fibre or cores, but small in size. Separation of those small particles from processed hemp material was the first step in the fibre cleaning process, which was the focus of this study.

As no cleaning machines have been designed specifically for separating hemp material, people adopted cleaning equipment from other applications, such as screen type machines (Hempel 2000). In some industrial applications, processed hemp was fed into a multiple ultra cleaner to eliminate short fibres and cores from the long fibres (Münder et al. 2004). Straw walkers from combine were also used for cleaning fibres (Gratton and Chen 2004). Among all those methods, the screening method is more versatile and capable of handling large amount of feed. However, little research has been done in the past to investigate the efficiency of the screening method for separations of processed hemp.

One of the common screening machines is vibratory separator (Nye and Ling 2008). In this study, a 3D vibratory separator was investigated using both experimental and modeling approaches. For the modeling, the discrete element method (DEM) was used to simulate the separation process of processed hemp material in the 3D vibratory separator. The DEM is a numerical approach to simulate material as discrete assemblages of particles. The DEM was first introduced by Cundall and Strack (1979) for analyzing geological materials (rocks and soils). Recently, the DEM has been applied to many other biomaterials including grains (Lu et al. 1997; Sakaguchi et al. 2001), biofibre (Sadek et al. 2011), and manure (Landry et al. 2006a; Landry et al. 2006b). The DEM has become a promising tool to simulate bulk behaviours of a material through their constituent of individual particles.

Particle Flow Code in Three Dimension (PFC^{3D}) was a widely used commercial DEM software. It was developed by Itasca Consulting Group, Inc., Minneapolis, MN (Itasca 2008). In PFC^{3D}, material to be simulated is represented by assemblies of individual particles. The basic particles are "balls". The "surrounding environment" in which the material is placed, such as boundaries and machine surfaces, is simulated by "walls". PFC^{3D} allows users to model material particles with any arbitrary shapes by attaching a group of balls together using the PFC^{3D} bond models. These features allow for effective simulations of the irregular shapes of hemp fibre and cores as well as their interactions with the separator.

The objective of this study was to investigate the performance of a 3D vibratory separator for cleaning processed hemp. The specific objectives were

a. to measure the separation efficiency for separating hemp particles under different operating conditions;
b. to develop a model to simulate the separation process using PFC^{3D};
c. to use the model to predict the separation efficiency for hemp mixtures with various compositions.

6.4. METHODOLOGY

6.4.1. Hemp Separation Experiment

6.4.1.1. Feedstock used for the separation experiment

The feedstock used for the separation experiment was processed hemp material collected from a hemp processing plant in Manitoba, Canada. The feedstock contained fibre, cores, and chaff as shown in Fig. 6.1. Detail compositions of the feedstock are described later in this paper.

Fig. 6.1. Processed hemp material used for the separation experiment.

6.4.1.2. The 3D vibratory separator

A 3D vibratory separator, named SWECO (Vibro Energy Separator - XS40, SWECO Canada, Inc., ON, Canada) was used for the fibre separation tests (Fig. 6.2). The separator had several screen decks and a vibration motion generator. The screen decks were replaceable with any desired opening size of screen. In the experiment, only one deck was used and it had 20 mm screen opening size. This size appeared to be the

common length used to differentiate final fibre product and chaff (Munder and Hempel 2004). The motion generator consisted of a motor with eccentric weights on the top and the bottom of the motor. Top weight generated the horizontal motion and the bottom weight generates the vertical motion. Both horizontal and vertical vibration magnitudes could be adjusted through the weight settings. Each setting corresponded to a centrifugal force specified by the manufacturer of the separator. In addition to those settings, the separator could also be run at different lead angles, relative positions of the top and bottom weights. The lead angle was the measure of the delay between the vertical and horizontal amplitudes, and it affected the pattern of material flow on the screen. In the experiment, the lead angle was fixed at 35° based on the recommendation from the manufacturer for dry material separation. This lead angle produced a spiral flow pattern (material flows outwards from the centre to the periphery). The horizontal and vertical vibration amplitudes were read from the gauge stickers on the machine when the machine is in operation.

Fig. 6.2. The 3D vibratory separator used in the separation experiment.

6.4.1.3. Experimental design

The separation efficiency of the separator was tested for the 20 mm screen opening size under different horizontal and vertical vibration forces of the separator. Under each vibration direction, three levels of centrifugal force were selected, and they were the highest, lowest, and the recommended level by the manufacturer. Their corresponding centrifugal forces (Sweco 2003) are listed in Table 6.1. A total of 36 tests (3 horizontal forces x 3 vertical forces x 4 replications) were performed. The tests were completed in a completely random order.

Table 6.1. Summary of the treatments

Vibration direction	Force setting	Centrifugal force (N)*
Horizontal	H1	13367
	H2	9920
	H3	2678
Vertical	V1	1174
	V2	4346
	V3	5858

*Specified by Sweco (2003)

6.4.1.4. Hemp sample preparation

The processed hemp material shown in Fig. 6.1 was used for the separation tests. Samples for the experiment were prepared by collecting bunches of the material from random locations of the feedstock in a large container. Each bunch of the material removed from the container was assigned a number value of one to forty using a random number generator which was corresponded to a treatment condition. Thirty six samples

were used for the separation tests and four samples were used for analyzing the feedstock compositions. Each sample weighed 100 g.

6.4.1.5. Measurement of initial compositions of the feedstock

The feedstock was a mixture of fibre, core, and chaff. The compositions of the mixture were quantified using four samples. The compositions of the feedstock were classified based on the screen opening size, 20 mm. Each sample was separated manually into the following four different fractions (Fig. 6.3), and the weight of the fraction was recorded to determine the percentage in the mixture as the followings:

a) *Fibre (m_f),* fibres longer than 20 mm;
b) *Fibre bound to core (m_{cf})* (core and fibre still attached together), combined length longer than 20 mm;
c) *Core (m_c),* cores longer than 20 mm;
d) *Chaff (m_{ch}),* fibres and cores equal to and shorter than 20 mm.

(a) (b)

(c) (d)

Fig. 6.3. Different fractions of the feedstock; (a) fibre, (b) fibre bound to core, (c) core, (d) chaff.

6.4.1.6. Definition of separation efficiency

In particulate solids analyses, the mass of material which is capable of passing a screen is often determined based on the linear dimension of particle and the screen size. When the particle size is smaller than the screen opening size, the particle is considered to be capable of passing. The separation efficiency is defined as the mass of material which passes the screen divided by that mass of the material which is capable of passing (Richardson et al. 2002). In this study, among the different fractions of the feedstock, the

fractions, m_{ch} was considered capable of passing the 20 mm screen, and the rest factions would remain on the top of the screen. Therefore, the separation efficiency was determined as

$$\eta = \frac{m_p}{m_{ch}} \times 100 \tag{6.1}$$

where

η = separation efficiency (%),

m_p = mass of the material which actually passed through the screen (g),

m_{ch} = mass of the chaffs present in the mixture (g).

6.4.1.7. Experimental procedure

Before each test run, the vibration of the separator was set to the desire horizontal and vertical forces. The feedstock sample was manually fed on the deck through the central opening of a lid on top of the screen deck. Then, the vibration commenced, and continued for 3 minutes. During the operation, the vibration amplitude was recorded. At the end of the run, the portion of the material passed the screen and the remaining portion on the screen were collected. The mass of each portion was recorded to determine the separation efficiency.

6.4.1.8. Data analysis

Data were analyzed using SAS 9.1.3. The experimental parameters were arranged into two factor factorial design. Scheffe's test was used to determine the differences among least square means. A significance level of 0.05 was applied to all the analysis.

6.4.2. Simulation of the 3D Vibratory Separator

6.4.2.1. Virtual fibre and core

Virtual fibre and core were defined based on the characteristics of the real fibre and cores. Although the shapes of real fibre and cores are irregular, a fibre has a string-like shape, and a core is close to a rectangular. Thus, a string shaped fibre and a rectangular shaped core were defined using the cluster logic of PFC^{3D} (Fig. 6.4). A cluster consists of a series of balls which are connected with the parallel bonds implemented in PFC^{3D}. The bonds provide some strength to the structure of the cluster.

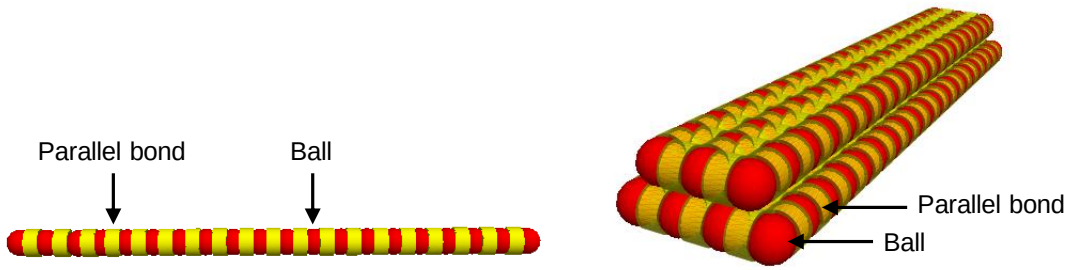

(a) (b)

Fig. 6.4. (a) Virtual fibre, (b) virtual core.

All balls in a virtual fibre cluster have the same diameter which was set as the diameter of the fibre to be simulated. The number of balls in a virtual fibre can be determined based on the fibre length using the following equation

$$n_f = l/D + 1 \tag{6.2}$$

where

n_f = number of balls in a virtual fibre bundle,

D = diameter of ball, equal to the diameter of fibre (mm),

l = length of fibre (mm).

As a core is a broken piece of hemp stem which is of circular shape originally, the shape of core is also curved in one direction. Such a shape was approximated by a cluster of two layers of balls, with one layer being larger than the other (Fig. 6.4b). The diameter of the balls was set to be half of the core thickness. The total number of balls required for the cluster of a virtual core depends on the width and length of the core as follows:

$$n_c = \frac{b_{c1} l_{c1} + b_{c2} l_{c2}}{D_c^2} \tag{6.3}$$

where

n_c = number of particles in a virtual core

D_c = diameter of ball (mm)

b_{c1}, b_{c2} = width of the bottom and top layer of core (mm)

l_{c1}, l_{c2} = length the bottom and top layer of core (mm)

6.4.2.2. Model microproperty

In PFC^{3D}, the virtual fibre and core described above are defined by a set of ball and bond microproperties. The ball microproperties include normal stiffness (K_n), shear stiffness (K_s), and friction coefficient (μ), and the bond microproperties include normal and shear stiffness ($\bar{k}^n$ and $\bar{k}^s$), normal and shear strength (σ_c and τ_c), and the radius of the

cylindrical bond (*R*). The microproperties of the hemp fibre and core were taken from the previous values. The ball microproperties are described in Chapter 3 and the bond microproperties are described in Chapter 5. The microproperties are summarised in Table 6.2.

Table 6.2. Model microproperties

	Value	
Ball microproperty	**Fibre**	**Core**
Normal stiffness (K_n), N m^{-1}	5x10^4	8x10^4
Shear stiffness (K_s), N m^{-1}	5x10^4	8x10^4
Friction (μ)	1.0	1.0
Bond Microproperty		
Normal stiffness ($\bar{k}^n$), Pa m^{-1}	1x10^{14}	2.5x10^9
Shear stiffness ($\bar{k}^s$), Pa m^{-1}	1x10^{14}	2.5x10^9
Normal strength (σ_c), Pa	3.58x10^8	2.2x10^6
Shear strength (τ_c), Pa	3.58x10^8	2.2x10^6
Bond radius (R)	Equal to the ball radius	

6.4.2.3. Virtual separator

The virtual separator was constructed using the PFC^{3D} wall logic (Fig. 6.5). A cylindrical wall was used to construct the main body of the separator. The screen was formed using 3D lines through intersecting the 3D lines with an equal spacing of 20 mm. The screen was placed at the two-third height of the main body from the bottom. A rectangular base was constructed at the bottom of the main body to function as the collecting pan of the separator.

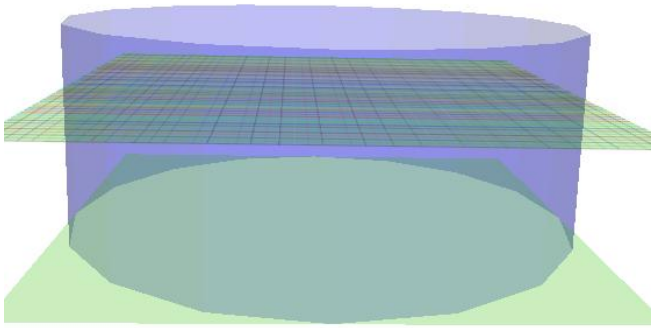

Fig. 6.5. Virtual 3D vibratory separator.

6.4.2.4. Motion of the virtual separator

The horizontal and vertical motion of the virtual separator was set the same as the real 3D separator. The motion was calculated using the angular frequency (ω) and vibration amplitude (A) of the separator. Angular frequency (ω) was derived from the rational speed of the motor (1200 rpm) and the amplitude was measured from the real 3D separator. The vibrating function is expressed by

$$v_x = A \cos(\omega t) \tag{6.4}$$

$$v_y = A \cos(\omega t) \tag{6.5}$$

$$v_z = A \sin(\omega t + \varphi) \tag{6.6}$$

where

v_x, v_y and v_z = translational velocities of the virtual separator in x, y and z directions, respectively (m/s),

A = vibration amplitude (m),

ω = angular frequency (radian),

φ = lead angle (radian),

t = time (s).

6.4.2.5. Generation of a virtual mixture of processed hemp

To simulate the separation process, a mixture of fibres, cores, and chaff needs to be generated in the virtual separator. In PFC^{3D}, it is difficult to directly generate clusters which were used to define virtual fibres and cores. Therefore, several steps were followed in the generation process. The first step was to generate the desired number of balls on the top of the screen at the centre of the virtual separator. The second step was to replace each of those balls by a clump. The clump template was made of the same dimension as the cluster of a virtual hemp fibre or a virtual core. The third step was to change the clump to a cluster through "releasing" the balls within the clump without changing the shape of the template. To generate desired compositions of fibre and core in the mixture, the generated balls in the first step were assigned to a group name (eg. "fibre" and "core"). Thus, each group of balls could be replaced accordingly by a group of virtual fibres or a group of virtual cores. The ratio of the two groups could be adjusted as desired. The sizes of each cluster and size distributions within the groups could also be

varied as desired. The sizes of the chaff were set to be smaller than the screen opening size, 20 mm in the particular case of this study.

6.4.3. Testing of the Model Behaviour

Before the simulations of the separation process, the model was tested to examine if particles would follow the expected motion pattern. For this purpose, a single virtual fibre was generated at the centre of the screen (Fig. 6.6a). After the vibratory motion was introduced, a spiral motion of the fibre was observed. The stationary fibre started moving outwards (Fig. 6.6b), then touching the periphery (Fig. 6.6c), and finally traveling along the periphery (Fig. 6.6d). This motion pattern was similar to that described by the supplier of the real separator for the 35^{o} lead angle.

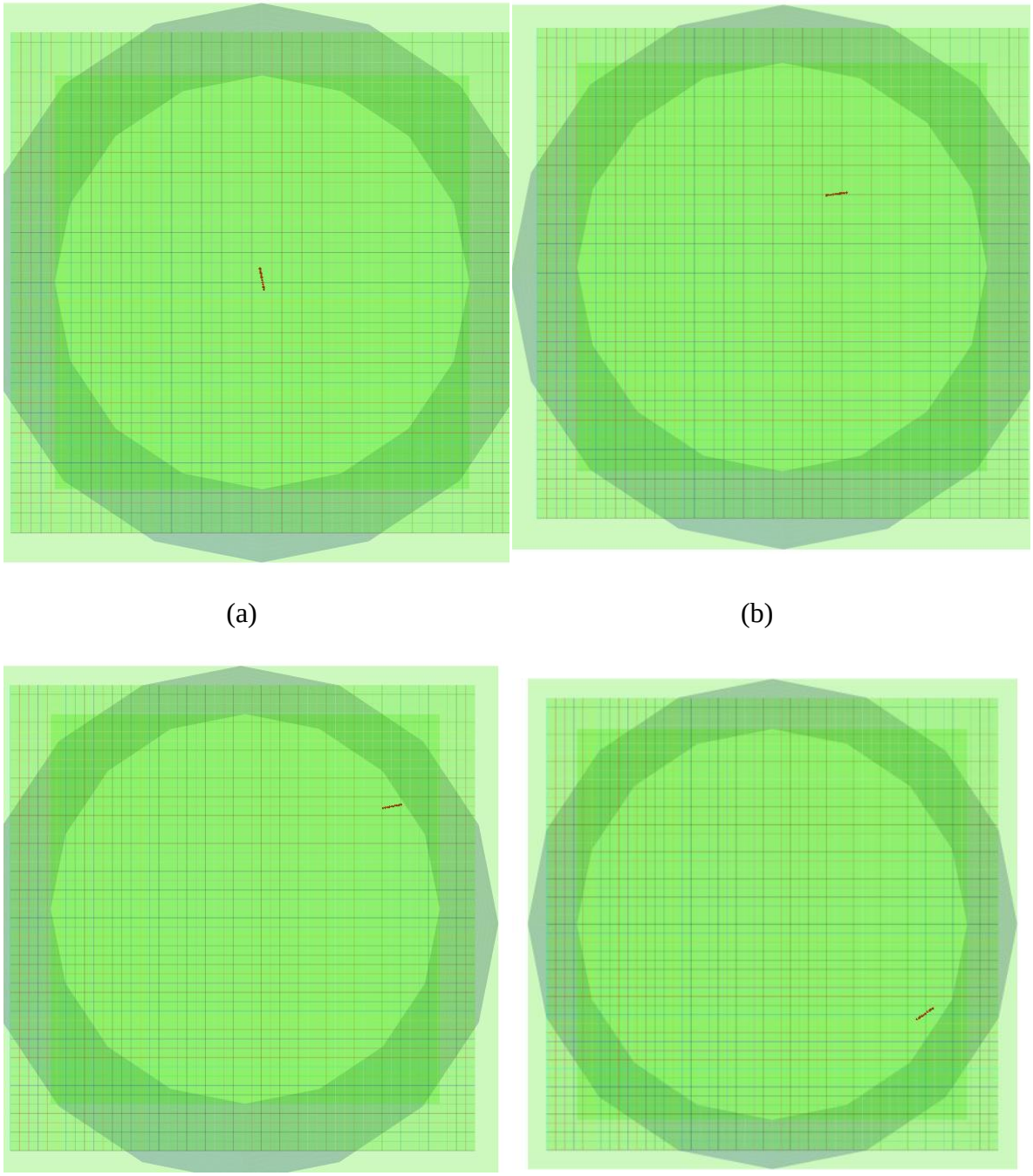

(a) (b)

(c) (d)

Fig. 6.6: Screenshots of the motion of a single particle at different simulation times.

6.4.4. Simulation of the Separation Process

6.4.4.1. Virtual mixtures of hemp material

As described above, the feedstock was a mixture of fibre, core, fibre bound to core, and chaff. In PFC^{3D}, it was difficult to form the faction of fibre bound to core. Thus the mixture was assumed to be included only virtual fibre, core, and chaff. The faction of fibre bound to core was split equally into the fibre and core fractions. For fibre, a constant diameter of 0.30 mm was used which was presented in Chapter 4. For core, the thickness and the width of all hemp cores were 4 mm (Khan et al. 2010) and 10 mm respectively. The lengths of fibre and core were varied within the mixture. Some of them had sizes greater than 20 mm, and some had sizes smaller than 20 mm. Those particles smaller than 20 mm were considered as chaff.

The six different particles (Table 6.3) were formed and they were used to make the mixtures for the separation simulations. The Fibre A was longer than the Fibre B, and both were greater than the screen opening size of the separator. Similarly, the Core A was longer than the Core B, and both were greater than the screen opening size. The Fibre Chaff and Core Chaff were set to the lengths smaller than the screen opening size. The dimensions of the different compositions are listed in Table 6.3

Table 6.3. Different particles for virtual mixtures of hemp material

Particle	**Dimension, mm**
Fibre A	60x0.30 (Length x Diameter)
Fibre B	30x0.30 (Length x Diameter)
Fibre chaff	10x0.30 (Length x Diameter) and balls (0.3-2.0 mm diameter)
Core A	50x10x4 (Length x Width x Thickness)
Core B	25x10x4(Length x Width x Thickness)
Core chaff	10x10x4 (Length x Width x Thickness) and balls (0.3-2.0 mm diameter)

Simulations of the separation efficiency could be conducted for a mixture of the six particles listed in (Table 6.3). Figure 6.7a shows a mixture in the virtual separator before the separation process starts. The mixture is generated at the centre of the virtual separator. Enlarged top view of the mixture (Fig. 6.7b) illustrates that the fibre and core clusters are well mixed in the mixture and their orientations are random in nature, representing a real situation.

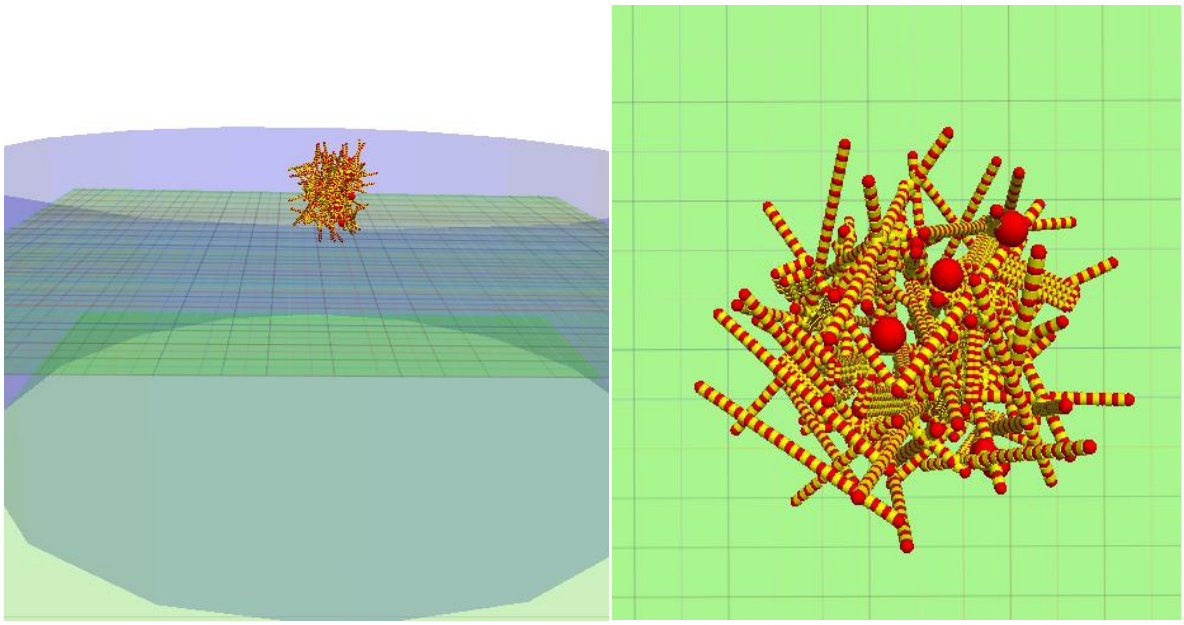

(a) (b)

Fig. 6.7. A particle mixture on the screen; a) side view, b) enlarged top view.

6.4.4.2. Vibration motion for the simulations

In the simulation, the virtual separator was operated only at one condition which was the optimal vibration condition found during the tests. The horizontal and vertical motions of the virtual separator was calculated using the Eq. 6.4, 6.5 and 6.6. Its cyclic motion is demonstrated in Fig. 6.8. The magnitude was derived from the displacement amplitude of the 3D separator, and in this case it was 3.9 mm for both horizontal and vertical direction. The first curve in Fig. 6.8 represents the vibration in both X and Y directions (horizontal) and the second curve represents for Z direction (vertical). The phase difference between the horizontal and vertical directions was the lead angle. All simulation lasted for three minutes as in the tests. During the course of simulation, the masses of particles above and below the screen were recorded using the PFC^{3D} fish function to determine the separation efficiency.

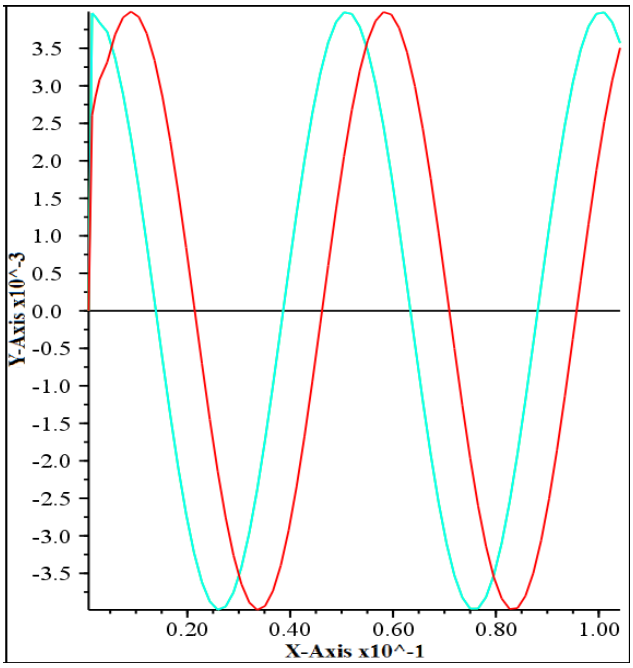

Fig. 6.8. Vibratory motion of the virtual separator; the first curve is the motion in the x and y directions and the second curve is the motion in the z direction. X-axis: duration (min), Y-axis: vibration amplitude.

6.5. RESULTS AND DISCUSSION

6.5.1. RESULTS FROM THE SEPARATION TESTS

6.5.1.1. Composition of the feedstock

Different fractions in the processed hemp material are presented in Fig. 6.9 as the percentage of the mass over the total mass. The largest fraction was the fibre which accounted for 48% of total mass, and only 3.5% of the total mass was cores. The remaining were fibre bound to core (23.45%) and chaff (25.35%).

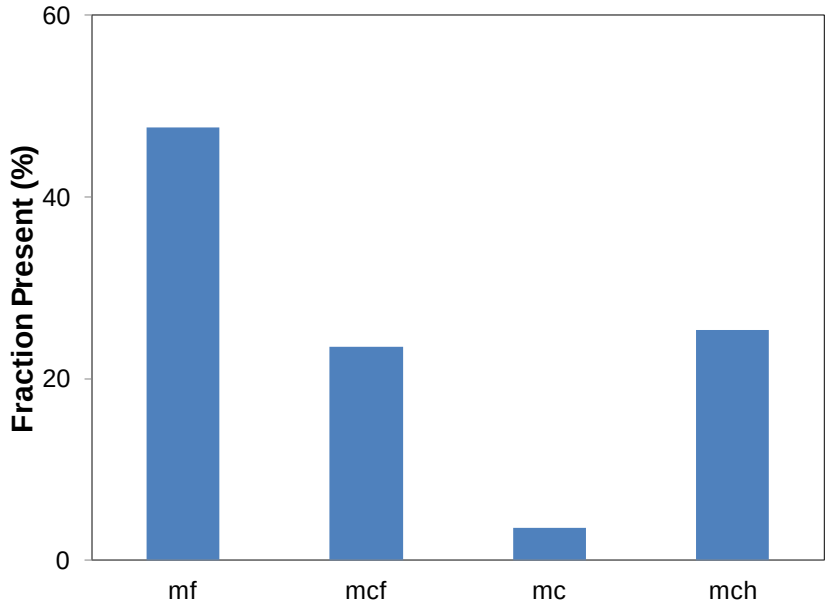

Fig. 6.9. Percentage of different fractions in feedstock. m_f = fibre fraction; m_{cf} = fibre bound to core fraction; m_c= core fraction; and m_{ch} = chaff fraction in the feedstock.

6.5.1.2. Measured separation efficiency

Separation efficiency was determined for all test runs using Eq. 6.1 and the efficiency data were statistically analyzed. The statistical analysis showed that the experimental factors, horizontal vibration force and its interaction with the vertical vibration force, significantly affected the separation efficiency (Table 6.4), whereas the vertical vibration force did not significantly affect the efficiency. Therefore, the simple effects of the experimental factors are presented due to the significance of their interactions.

Table 6.4. ANOVA results on the effects of experimental factors

Source	**df**	**MS**	**F**	**P**
Horizontal	2	6304.66	67.79	<0.0001
Vertical	2	92.52	0.99	0.3829
Horizontal*Vertical	4	590.67	6.35	0.001
Error	27	92.99		

The separation efficiency of the separator was highly variable, from 23.4 to 86.2%. (Fig. 6.10). Overall, the efficiency of the 3D separator was lower. Some chaff may have been trapped in the tangled fibres, which prevented them from passing through the screen. As for the treatment effects, the separation efficiency was increased by increasing the horizontal force for all levels of vertical vibration force, implying that the higher horizontal vibration force could reduce fibre entangling effects. There was no clear trend of the efficiency while changing the vertical vibration force. The highest separation efficiency, 86.2%, was observed when using force setting H1V2, followed by the combination of H1V3. The lowest efficiency, 23.4%, was obtained when using the V2H3 combination.

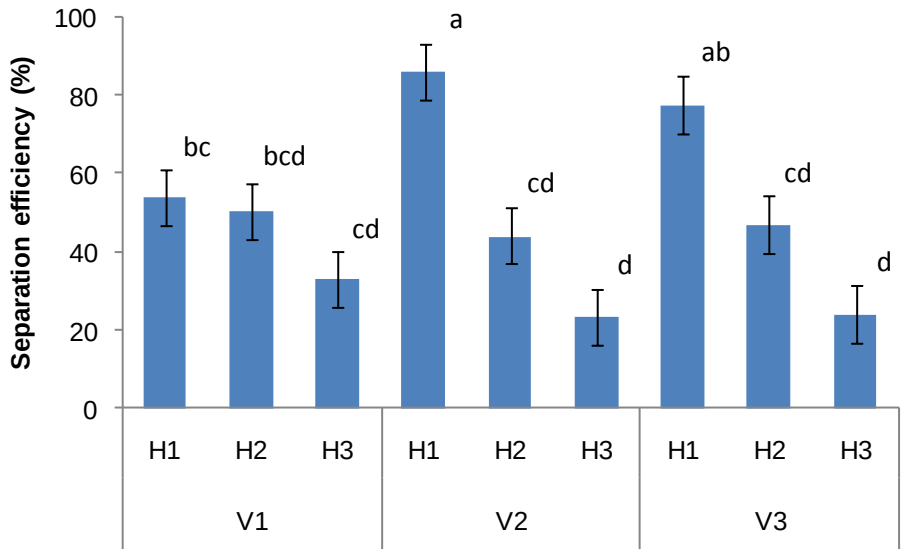

Fig. 6.10. Effect of vibration forces on the separation efficiency of the 3D vibratory separator. H1, H2, H3 = levels of horizontal force, V1, V2, V3 = levels of vertical force. Means followed with different letters are significantly different; error bars stand for standard errors.

6.5.2. Results from the Simulation

6.5.2.1. Selection of the particle mixtures

Simulations of the separation efficiency were conducted for three different mixtures of the hemp material (Table 6.5). All mixtures have a total weight of 100 g. The Mixture 1 was composed of particles similar to the feedstock used in the tests, so that the simulation results from this mixture could be compared with the test results. The Mixture 2 and Mixture 3 were arbitrarily formed. The Mixture 2 was composed of more long fibres and less chaff and Mixture 3 was composed of less long fibre and more chaff. These two

mixtures were used to further investigate whether the separation efficiency was affected by the different particle compositions.

Table 6.5. Percentages of virtual fibres, cores, and chaff in the virtual mixture of hemp material

	Percentage		
Particle	**Mixture 1**	**Mixture 2**	**Mixture 3**
Fibre A	48, Equal to m_f	58	38
Fibre B	11, Half of the m_{cf}	11	11
Fibre chaff	13, Half of the m_{ch}	8	18
Core A	4, Equal to m_c	4	4
Core B	11, Half of the m_{cf}	11	11
Core chaff	13, Half of the m_{ch}	8	18

m_f = fibre fraction; m_{cf} = fibre bound to core fraction; m_c= core fraction and m_{ch} = chaff fraction in the feedstock

6.5.2.2. Model behaviours

As in the real tests, small particles fell through the virtual screen, as illustrated by a snapshot of the simulation in Fig. 6.11. It was observed that most particles on the screen have sliding motion during simulation, while some particles were "jumping" on the screen. The jumping particles may orientate in the vertical direction, which would result in them falling through the screen, even though their lengths were greater than the screen opening sizes. This phenomenon was also observed in the real separation tests. During simulation there was no entanglement of the fibres thus there was high possibility of passing long particles passed through the screen depending on the duration of screening. This may lead the separation efficiency higher than the 100 percent. Hence the separation

efficiency will not be the appropriate term to analysis the effectiveness of virtual the 3D vibratory shaker. For the simulation results the effectiveness has described as separation performance.

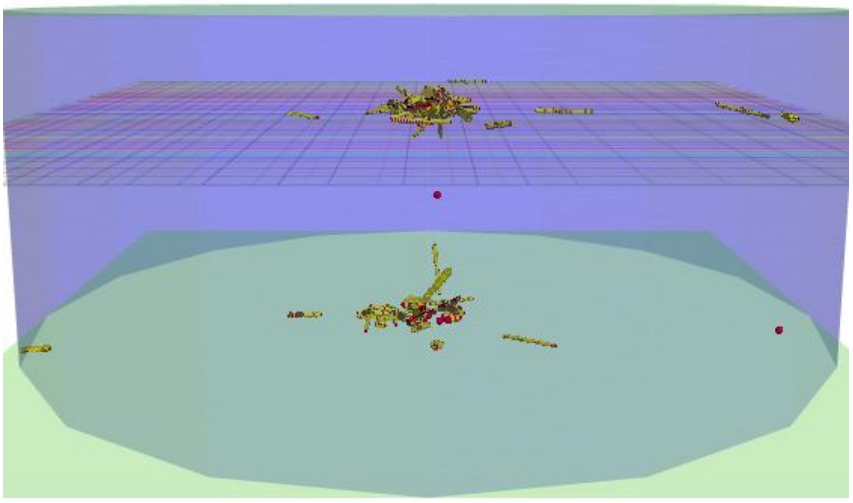

Fig. 6.11. A snapshot of virtual separation simulation.

6.5.2.3. Separation performance

Mixture 1 This mixture had similar compositions as the feedstock used for the separation tests. During the simulation, the percentage of the particle mass which passed through the screen over the total mass was monitored during the simulation. The results showed a slow increase in the percentage at the beginning and then a faster increase (Fig. 6.12). After 3 minutes, a total of 33% of particles (in mass) passed through the screen. If using the same theory as in the experiment, the simulated separation efficiency would be 100%. This was much higher than the experimental result (86.2%). The explanation was that there would be no fibre entanglement in the virtual mixture. As the result, all Fibre Chaff and Core Chaff would pass through the screen, which would give a 100% of

separation efficiency. The other 30% of particles which passed through the screen could be those “jumping” long particles.

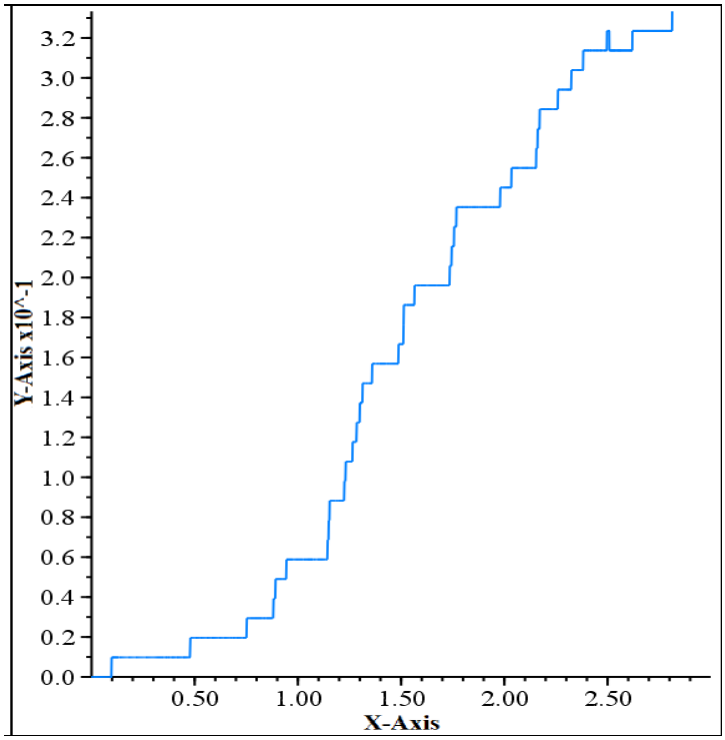

Fig. 6.12. Mixture 1- percentage of the particles passed through the screen vs time. X-axis: time (minute), Y-axis: percentage (%).

Mixture 2 This mixture had more long fibre particles and less chaff particles as compared with the Mixture 1. The simulation results showed that the amount of particles passing through the screen was increasing over time during the entire separation period (Fig. 6.13) and 16% of the particles passed the screen within 1.5 minute of separation duration. At the end of 3 minutes, 27% of particles passed through the screen. This value indicated that all chaff was separated, meaning that separation efficiency was 100%.

Please notice that some non-chaff material has passed the screen during the simulation as in the case of Mixture 1.

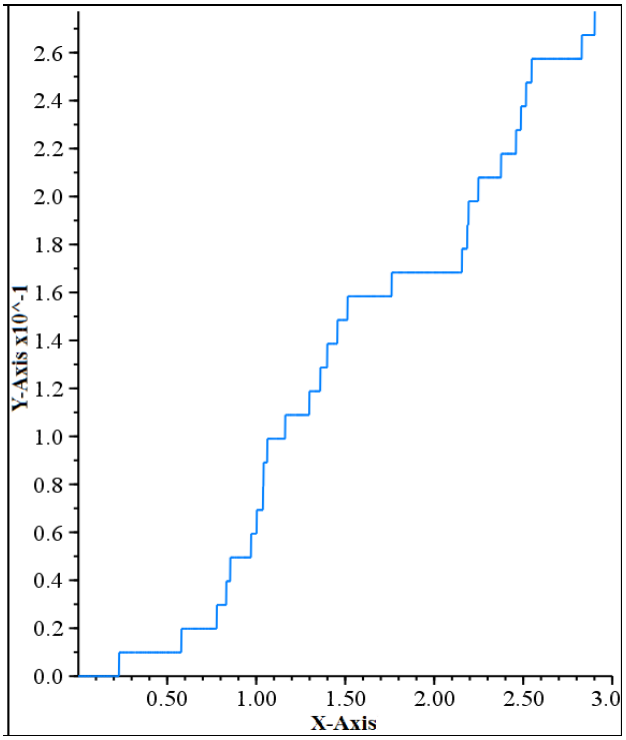

Fig. 6.13. Mixture 2- percentage of the particles passed through the screen vs time. X-axis: time (minute), Y-axis: percentage (%).

Mixture 3 The Mixture 3 had a lower percentage of long fibre particles and more chaff and a higher percentage of chaff than the Mixture 1. When the Mixture 3 was separated, the percentage of the particles passing through the screen was gradually increased before 0.75 minutes, and then a deep slope of increase was observed (Fig. 6.14). After 1.75 minutes, the increasing rate was slowed down. This trend was different with those from the other two mixtures. At the end of 3 minutes, approximately 33% of the particles

passed through the screen. This percentage was translated to a separation efficiency of 91%.

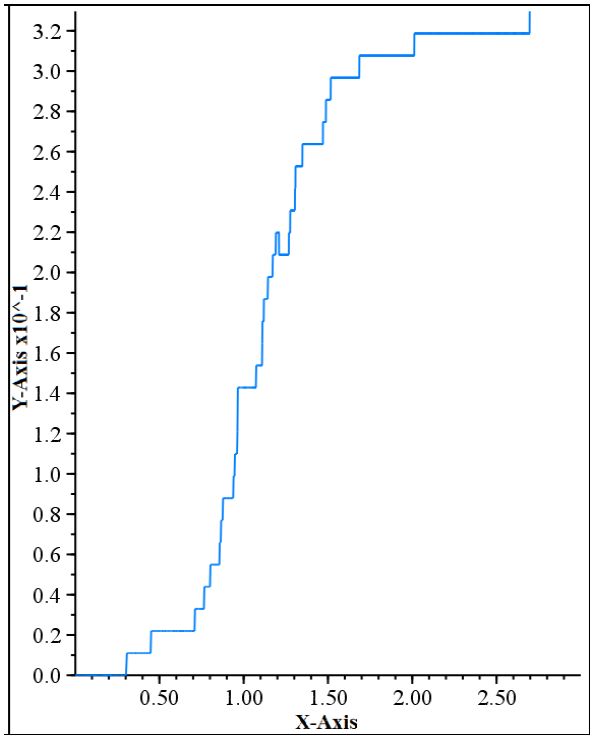

Fig. 6.14. Mixture 3- percentage of the particles passed through the screen vs time. X-axis: time (minute), Y-axis: percentage (%).

In summary, the separation efficiency of the 3D separator predicted by the model was affected by the composition of the mixture being separated. As comparing three different mixtures it was observed that percentage of the small particles and duration of separation time has huge impact on separation performance. For all three mixtures around 30 percent of total particles were passed through the screen after three minutes of separation. This causes over separation duration for mixture 1 and 2 whereas less for the mixture 2. Thus the separation performance was higher for mixture 2 and 3. The two mixtures

simulated had a separation performance of over 100%, implying losses of product. Also there was no entanglement among the particles into the mixture thus the motion and orientation of hemp particles on a screen vibrating in three directions are a complicated regime. Detail examinations of these dynamic behaviours were beyond the scope of this study. Further research is needed to explain the observed effects of the mixture composition on the separation efficiency of the 3D separator.

6.6. CONCLUSION

Tests of the 3D vibratory separator were conducted to remove the chaff from the processed material. The separation efficiency varied between 23.4 and 86.2%. The highest separation efficiency was found for the combination of a horizontal force of 1337 N and a vertical force of 4346 N. In simulations of the separation process using the 3D vibratory separator, hemp fibre and core can be defined as PFC^{3D} clusters. Different mixtures of processed hemp can be formed with those clusters having different sizes and microproperties. Varying the composition of the mixture, the simulated separation performance varied from 91% to 168%. It seemed that fewer long fibres and more chaff particles reduced the separation efficiency. Regardless of the composition of the mixture, the separation efficiency was higher than that observed in the tests. Efficiency greater than 100% means losses of the product. The model developed in this study can simulate the general behaviour of hemp fibre, core, and chaff particles in the separation process using the 3D vibratory separator. However, the model did not address the fibre entanglement nature. The current model needs improvement for the application

concerned in this study. However, the model is expected to work better for simulations of separations of other free flowing materials.

6.7. REFERENCES

Bócsa, I. and M. Karus. 1997. The Cultivation of Hemp's Botany, Varieties, Cultivation, and Harvesting. Sebastopol, Calif.: HempTech.

Cundall, P.A. and O.D.L. Strack. 1979. A discrete numerical model for granular assemblies. *Geotechnique* 29: 47-65.

Furl, C. and H. Hempel. 2000. Optimisation of a new machine for fibre processing by impact stress. Research report, Potsdam-Bornim, Germany: Instiyut fur Agrartechnik.

Gratton, J. and Y. Chen. 2004. Development of a field-going unit to separate fiber from hemp (cannabis sativa) stalk. *Applied Engineering in Agriculture* 20(2): 139-145.

Itasca. 2008. PFC^{3D} particle flow code in 3 dimensions, theory and background. Itasca Consulting Group, Inc. Minneapolis, Minnesota, USA

Khan M.R., Y. Chen, C. Lague, H. Landry, Q. Peng and W. Zhong. 2010. Compressive properties of Hemp (Cannabis sativa L.) stalks. *Biosystems Engineering* 106: 315 - 323.

Landry, H., C. Laguë and M. Roberge. 2006a. Discrete element representation of manure products. *Computers and Electronics in Agriculture* 51: 17-34.

Landry, H., F. Thirion, C. Laguë and M. Roberge. 2006b. Numerical modeling of the flow of organic fertilizers in land application equipment. *Computers and Electronics in Agriculture* 51: 35-53.

Lu, Z., S.C. Negi and J.C. Jofriet. 1997. A numerical model for flow of granular materials in silos. Part 1: model development. *Journal of Agricultural Engineering Research* 68: 223-229.

Munder, F. and H. Hempel. 2004. Results of an Advanced Technology for Decortication of Hemp, Flax and Linseed. Molecular Crystals and Liquid Crystals, 418: 165/[893]–179/[907].

Münder, F., Ch. Fürll and H. Hempel. 2004. Advanced Decortication Technology for Unretted Bast Fibres. *Journal of Natural Fibers* 1(1): 49 - 65.

Nye, W. and J. Ling. 2008. Good Vibrations You Say Potato I Say Potato. www.sweco.com.

Richardson, J.F. and J.H. Harker and J.R. Backhurst. 2002. Coulson and Richardson's Chemical Engineering, Particle Technology & Separation Processes. Vol 2, 5th edition. Tutterworth Heinemann, New York.

Sadek, M. A., Y. Chen, C. Laguë, H. Landry, Q. Peng and W. Zhong. 2011b. Characterization of the shear properties of hemp using discrete element method. *Transaction of ASABE* 54(6): 2279-2285.

Sakaguchi, F., M. Suzuki, J.F. Favier and S. Kawakami. 2001. Numerical simulation of the shaking separation of paddy and brown rice using the discrete element method. *Journal of Agricultural Engineering Research* 79(3): 307-315.

Sweco. 2003. Installation, operation and maintenance manual. www.sweco.com.

Chapter 7

General Conclusions and Future Recommendations

7.1. GENERAL CONCLUSIONS

The model developed using the PFC^{3D} can be used to simulate direct shear tests of hemp fibre and core. The model particle normal and shear stiffness was calibrated using the measurements, and it was 5e4 N/m for ground fibre and 8e4 N/m for ground core. When comparing the model results of shear properties with the measurements, the model agreed well with the measurements. It should be noted that the microproperties were calibrated based on a uniform particle size (particle diameter: 2 mm) for both fibre and core particles. The calibration results may vary when different particle sizes are chosen.

A virtual fibre, formed using spherical particles connected with bonds implemented in the PFC^{3D} parallel bond model, reflect tensile behaviour of real fibre. The model is capable of simulating numerous tensile characteristics of fibre, including load-extension curve, maximum stress, and elongation. An important microproperty, normal bond stiffness, can be calibrated through matching elongation behaviours between virtual and real fibres. The calibrated normal bond stiffness using the laboratory tensile test data was $1x10^{14}$ Pa m^{-1}.

PFC^{3D} was successfully used for developing a model to simulate hemp processing using a hammermill. With PFC^{3D}, virtual hemp stems can be formed using a cluster of balls and bonds. Calibration of particle microproperties can be achieved using virtual compression tests. The calibrated bond stiffness of hemp stem was $2.2x10^6$ Pa when compared to the literature data of hemp compression tests. The model was able to predict the power requirement of the hammermill, and kinetic and strain energies of hemp particles under different feeding masses and hammer rotational speeds. This information is important to assess the energy consumption of hemp processing and design the effective processing equipment.

In simulations of the separation process using a 3D vibratory separator, hemp fibre and core can be defined as PFC^{3D} clusters. Different mixtures of processed hemp can be formed with those clusters having various sizes and microproperties. Changing the composition of the mixture, the simulated separation performance varied from 91% to 168%, which was higher than the measurements. This higher separation performance indicated that the ratio of the small and large particle into the mixture and the separation duration was critical for serration performance. However, the model developed can simulate the general behaviour of hemp fibre, core, and chaff particles in the separation process using the 3D vibratory separator. The model was not able to address the fibre entanglement nature. It needs improvement for the application concerned in this study. However, the model is expected to work better for simulations of separations of other free flowing materials.

Throughout the study a simulation technique has been established for hemp fibre processing which could be further used for prediction of machine-material behaviour for different conditions including end particle size distribution after hammermill operation, particle movement on the 3D vibratory separator, quantification of the particles after separation, and entanglement of the particles within the machines. These models will be helpful for understanding new processes and development of new equipment for hemp processing.

7.2. LIMITATIONS AND RECOMMENDATIONS

This was the first attempt of using the DEM method for modeling hemp materials. In defining hemp particles, several simplifications were made. The virtual hemp stem in the hammermill simulations was constructed with balls having the same properties. This did not address the real structure of a hemp stem consisting of outer fibre layer and inner core layer. In the separator simulations, the fraction of fibre bound to core was not considered in the virtual mixture of the processed hemp. In both the hammermill and separator models, the structure of the virtual hemp fibres did not reflect the flexibility and entangling natures of natural fibres. All these may limit the applications of the models and should be considered in the further research.